

**Quantitative Delaminierung zur Herstellung von Nanoschichten
Struktur-inhärenter Dicke**

DISSERTATION

zur Erlangung des akademischen Grades eines
Doktors der Naturwissenschaften (Dr. rer. nat.)
an der Fakultät für Biologie, Chemie und Geowissenschaften
der Universität Bayreuth

vorgelegt von

Matthias Daab

geboren in Mosbach

Bayreuth, 2018

**Quantitative Delaminierung zur Herstellung von Nanoschichten
Struktur-inhärenter Dicke**

DISSERTATION

zur Erlangung des akademischen Grades eines
Doktors der Naturwissenschaften (Dr. rer. nat.)
an der Fakultät für Biologie, Chemie und Geowissenschaften
der Universität Bayreuth

vorgelegt von

Matthias Daab

geboren in Mosbach

Bayreuth, 2018

Die vorliegende Arbeit wurde in der Zeit von Oktober 2015 bis Juni 2018 in Bayreuth am Lehrstuhl für Anorganische Chemie 1 unter Betreuung von Prof. Dr. Josef Breu angefertigt.

Vollständiger Abdruck der von der Fakultät für Biologie, Chemie und Geowissenschaften der Universität Bayreuth genehmigten Dissertation zur Erlangung des akademischen Grades eines Doktors der Naturwissenschaften (Dr. rer. nat.).

Dissertation eingereicht am: 03.07.2018

Zulassung durch die Promotionskommission: 04.07.2018

Wissenschaftliches Kolloquium: 22.11.2018

Amtierender Dekan: Prof. Dr. Stefan Peiffer

Prüfungsausschuss:

Prof. Dr. Josef Breu (Gutachter)

Prof. Dr. Georg Papastavrou (Gutachter)

Prof. Dr. Anna Schenk (Vorsitz)

Prof. Dr. Seema Agarwal

„Eiserner Wille. Das einzige Werkzeug, das man nicht kaufen kann.“

– Hornbach-Werbung, *anno 2005* –

Meiner lieben Familie

Inhalt

Inhalt

Abkürzungsverzeichnis	ix
1. Summary	1
2. Zusammenfassung	3
3. Einleitung	5
3.1. Grundbegriffe zu Schichtverbindungen an ausgewählten Beispielen	5
3.2. Nanoschichten Struktur-inhärener Dicke	7
3.3. Quantitative Delaminierung durch repulsive osmotische Quellung	9
3.4. Synthese von 2:1 Schichtsilikaten	16
3.5. Anwendungen von Nanoschichten	18
3.6. Problemstellung	21
4. Synopsis	22
4.1. Quantitative Delaminierung geordneter Heterostrukturen	24
4.2. Kriterien für das Einsetzen der repulsiven osmotischen Quellung.....	26
4.3. Ladungsdichte-übergreifende Delaminierung	29
4.4. Isomorphe Substitution und elektrische Leitfähigkeit.....	30
5. Literatur	32
6. Ergebnisse	41
6.1. Quantitative Delaminierung geordneter Heterostrukturen	41
6.2. Kriterien für das Einsetzen der repulsiven osmotischen Quellung.....	57
6.3. Ladungsdichte-übergreifende Delaminierung	70
6.4. Isomorphe Substitution und elektrische Leitfähigkeit.....	83
7. Publikationsliste	97
8. Danksagung	98
9. Erklärung des Verfassers.....	99

Abkürzungsverzeichnis

(<i>a,b</i>)	kristallographische <i>a·b</i> Ausdehnung der 2:1 Schichtsilicatstruktur
(<i>a,b</i>) _t / (<i>a,b</i>) _o	Verhältnis der <i>a·b</i> Ausdehnungen der Tetraeder- / Oktaederschicht für ideale unverzerrte Polyeder
α	Aspektverhältnis, Verhältnis von lateraler Ausdehnung zur Dicke
A _C	Ladungsäquivalentfläche einer Schichtverbindung
A _I	Ladungsäquivalentfläche des Interkalates
C ₃	n-Propylammonium
C ₄	n-Butylammonium
<i>d</i>	kristallographischer <i>d</i> -Wert
DEAE	Diethylammoniummethanol
DMAE	Dimethylammoniummethanol
ϕ	Volumenbruch
<i>h</i>	Galleriehöhe <i>h</i> = <i>d</i> - 9.6 Å entspricht der Dicke einer 2:1 Silicatschicht)
κ^1	<i>Debye</i> -Länge
M	Kation in den Oktaederlücken der 2:1 Schichtsilicate
Meglumin	<i>N</i> -Methyl- <i>D</i> -glucammonium
OLED	Organische Leuchtdiode, <i>organic light emitting diod</i>
p.f.u.	pro Formeleinheit O ₁₀ (OH/F) ₂ , <i>per formula unit</i>
PET	Polyethylenterephthalat
σ	Ladungsdichte
<i>t</i>	Dicke einer 2:1 Silicatschicht (9.6 Å)
TBA	Tetrabutylammonium
TMA	Tetramethylammonium
TMAEMA	2-(Trimethylammonium)ethylmethacrylat
TRIS	Tris(hydroxymethyl)ammoniummethan

Abkürzungsverzeichnis

w Besetzungswahrscheinlichkeit

x Schichtladung

Z Zwischenschichtion

□ Oktaederlücke

1. Summary

The quantitative delamination of layered materials is feasible by repulsive osmotic swelling in water. Thereby nanosheets of structure-inherent thickness are obtained as colloidal stable gels that can be used as gas barrier pigments in polymer nanocomposite formulations. Based on synthetic 2:1 layered silicates new insights into the conditions for the onset of osmotic swelling are gained. Furthermore, the functionalization of the 2:1 layers by isomorphous substitution is discussed.

The first part of the thesis deals with a partial-ion exchanged intercalation heterostructure that is capable of osmotic swelling and whose homoionic phases do not swell osmotically. A partial ion-exchange was conducted with a 2:1 layered silicate ($\{\text{Na}_{0.6}\} [\text{Mg}_{2.4}\text{Li}_{0.6}]^{\text{oct}}\text{Si}_4\text{O}_{10}\text{F}_2$; $x = 0.6$ p.f.u., charges per formula unit $\text{Si}_4\text{O}_{10}\text{F}_2$, p.f.u.) that was treated with *n*-butylammonium (C4) salts, yielding the Heterostructure " $\{\text{Na}\}$ - [2:1 layer] - {C4} - [2:1 layer]" (array normal to the stacking direction). In contrast to its homoionic $\{\text{Na}\}$ - and {C4}-phase, this structure is capable of repulsive osmotic swelling. The mechanism presumably runs in two steps. At first, the osmotic swelling of the $\{\text{Na}\}$ -interlayer ion forms "sandwich structures" of the type "[2:1 layer] - {C4} - [2:1 layer]", followed by a disintegration of these aggregates into individual layers of structure-inherent thickness. For the homoionic $\{\text{Na}\}$ -phase the attractive electrostatic interactions are too high to permit the onset of repulsive osmotic swelling. This would only be feasible for $x < 0.55$ p.f.u.. The homoionic {C4}-phase also does not swell osmotically. In this respect, it is observed that the {C4}-phase despite its layer charge of 0.6 p.f.u., is characterized by a lower intracrystalline reactivity than more highly charged, osmotically swellable {C4}-vermiculites (typically $x > 0.65$ p.f.u.).

This counter-intuitive swelling behavior of the organo-intercalates is explained in the second part of the thesis. A systematic combination of organo-cations of different size intercalated in silicates of different layer charge was examined. The results indicate that the "steric pressure" of the organo-cations contributes to the onset of osmotic swelling and that this pressure depends on the layer charge: The intercalated cations have a certain space requirement per charge in the interlayer space. To achieve the necessary "steric pressure" their space requirement must be higher than (or equal to) the space that is available per charge within the used layered silicate. If this requirement is met, a flat lying monolayer of organo-cations is no longer sufficient to ensure electro neutrality, in particular if some water molecules have already been taken up by the organo-cation. In addition, excessive swelling of the dried intercalation compound in moist

Summary

air (98% relative humidity) is a necessary criterion for the onset of osmotic swelling. The excessive swelling is characterized by (i) an increase in d-spacing of $\Delta d \gtrsim 3.5 \text{ \AA}$, which corresponds to the hygroscopicity of the intercalation compound and the “steric pressure” by water uptake and (ii) by exceeding a minimum absolute value of $d^* \gtrsim 17.5 \text{ \AA}$. The last condition might be a decisive contribution to make the repulsive interactions larger than the attractive ones. Increasing the d-spacing critically weakens attractive interactions and repulsive osmotic swelling in water sets in.

Based on these insights, in the third part a bulky ammonium sugar (*N*-methyl-*D*-glucammonium) has been identified as a sterically demanding interlayer cation which, for the first time, enables low charged organo-smectites to delaminate by repulsive osmotic swelling as well as highly charged organo-vermiculites. More precisely, the osmotic swelling is feasible over a range of at least $0.3 \leq x \leq 0.7$ p.f.u.. Noteworthy, all above-mentioned criteria for the onset of osmotic swelling are met for *N*-methyl-*D*-glucammonium intercalation compounds for the whole range of layer charges. This also applies to charge-heterogeneous systems, which significantly reduces the demands on charge homogeneity of barrier pigments that shall be delaminated utterly.

Furthermore, the 2:1 layer was functionalized by isomorphous substitution to investigate its electronic conductivity in the fourth part, motivated by a potential application of 2:1 layers in electronic heterostructures in future works. An iron-rich layered silicate of the composition $\{\text{Ba}_{0.96}\} [\text{Fe}_{2.68}\text{Al}_{0.28}]^{\text{oct}} < \text{Si}_{2.01}\text{Al}_{1.99} >^{\text{tetra}} \text{O}_{10}\text{F}_2$ was synthesized. Based on the analysis of its single-crystal structure, the limitations concerning the degree of isomorphous iron substitution are discussed in comparison to known crystal structures. Its conductivity is of the order of magnitude $\mu\text{S}/\text{cm}$ (200°C) and is increased by a factor > 2 upon oxidation of structural iron. By comparing the conductivities to a ferrous-tainiolite ($\{\text{Cs}\} [\text{Fe}_2\text{Li}]^{\text{oct}} < \text{Si}_4 >^{\text{tetra}} \text{O}_{10}\text{F}_2$) it is evidenced that the electronic conductivity of iron-rich 2:1 layers is rather determined by the degree of oxidation of iron than by total iron content.

This work was in part performed in collaboration with BYK Chemie GmbH. The present work is a cumulative thesis, therefore all results are presented in the attached manuscripts.

2. Zusammenfassung

Die quantitative Delaminierung von Schichtverbindungen ist durch repulsive osmotische Quellung in Wasser möglich. Diese Methode liefert Nanoschichten von Struktur-inhärenter Dicke in kolloidal stabiler Dispersion. Solche Nanoschichten finden als Gasbarriere-Pigmente in Polymernanokompositen Anwendung. Im Rahmen dieser Arbeit ist es auf Basis synthetischer 2:1 Schichtsilicate gelungen, neue Wege zur Herstellung osmotisch quellfähiger Schichtverbindungen zu finden und den Mechanismus des Einsetzens der osmotischen Quellung verständlich zu machen. Darüber hinaus wurde eine Untersuchung zur Funktionalisierung der 2:1 Schichten durch isomorphe Substitution durchgeführt.

Im ersten Teil der Arbeit wird eine osmotisch quellfähige Heterostruktur präsentiert, deren Randphasen nicht delaminieren. Durch partiellen Ionenaustausch von einem 2:1 Schichtsilicat der Summenformel $\{Na_{0.6}\} [Mg_{2.4}Li_{0.6}]^{oct} <Si_4>^{tet} O_{10}F_2$ (Schichtladung $x = 0.6$ pro Formeleinheit $Si_4O_{10}F_2$, p.f.u.) mit *n*-Butylammonium-Ionen (C4) wurde eine Interkalations-Heterostruktur der Form „{Na} - [2:1 Schicht] - {C4} - [2:1 Schicht]“ (Anordnung in Stapelrichtung) erhalten. Im Gegensatz zu ihren homoionischen Randphasen (reine {Na}- bzw. reine {C4}-Form) ist diese Struktur osmotisch quellfähig. Die Delaminierung läuft vermutlich in zwei Schritten ab: der osmotischen Quellung der {Na}-Zwischenschicht in „Sandwich-Strukturen“ der Form „[2:1 Schicht] - {C4} - [2:1 Schicht]“ und dem Zerfall dieser Aggregate in einzelne 2:1 Schichten Struktur-inhärenter Dicke. Für die reine homoionische {Na}-Randphase sind die attraktiven elektrostatischen Wechselwirkungen zu hoch für repulsive Quellung, dies wäre nur für $x < 0.55$ p.f.u. möglich. Die vollständig Ionen-ausgetauschte, homoionische {C4}-Randphase quillt ebenfalls nicht osmotisch und weist trotz ihrer Schichtladung von 0.6 p.f.u. eine niedrigere intrakristalline Reaktivität bezüglich der Quellung auf als höher geladene, osmotisch quellfähige {C4}-Vermiculite mit typischerweise $x > 0.65$ p.f.u..

Dieses auf den ersten Blick widersprüchliche Quellverhalten der homoionischen Organo-Interkalate wurde im zweiten Teil der Arbeit erklärt. Eine systematische Kombination von Organo-Kationen unterschiedlicher Größe und verschiedenen Schichtladungen wurde untersucht. Dabei wurde festgestellt, dass der „sterische Druck“ der Organo-Kationen entscheidend dazu beiträgt, die osmotische Quellung auszulösen. Dieser „sterische Druck“ hängt wiederum von der Schichtladung ab: Die interkalierten Kationen besitzen einen gewissen Platzbedarf pro Ladung im Zwischenschichtraum. Es zeigte sich, dass der Platzbedarf größer oder gleich der Ladungsäquivalentfläche des verwendeten Schichtsilicates sein muss. Dies bedeutet, dass eine flachlie-

Zusammenfassung

gende Monolage der Organo-Kationen nicht mehr ausreichend ist, um Elektroneutralität zu gewährleisten. Dies gilt insbesondere, wenn erste Wassermoleküle aufgenommen werden. Darüber hinaus ist die exzessive Quellung der getrockneten Interkalationsverbindung an feuchter Luft (98 % Luftfeuchte) ein notwendiges Kriterium für das Einsetzen der osmotischen Quellung. Die exzessive Quellung ist durch zwei Merkmale gekennzeichnet: (i) eine Erhöhung des d -Wertes um $\Delta d \gtrsim 3.5 \text{ \AA}$, was der Hygroskopizität der Interkalationsverbindung und dem „sterischen Druck“ durch Wasseraufnahme entspricht und (ii) durch das Überschreiten eines kritischen d -Wertes von $d^* \gtrsim 17.5 \text{ \AA}$. Dieses letzte Kriterium könnte ein entscheidender Beitrag dazu sein, die attraktiven Wechselwirkungen entscheidend zu schwächen und repulsive osmotische Quellung in Wasser auszulösen.

Basierend auf diesen Einblicken wurde im dritten Teil mit *N*-Methyl-*D*-glucammonium ein Ammonium-Zucker als sterisch anspruchsvolles Zwischenschichtkation identifiziert, das erstmals niedrig geladene Organo-Smectite osmotisch quellen lässt. Darüber hinaus ist die osmotische Quellung hiermit in einem Bereich von mindestens $0.3 \leq x \leq 0.7$ p.f.u. möglich. Hierbei sind die oben genannten Kriterien für das Einsetzen der osmotischen Quellung für den gesamten Schichtladungsbereich erfüllt, was die Ansprüche an die Qualität von Barriere-Pigmenten bezüglich Ladungshomogenität senkt.

Im vierten Teil wurde die 2:1 Schicht durch isomorphe Substitution funktionalisiert. Die Substitution von Eisen in die 2:1 Schicht kann deren elektrische Leitfähigkeit erhöhen. Relevant ist dies im Hinblick auf eine mögliche Verwendung in elektrischen Heterostrukturen. Es wurde ein Eisen-reiches 2:1 Schichtsilicat der Zusammensetzung $\{\text{Ba}_{0.96}\} [\text{Fe}_{2.68}\text{Al}_{0.28}]^{okt} < \text{Si}_{2.01} \text{Al}_{1.99} >^{tet} \text{O}_{10}\text{F}_2$ synthetisiert. Die Limitierungen bezüglich der isomorphen Substitution (Höhe des Eisengehaltes) werden auf Basis der Einkristall-Struktur durch Vergleich mit bekannten Kristallstrukturen diskutiert. Die Leitfähigkeit liegt in der Größenordnung $\mu\text{S}/\text{cm}$ bei 200°C und wird durch die Oxidation von strukturellem Eisen um einen Faktor > 2 erhöht. Der Vergleich mit einem Tainiolit der Zusammensetzung $\{\text{Cs}\} [\text{Fe}_2\text{Li}]^{okt} < \text{Si}_4 >^{tet} \text{O}_{10}\text{F}_2$ zeigt, dass bei hohen Eisengehalten (> 2 p.f.u.) der Oxidationszustand des Eisens und nicht der Gesamtgehalt an Eisen die Leitfähigkeit maßgeblich bestimmt.

Die vorliegende Arbeit ist teilweise in Kooperation mit der BYK Chemie GmbH entstanden. Bei dieser Arbeit handelt es sich um eine kumulative Dissertation, daher werden die Ergebnisse thematisch sortiert in den angehängten Manuskripten beschrieben.

3. Einleitung

3.1. Grundbegriffe zu Schichtverbindungen an ausgewählten Beispielen

Der Aufbau von Kristallen lässt sich häufig in Schichten beschreiben. Eine Schichtverbindung liegt jedoch nur dann vor, wenn die Bindungsverhältnisse anisotrop sind. Die Modifikationen von Bornitrid verdeutlichen dies: β -Bornitrid (Zinkblende-Typ) lässt sich als kubisch dichteste Kugelpackung - also als ABC Schichtfolge dichtgepackter Nitrid-Schichten - beschreiben, in der jede zweite Tetraederlücke mit Bor besetzt ist.^[1] Da die Bindungsverhältnisse hier jedoch isotrop sind (gleiche Bindungsverhältnisse und -längen in allen drei Dimensionen), liegt keine Schichtverbindung vor. α -Bornitrid hingegen weist anisotrope Bindungsverhältnisse auf und ist daher eine Schichtverbindung: Hier beträgt die B-N-Bindungslänge in der Schicht 1.4 Å, während der kürzeste Abstand in Stapelrichtung 3.3 Å beträgt (B-N-Abstand zwischen gegenüberliegenden planaren, hexagonalen B-N-Waben).^[2]

Unterschiedliche Strukturtypen und unterschiedliche chemische Zusammensetzungen innerhalb der Klasse der Schichtverbindungen sorgen für eine Diversität, die eine vollständige Auflistung nahezu unmöglich und eine Einteilung notwendig macht. Im Allgemeinen lassen sich Schichtverbindungen in neutrale, positiv geladene und negativ geladene Schichten einteilen.^[3] Weitere Möglichkeiten der Einteilung können Unterschiede in der Leitfähigkeit und im Redox-Verhalten oder im Quellverhalten der Schichtverbindungen sein.^[4-5]

Ladung in der Schicht lässt sich beispielsweise durch isomorphe Substitution erzeugen: Im Fall von Talk und Tainiolit werden über den Substitutionspfad $[\text{Mg}^{2+}]^{\text{oxt}} \rightarrow [\text{Li}^+]^{\text{oxt}}$ negativ geladene Schichten erhalten, deren Ladung durch Zwischenschichtkationen $\{\text{Z}\}$ ausgeglichen wird (**Abb. 1**). Liegen reduzierbare oder oxidierbare Atome in der Schicht vor, kann mitunter Ladung durch Redox-Reaktionen erzeugt werden (Beispiel: das Redox-amphotere Graphit)^[6-7] oder eine bestehende Schichtladung kann durch Redox-Reaktionen variiert werden (Beispiel: eisenhaltiger Tainiolit, Variation des $\text{Fe}^{\text{II}}/\text{Fe}^{\text{III}}$ -Verhältnisses).^[8]

Einleitung

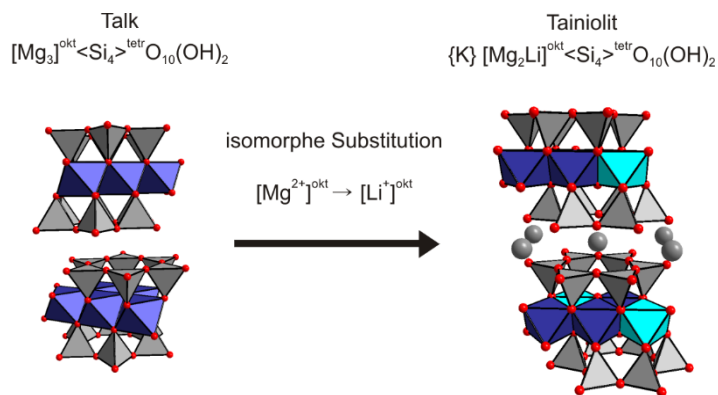


Abb. 1: 2:1 Schichtsilicate: isomorphe Substitution am Beispiel von Talk^[9] und Tainiolit.^[10]

Im Fall von Talk und Tainiolit handelt es sich um 2:1 Schichtsilicate. Diese Art der Schichtverbindungen wird in der vorliegenden Arbeit verwendet, da deren Struktur vielfältige chemische Zusammensetzungen und Schichtladungen durch isomorphe Substitution realisieren kann und sich damit besonders für grundlegende Studien eignet (**Kap. 3.4.**). Die Struktur der 2:1 Schichtsilicate ist aus zwei Tetraederschichten aufgebaut, die über ihre apikalen Sauerstoffatome mit einer Oktaederschicht verknüpft sind. Die van-der-Waals-Dicke einer einzelnen 2:1 Schicht beträgt ca. 9.6 Å. Die Zwischenschichtionen liegen im Fall von Tainiolit zwischen gegenüberliegenden hexagonalen Kavitäten der Tetraederschichten.

Zwischenschichtkationen können in vielen Fällen durch einen ausreichenden Ionenhintergrund in wässriger Suspension ausgetauscht werden, was vielfältige Funktionalisierungen ermöglicht (**Kap. 3.5.**). Hierbei werden die Ionen gemäß ihrem Verteilungsgleichgewicht in den Zwischenschichtraum eingelagert (interkaliert).^[11] Die Menge der austauschbaren Zwischenschichtionen wird durch die Ionenaustauschkapazität (gebräuchliche Einheit: mval/100 g) quantifiziert.

Ein wichtiges Charakteristikum geladener Schichtverbindungen, das auch die Ionenaustauschkapazität bestimmt, ist deren Ladungsdichte σ (gebräuchliche Einheit: Ladungen/nm²). Für die Diskussion von Hydroxonium-interkalierten Schichtverbindungen werden in dieser Arbeit die Dichte der Ladungen und die Dichte der Schichtoberflächen-OH-Gruppen als ein Wert in der Ladungsdichte zusammengefasst, wie in der Literatur üblich (**Kap. 3.3.1.**). Da insbesondere organische Zwischenschichtionen einen gewissen Platzbedarf mit sich bringen, wird als Maß für deren Platzbedarf häufig die Ladungsäquivalentfläche verwendet,^[12] die in etwa der Projektionsfläche eines interkalierten Kations entspricht. Die Ladungsdichten der Schichtverbindungen werden zur besseren Vergleichbarkeit mit dem Platzbedarf der Zwischenschichtionen häufig ebenfalls in eine Ladungsäquivalentfläche A_C umgerechnet (Kehrwert der Ladungsdichte: $A_C = 1/\sigma$, gebräuchliche Einheit: Å²/Ladung).

3.2. Nanoschichten Struktur-inhärenter Dicke

Eine Nanoschicht Struktur-inhärenter Dicke ist beispielsweise eine einzelne Graphit-Lamelle (einzelne hexagonale sp^2 -hybridisierte Kohlenstoffschicht atomarer Dicke, was dann als Graphen bezeichnet wird) oder eine einzelne 2:1 Silicatschicht. Arbeiten zur Herstellung und Anwendungen solcher Schichten finden sich häufig unter dem Schlagwort *nanosheet*, das erstmals von *Sasaki* 1996 verwendet wurde (erste Nennung in über Scifinder zugänglichen Publikationen).^[13] Das wachsende Interesse an solchen Materialien spiegelt sich in der steigenden Zahl der jährlichen Neuerscheinungen zu diesem Thema wieder (**Abb. 2**, gesamte Anzahl der Publikationen: grün, davon Patente: schwarz). Seit dem Jahr 2003 erscheinen jährlich mehr und mehr Patente, da diese Materialien kommerzielles Interesse geweckt haben.

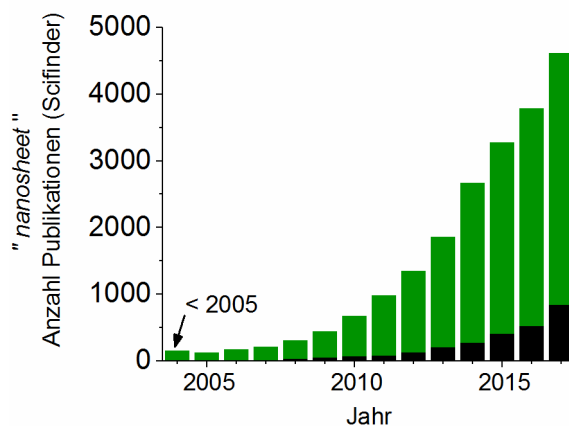


Abb. 2: Bibliographische Analyse zu dem Schlagwort *nanosheet*, Publikationen bei Scifinder (grün: Publikationen gesamt, schwarz: davon Patente; Informationen abgerufen im Januar 2018).

Nanoschichten Struktur-inhärenter Dicke weisen andere Eigenschaften als ihr *Bulk*-Material auf. Die spezifische Oberfläche von Schichtverbindungen ist nur für einzelne Nanoschichten maximal (Graphen: $2600 \text{ m}^2/\text{g}$, 2:1 Silicatschicht: $700 \text{ m}^2/\text{g}$) während die korrespondierenden *Bulk*-Materialien, typischerweise bestehend aus Stapeln von > 1000 einzelnen Schichten, Oberflächen von $<< 10 \text{ m}^2/\text{g}$ aufweisen. Die anisotropen Bindungsverhältnisse in Schichtverbindungen haben zur Folge, dass diese meist ein Aspektverhältnis $\alpha > 1$ aufweisen (Verhältnis von lateraler Ausdehnung zur Dicke). Das maximale Aspektverhältnis ist erreicht, wenn Nanoschichten von Struktur-inhärenter Dicke vorliegen und es bei deren Herstellung nicht zum Bruch von Primär-Partikeln des *Bulk*-Materials kommt.^[14-15] Grenzfläche und Aspektverhältnis von Nanoschichten als Füllstoff in einer Polymermatrix beeinflussen die Eigenschaften solcher Kompositmaterialien entscheidend (**Kap. 3.5.**).^[16]

Einleitung

3.2.1. Herstellung

Prinzipiell existieren zwei Ansätze um Nanoschichten Struktur-inhärenter Dicke zu erhalten:

- *Bottom-up*-Methoden

z.B. Epitaktische Dampfabscheidung,^[17] Synthese durch Vorläuferverbindungen,^[18] Molekularstrahl-Epitaxie^[19]

- *Top-down*-Methoden

z.B. Repulsive Quellung von geladenen Schichtverbindungen,^[14, 20-21] mechanisches Scheren (mit nachfolgender Aufreinigung von Aggregaten)^[7]

Zur wirtschaftlichen Verwendung sind einfach skalierbare Verfahren notwendig, was *Bottom-up*-Methoden gegenüber *Top-down*-Methoden im Allgemeinen nachteilig erscheinen lässt.^[22]

3.2.2. Delaminierung oder Exfolierung

Top-down-Methoden können bezüglich der Vollständigkeit der Spaltung in Stapelrichtung durch die beiden Begriffe Delaminierung und Exfolierung unterschieden werden. Diese wurden von *Lagaly* und *Gardolinsky*^[23] folgendermaßen definiert:

- Delaminierung ist die Separation der einzelnen Schichten von Struktur-inhärenter Dicke aus dem *Bulk*-Material.
- Exfolierung ist die Zerlegung großer Stapel von Schichten in kleinere Stapel von Schichten.

Leider wird in der Literatur nicht immer konsequent zwischen Delaminierung und Exfolierung unterschieden, teilweise werden die beiden Begriffe auch in umgekehrtem Zusammenhang verwendet.^[24] Die ursprüngliche Definition von *Lagaly* und *Gardolinski* hat dennoch – auch außerhalb der Schichtsilicat-Forschung – Anklang gefunden.^[4] Eine weitere Schwierigkeit in der Evaluierung von Literatur zum Thema *nanosheets* ergibt sich daraus, dass nicht immer dargelegt wird, ob tatsächlich quantitative Delaminierung in Nanoschichten Struktur-inhärenter Dicke vorliegt oder ob es sich um Exfolierung handelt.

Als Leitfaden für eine erste Einordnung können folgende Überlegungen für den Fall von *Top-down*-Methoden dienen: Bei mechanischem Scheren kann nicht von Delaminierung gesprochen werden, da ohne weitere Aufreinigung Stapel aus mehreren Schichten zurückbleiben (es handelt sich in solchen Fällen um Exfolierung), darüber hinaus brechen hierbei Primärpartikel, was das Aspektverhältnis verringert.^[7] Eine schonende Methode, die quantitative Delaminierung des *Bulk*-Materials in Nanoschichten Struktur-inhärenter Dicke ermöglicht, ist die repulsive osmotische Quellung, die kolloidal stabile Suspensionen aus Nanoschichten liefert.^[15]

3.3. Quantitative Delaminierung durch repulsive osmotische Quellung

Einige geladene Schichtverbindungen können ausgehend vom trockenen Zustand bereits an feuchter Luft durch Hydratation von Zwischenschichtionen zu höheren Schichtabständen quellen.^[25-26] Der Schichtabstand wird hierbei in diskreten Stufen durch Interkalation von einer bestimmten Anzahl an Wasserlagen erhöht. Die Anzahl der Wasserlagen in solchen kristallinen Hydraten kann durch den Wasserdampf-Partialdruck variiert werden. Hydratstufen für 2:1 Schichtsilicate mit Alkali- und Erdalkalimetall-Zwischenschichtionen sind typischerweise 0 bis 3 Wasserlagen, $d \approx 9.7 \text{ \AA}$ (0 Wasserlagen, trocken), 12.3 \AA (1 Wasserlage), 15.1 \AA (2 Wasserlagen), 18.1 \AA (3 Wasserlagen).^[27-29] Dieses Quellverhalten wird kristalline Quellung genannt.

Eine Erhöhung der Wasseraktivität durch Eintauchen der Schichtverbindung in entsalztes Wasser führt unter bestimmten Bedingungen zur weiteren Hydratation der Zwischenschichtionen durch osmotische Quellung. Diese separiert die einzelnen Schichten repulsiv und bei ausreichender Verdünnung bis hin zur freien Drehbarkeit der Schichten.^[14] Die quantitative Delaminierung durch repulsive osmotische Quellung ist nach Wissens des Autors bislang nur für Schichtverbindungen mit negativ geladenen Schichten bewiesen worden, daher werden in diesem Kapitel zur ausführlichen Erläuterung dieses Phänomens nur solche Schichtverbindungen diskutiert. Eine prinzipielle Beschränkung auf negativ geladene Schichten besteht möglicherweise nicht.

3.3.1. Stand der Technik: Bedingungen für die osmotische Quellung

Im Gegensatz zu ladungsneutralen Schichtverbindungen, können durch Änderung des Abstandes von geladenen Schichten diverse Übergänge zwischen Attraktion (negativer osmotischer Druck zwischen den Schichten) und Repulsion (positiver osmotischer Druck) durchlaufen werden. Es existieren unterschiedliche Ansätze zur Beschreibung dieser Zustandsänderungen in Abhängigkeit des Schichtabstandes. Diese Ansätze beruhen beispielsweise auf Monte Carlo Simulationen des Gesamtdruckes unter Berücksichtigung der elektrostatischen Kopplung von Gegenionen und Schicht auf Basis der Grenzfälle für starke und schwache Kopplung.^[30] Eine anschaulichere Simulationen des Gesamtdruckes, der aus Attraktion (elektrostatisch: Gegenion-Schicht mit kontinuierlicher Ladungsverteilung in der Schicht) und Repulsion (Entropie der Gegenionen; Abstoßung durch ausgeschlossenes Volumen; elektrostatisch: Gegenion-Gegenion, Schicht-Schicht) resultiert, wird in Ref. [31] gegeben und berücksichtigt die sich mit dem Schichtabstand ändernde Verteilung der Zwischenschichtionen. Hier wird jedoch für hohe

Einleitung

Schichtseparationen für viele relevante Schichtladungen Attraktion vorausgesagt, was osmotische Quellung unmöglich machen würde und die Schwierigkeiten in der theoretischen Beschreibung des Übergangs von kristalliner zu osmotischer Quellung zeigt.

Die Ladungsdichte der Schicht ist von besonderer Bedeutung für die repulsive osmotische Quellung, da sie den Betrag der elektrostatischen Attraktion dominiert. So ist für niedrig geladene 2:1 Schichtsilicate mit einer Ladungsdichte von < 2.3 Ladungen/nm² mit Na⁺ als Zwischenschichtkation osmotische Quellung in Wasser möglich (z.B. synthetischer {Na_{0.5}}-Smecit {Na_{0.5}} [Mg_{2.5}Li_{0.5}]^{okt}<Si₄>^{tetr}O₁₀F₂^[15] oder bestimmte natürliche, aufgereinigte {Na}-Smectite^[20]).^[32] Dahingegen verhindern Ladungsdichten > 2.3 Ladungen/nm² die osmotische Quellung von Na⁺ durch zu starke elektrostatische Attraktion (Berechnung der Ladungsdichten für 2:1 Schichtsilicate, s. **Kap. 3.4.1.**).^[32-33]

Die osmotische Quellung von höher geladenen Schichtsilikaten kann durch Zwischenschichtkationen höherer Hydratationsenthalpie bewerkstelligt werden: Li⁺ weist mit 519 kJ/mol eine höhere Hydratationsenthalpie als Na⁺ (409 kJ/mol) auf^[34] und kann höher geladene 2:1 Schichtsilicate (z.B. einige Vermiculite mit > 2.3 Ladungen/nm²)^[35] osmotisch quellen lassen.^[36] Hier ist zuvor ein aufwändiger Kationenaustausch der nicht osmotisch quellfähigen {Mg}-Vermiculite durch Li⁺ notwendig. Dies ist nötig, da osmotische Quellung durch zweiwertige Zwischenschichtionen wie Mg²⁺ nicht möglich ist. Diese weisen zwar eine hohe Hydratationsenthalpie pro Ladung auf, haben aber auch eine größere Gouy-Chapman-Länge als einwertige Kationen (Entfernung bei der die Coulomb-Energie eines Ions zu einer geladenen Schicht der thermischen Energie entspricht).

Zusammenfassend müssen Alkalimetallion-interkalierte Schichtsilicate eine hohe Hydratationsenthalpie (Repulsion) aufweisen und/oder eine ausreichend geringe Schichtladung (Attraktion), um osmotisch quellfähig zu sein. Die osmotisch quellfähigen Zwischenschichtionen Li⁺ und Na⁺ weisen im Zwischenschichtraum signifikant höhere Hydratationsenthalpien auf als ihre höheren Homologen (K⁺, Rb⁺),^[37] die in 2:1 Schichtsilikaten nicht osmotisch quellen und eine höhere Selektivität für die innere Helmholtzschicht aufweisen.

Liegen Schichtverbindungen vor, die aufgrund ihrer hohen Ladungsdichte nicht osmotisch quellen, kann osmotische Quellung in einigen Fällen durch Interkalation von sterisch anspruchsvollen, aber hydrophilen organischen Zwischenschichtkationen hervorgerufen werden.

Beispiele für solche Zwischenschichtkationen sind TBA (Tetrabutylammonium, 90 Å²/Ladung), DMAE (Dimethylammoniumethanol, 38 Å²/Ladung), C4 (*n*-Butylammonium,

37 Å²/Ladung), C3 (*n*-Propylammonium, 31 Å²/Ladung) und TMA (Tetramethylammonium, 29 Å²/Ladung); Berechnung der Ladungsäquivalentflächen s. **Tab. 1**, Tabellenunterschrift a.

Werden diese Kationen in die passende Schichtverbindung interkaliert, kann osmotische Quellung hervorgerufen werden. Beispiele für solche Schichtverbindungen sind α-Zirconiumphosphat Zr({H}PO₄ (12 Å²/Ladung bzw. 8.3 Ladungen/nm²),^[38-39] Lepidokrokit-artiges Titanat {H_{0.8}} Ti_{1.2}Fe_{0.8}O₄ (14 Å²/Ladung bzw. 7.1 Ladungen/nm², Hydroxonium-interkaliertes {K_{0.8}} Ti_{1.2}Fe_{0.8}O₄),^[40-42] Kaliumhexaniobat {K₄} Nb₆O₁₇ (14 Å²/Ladung bzw. 7.1 Ladungen/nm²),^[25, 43] Calciumniobat {H} Ca₂Nb₃O₁₀ (15 Å²/Ladung bzw. 6.7 Ladungen/nm², Hydroxonium-interkaliertes {K} Ca₂Nb₃O₁₀),^[42, 44] Vermiculit (z.B. 38 Å²/Ladung bzw. 2.6 Ladungen/nm²)^{[35], [45]} oder Birnessit {H_{0.13}} MnO₂ (55 Å²/Ladung bzw. 1.8 Ladungen/nm², Hydroxonium-interkaliertes und oxidiertes {K_{0.45}} MnO₂);^[46-47] Berechnung der Ladungsäquivalentflächen s. **Tab. 1**, Tabellenunterschrift b. Anmerkung: die Interkalation der Organo-Kationen wird im Fall von Hydroxonium-interkalierten Schichtverbindungen durch tertiäre Amine als Base durchgeführt, bzw. für quartäre Ammoniumionen durch deren Hydroxidsalze als Base; Schichtsilicate sind unter sauren Bedingungen (die für die Hydroxonium-Interkalation notwendig sind) instabil.^[48]

Im Gegensatz zu den kleinen Li⁺- und Na⁺-Ionen weisen die genannten organischen Ionen Ladungsäquivalentflächen auf, welche die Ladungsäquivalentflächen der Schichtverbindungen systematisch überschreiten: bekannte osmotisch quellfähige Kombinationen aus Organo-Kationen und Schichtverbindung (**Tab. 1**, Zeilen 1 bis 9) sind dadurch gekennzeichnet, dass die Ladungsäquivalentfläche des Organo-Kations größer (oder im Rahmen der Genauigkeit) gleich der Ladungsäquivalentfläche der Schichtverbindung ist. Für das eher niedrig geladene {H_{0.13}} Mn^{III/IV}O₂ (55 Å²/Ladung) ist das sterisch anspruchsvolle TBA (90 Å²/Ladung) als osmotisch quellfähiges Zwischenschichtion bekannt (**Tab. 1**, Zeile 1). Dahingegen sind für höher geladene Schichtverbindungen mehrere auch deutlich kleinere Organo-Kationen bekannt, die osmotische Quellung hervorrufen. {H} Ca₂Nb₃O₁₀ (15 Å²/Ladung) beispielsweise quillt auch mit dem deutlich kleineren TMA (29 Å²/Ladung) als Zwischenschichtion osmotisch (**Tab. 1**, Zeile 9). Dies gibt einen ersten Hinweis auf eine sterische Komponente, die die osmotische Quellung von Organo-Zwischenschichtionen ermöglicht und darauf, dass die sterische Komponente auch von der Ladungsäquivalentfläche der Schichtverbindung abhängt.

Einleitung

Tab. 1: Einige osmotisch quellfähige Kombinationen von Organo-Kationen ($Z\text{-Kation}_{\text{Osm}}$) und Schichtverbindungen: Um repulsive osmotische Quellung auszulösen, müssen die $Z\text{-Kation}_{\text{Osm}}$ durch Kationenaustausch in die jeweilige Schichtverbindung interkaliert werden. Die $Z\text{-Kation}_{\text{Osm}}$ sind TBA (Tetrabutylammonium), DMAE (Dimethylammoniumethanol), C4 (*n*-Butylammonium), C3 (*n*-Propylammonium) und TMA (Tetramethylammonium). Der Kationenaustausch wird im Fall von Hydroxonium-interkalierten Schichtverbindungen durch die korrespondierenden tertiären Amine als Base durchgeführt, bzw. für quartäre Ammoniumionen durch deren Hydroxidsalze als Base.

	$Z\text{-Kation}_{\text{Osm}}$	Schichtverbindung (vor Kationenaustausch)	Ladungsäquivalentfläche		
			$Z\text{-Kation}_{\text{Osm}}^{\text{a})}$	Schicht ^{b)}	Austausch ^{c)}
			[$\text{\AA}^2/\text{Ladung}$]	[$\text{\AA}^2/\text{Ladung o. -OH}$]	[%]
1	{TBA}	Birnessit ^[46-47] {H _{0.13} } MnO ₂	90	55	~ 80 ^[46]
2	{TBA}	Calciumniobat ^[42, 44] {H} Ca ₂ Nb ₃ O ₁₀	90	15	~ 40 ^[42]
3	{TBA}	Lepidokrokit-artiges Titanat ^[40-41] {H _{0.8} } Ti _{1.2} Fe _{0.8} O ₄	90	14	~ 30 ^[49]
4	{TBA}	α -Zirconiumphosphat ^[38-39] Zr({H}PO ₄)	90	12	> 40 ^[38]
5	{DMAE}	Calciumniobat ^[42, 44] {H} Ca ₂ Nb ₃ O ₁₀	38	15	~ 60 ^[42]
6	{DMAE}	Lepidokrokit-artiges Titanat ^[40] {H _{0.8} } Ti _{1.2} Fe _{0.8} O ₄	38	14	~ 40 ^[40]
7	{C4}	Vermiculite ^[35, 45, 50] z.B. {Na,Mg} _{x=0.64} [Mg _{2.36} Fe _{0.48} Al _{0.16}] ^{0kt} <Si _{2.72} Al _{1.28} > ^{tetr} O ₁₀ (OH) ₂	37	38	≤ 100 ^[50]
8	{C3}	Kaliumhexaniobat ^[25, 43] {K ₄ } Nb ₆ O ₁₇	31	14	unbekannt
9	{TMA}	Calciumniobat ^[42, 44] {H} Ca ₂ Nb ₃ O ₁₀	29	15	~ 60 ^[42]

- a) Als Ladungsäquivalentfläche wurde die maximale Projektionsfläche der Kationen (Berechnung: Chemicalize.com^[51]) verwendet. Für C4 und C3 sind die Ladungsäquivalentflächen bekannt.^[12]
- b) Berechnet für die angegebenen Zusammensetzungen aus den zitierten Strukturdaten. Für Hydroxonium-interkalierte Schichtverbindungen mussten die Strukturdaten des jeweiligen Rohmaterials verwendet werden. Für Vermiculite: 24 $\text{\AA}^2/\text{x}$, s. Kap. 3.4.1).
- c) Anteil der interkalierten Organo-Kationen im Verhältnis zu der gesamten Anzahl an Ladungen bzw. OH-Gruppen.

In Einklang mit der vorangegangenen Auswertung der bekannten Literaturverbindungen wurde diskutiert, dass eine (bislang undefinierte) Mindestgröße derjenigen Organo-Kationen notwendig ist, die osmotische Quellung für ein bestimmtes schichtförmiges Titanat erlaubt.^[49] Dies hängt möglicherweise damit zusammen, dass eine gewisse Mindestseparation entgegen der elektrostatischen Attraktion überschritten werden muss, um das Einsetzen der repulsiven osmotischen Quellung zu erlauben.^[14] Passend hierzu können einige Vermiculite mit *n*-Butyl- und *n*-Propylammonium als Zwischenschichtkationen osmotisch quellen, jedoch nicht mit den kleineren Ethyl- und Methylammonium-Kationen.^[52] Die noch größeren *n*-Pentyl- und *n*-Hexylammonium-Kationen sind hingegen zu hydrophob für eine osmotische Quellung, was die schwierige Einstellung der attraktiven und repulsiven Komponenten unterstreicht und die repulsive Quellung von Vermiculiten mit *n*-Butylammonium „schwer zu verstehen“ macht.^[53]

Die Zusammenhänge zwischen der Art des Organo-Kations und der Ladungsdichte und dem daraus resultierenden Quellverhalten werden im Ergebnisteil dieser Arbeit (**Kap. 6.2.**) erörtert.

Eine weiterer Typ osmotisch quellfähiger Schichtverbindungen sei der Vollständigkeit wegen abschließend erwähnt: im Fall eines Antimonphosphates ($\{K_3\} Sb_3P_2O_{14}$, $11 \text{ \AA}^2/\text{Ladung}$, 9 Ladungen/nm^2)^[54] konnte durch Hydroxonium-Interkalation ($\{H_3\} Sb_3P_2O_{14}$) osmotische Quellung erreicht werden.^[21] Diese Quellung war jedoch nicht vollständig: ein signifikanter Teil des Materials wurde durch Sedimentation von dem delaminierten Gel abgetrennt und wurde nicht weiter untersucht.^[21] Eine schlüssige Erklärung der repulsiven Quellung dieser sauren Schichtverbindung ist daher schwierig. Auf Basis der verfügbaren Daten ist nicht zu beurteilen, welchen Assoziationsgrad die Schichtoberflächen-OH-Gruppen von Hydroxonium-interkalierten Schichtverbindungen pH-abhängig zeigen.

Einleitung

3.3.2. Suspensionen osmotisch gequollener Schichtverbindungen

Charakteristisch für kolloidale Suspensionen von repulsiv osmotisch gequollenen Schichtverbindungen ist, dass der Abstand zwischen benachbarten Lamellen durch den Volumenanteil der Schichtverbindung in der Suspension festgelegt ist (bei gegebener Ionenstärke). Dieses Verhalten wurde an 2:1 Schichtsilicaten^[14, 20] und an einem aufgereinigten, schichtförmigen Antimonphosphat^[21] detailliert untersucht. Eine kurze Rekapitulation von Ref. [14] erläutert die Grundlagen der Beschreibung von Suspensionen osmotisch gequollener Schichtverbindungen:

Wenn der Volumenanteil ϕ der 2:1 Schichten in wässriger Suspension $\phi > 2.5\%$ ist, besetzen die Schichten Gitterpunkte maximaler Separation (sogenannter Wigner-Kristall, **Abb. 3**). Der erwartete kristallographische d -Wert beträgt hier folglich:

$$d = \frac{t}{\phi} \quad (1)$$

wobei t die Dicke einer einzelnen Silicatschicht ist (9.6 Å).^[14] In diesem Konzentrationsbereich ist die Galeriehöhe h ($h = d - t$) kleiner als die *Debye*-Länge (κ^{-1}), d.h. die repulsiven elektrostatischen Wechselwirkungen der Schichten werden aufgrund ($h < \kappa^{-1}$) nicht abgeschirmt.^[14] In diesem Konzentrationsbereich kann die Vollständigkeit der osmotischen Quellung abgeschätzt werden: die Bestimmung der Trockenmasse der Suspensionen erlaubt unter der Annahme von *Bulk*-Dichten und der Annahme des Vorliegens einer absolut phasenreinen Schichtverbindung im Feststoffanteil die Berechnung des Volumenbruches. Damit kann überprüft werden, ob der erwartete d -Wert und der gemessene d -Wert übereinstimmen, wie es bei quantitativer Delaminierung durch osmotische Quellung der Fall ist (Übereinstimmung im Rahmen üblicher experimenteller Abweichungen). Die Abwesenheit von detektierbaren Reflexen von kristallinen Hydraten (typischerweise 10 bis 25 Å) alleine spricht nicht zwangsläufig für eine quantitative Delaminierung: röntgenographische Detektionsgrenzen von nicht-delaminierbaren kristallinen Hydraten variieren von Gerät zu Gerät und hängen von den Messbedingungen ab.

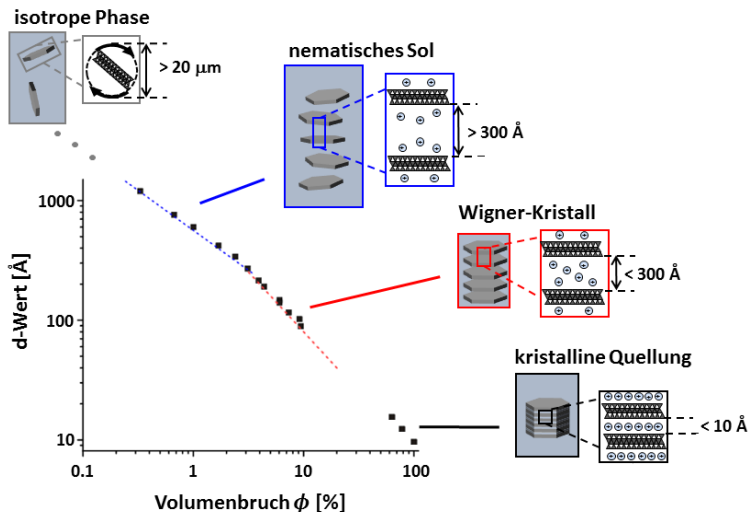


Abb. 3: Quellverhalten wässriger Suspensionen von $\text{Na}_{0.5}\text{-Smectit}$ ($\{\text{Na}_{0.5}\} [\text{Mg}_{2.5}\text{Li}_{0.5}]^{\text{oxt}}\text{<Si}_4\text{>}^{\text{tetra}}\text{O}_{10}\text{F}_2$) mit einem Durchmesser von $20 \mu\text{m}$. In Abhängigkeit des Volumenbruches des Smectites werden Bereiche unterschiedlicher Ordnung der Schichten durchlaufen. Die Graphik wurde im Vorfeld dieser Arbeit hauptsächlich von Dr. M. Stöter und Prof. Dr. J. Breu entworfen. *Adapted from Reference [14] with permission. Copyright (2016), American Chemical Society.*

Bei weiterer Verdünnung ($\phi < 2.5 \%$, $h > 300 \text{ \AA}$) „schmilzt“ dieser Wigner-Kristall und es wird ein nematisches Sol (**Abb. 3**) erhalten.^[14] Dieses zeigt zwischen gekreuzten Polarisatoren Doppelbrechung und kann – abhängig von ϕ – strukturelle Farben zeigen.^[21] Aufgrund der Abschirmung des elektrischen Potentials der Schichten ($h > \kappa^{-1}$) ist die Konzentrationsabhängigkeit des d -Wertes nun schwächer ausgeprägt (Details: Ref. [20] und Ref. [14]), makroskopische Phasenseparation tritt jedoch nicht auf.^[14] Die Abschirmung erlaubt eine gewisse Verkipfung der Schichten gegeneinander, was durch die Verbreiterung der Basal-Reflexe und durch die Auslöschung von Basal-Reflexen höherer Ordnung in der Röntgenkleinwinkelbeugung beobachtet werden kann.^[14] Die freie Drehbarkeit der Schichten wird zunächst durch die große laterale Ausdehnung der Schichten verhindert. Bei Verdünnungen $\phi < 0.15 \%$ kommt es zu einer Phasenseparation einer isotropen und einer nematischen Phase. Solche Separationen wurden bereits von Langmuir beobachtet^[55] und wurden bezugnehmend darauf von Michot im Detail untersucht.^[20, 56] Vollständig isotrope Suspensionen, die auch unter Scherung frei drehbare Plättchen aufweisen, werden für Verdünnungen von $\phi << 0.01 \%$ erhalten im Fall von $20 \mu\text{m}$ großen Plättchen.^[14] Isotrope Suspensionen und nematische Sole können im elektrischen oder magnetischen Feld ausgerichtet werden.^[57-59]

Suspensionen von osmotisch gequollenen Schichtverbindungen sind typischerweise bis zu Ionenstärken der Größenordnung 10 bis 100 mmol/L kolloidal stabil, wenn einwertige Ionen vorliegen.^[20-21, 60] Die Gegenwart zweiwertiger Kationen führt bereits bei Ionenstärken der Größenordnung 1 mmol/L zur Koagulation von delaminierten Schichtsilicaten.^[61]

Einleitung

3.4. Synthese von 2:1 Schichtsilicaten

Die Ladungsdichte einer Schichtverbindung kann ein Ausschlusskriterium für das Einsetzen der osmotischen Quellung sein. Daher ist es für grundlegende Untersuchungen essentiell, dass die Ladungsdichte eingestellt werden kann und über das gesamte Probenvolumen möglichst homogen verteilt ist. Eine Verbindungsklasse, die diese Voraussetzungen erfüllt, sind die 2:1 Schichtsilicate, wenn sie unter geeigneten Bedingungen entstanden sind.^[62] In diesem Zusammenhang weist die Schmelzsynthese insbesondere gegenüber der weitverbreiteten Nieder-temperatur-Hydrothermalsynthese einige Vorteile auf, was in diesem Kapitel rekapituliert wird.^[63-68] Die Homogenität der Ladungsdichteverteilung hängt davon ab, wie homogen die isomorphen Substitutionen im Kristall verteilt sind. Hierfür sind während der Entstehung der Schichtsilicate Temperaturen > 1000 K notwendig, um feste Lösungen zu erhalten.^[69] Dieser Umstand wurde ausgenutzt, um Schichtsilicate homogener Ladungsverteilung aus der Schmelze mit nachfolgendem Temperiern zu synthetisieren (alle Syntheseschritte > 1000 K).^[15] Die Größe der erhaltenen Schichtsilicat-Kristallite hängt nicht nur von der Homogenität der chemischen Zusammensetzung ab, sondern auch vom Betrag der Ladungsdichte. Hochgeladene Schichtsilicate weisen im Allgemeinen größere laterale Ausdehnungen auf als niedrig geladene.^[70-72] Gleichzeitig weisen Schichtsilicate hoher Ladungsdichte einen geringeren Grad an turbostratischer Fehlordnung auf (Translations- und/oder Rotationsfehlordnung der aufeinanderfolgenden Schichten in einem Stapel) als Schichtsilicate niedriger Ladungsdichte.^[73] Dies ist auf die mit steigender Schichtladung zunehmend eingeschränkten Fehlordnungsmöglichkeiten zurückzuführen, aufgrund von zunehmender Besetzung der hexagonalen Kavitäten mit Zwischenschichtionen.^[73] Dass der Grad der Besetzung der hexagonalen Kavitäten die Partikelgröße beeinflusst, wurde von *Meunier* unter anderem darauf zurückgeführt, dass die Nukleation gegenüber dem Kristallwachstum im Allgemeinen durch Fehlordnung stärker bevorzugt wird.^[72]

3.4.1. Isomorphe Substitution

Im Gegensatz zu Lepidokrokit-artigen Titanaten, schichtförmigem Birnessit oder schichtförmigen Niobaten (die unter geeigneten Bedingungen ebenfalls osmotisch quellen können, **Tab. 1**), lässt die Struktur der 2:1 Schichtsilicate eine beachtliche Zahl an realisierbaren isomorphen Substitutionen und Ladungsdichten zu.^[15, 27, 74-78] Durch isomorphe Substitution in der Oktaeder- und der Tetraederschicht wird eine permanente negative Ladung erzeugt, die durch Zwischenschichtkationen ausgeglichen wird. Während die Ladungsdichte durch isomorphe Substitution variiert werden kann, beträgt die Fläche, die pro Formeleinheit O₁₀(OH/F)₂ zur Verfügung steht, für viele isomorphe Substitutionen konstant ca. 24 Å².^[12] Daher wird für

2:1 Schichtsilicate als Ladungsdichte häufig eine Schichtladung in der Form x [Ladungen] pro Formeleinheit $O_{10}(OH/F)_2$ angegeben (x p.f.u., *per formula unit*, Ladungsäquivalentfläche: $24 \text{ \AA}^2/x$). Häufige isomorphe Substitutionspfade sind (hier ausgehend von Talk $[Mg_3]^{okt} < Si_4 >^{tetr} O_{10}(OH/F)_2$ dargestellt):

- 1) $[Mg^{II}]^{okt} \rightarrow [Li^{I}]^{okt}$
- 2) $[Mg^{II}]^{okt} \rightarrow [M^{II}]^{okt}$
- 3) $[Mg^{II}]^{okt} \rightarrow [M^{III}]^{okt}$
- 4) $[Mg^{II}]^{okt} \rightarrow [\square]^{okt}$
- 5) $<Si^{IV}>^{tetr} \rightarrow <Al^{III}>^{tetr.}$
- 6) $<Si^{IV}>^{tetr} \rightarrow <Fe^{III}>^{tetr.}$

Kombinationen von diesen Substitutionen führen zu 2:1 Schichtsilikaten unterschiedlicher Zusammensetzung der Schichtladung x:



Die in natürlichen Schichtsilikaten am häufigsten gefundenen Oktaederkationen (M) sind Al^{III} , Fe^{III} , Mg^{II} , Fe^{II} und Mn^{II} .^[72] Einige Einschränkungen für die isomorphen Substitutionen sind:

- 1) $x \leq 2$
- 2) $c \leq 1$
- 3) $0 \leq d \leq 1$
- 4) $e + f \leq 2$ (s. Löwenstein-Regel^[79])

Leider sind über diese Einschränkungen hinaus nicht beliebige Substitutionen synthetisch zugänglich oder in der Natur vorhanden. Ein Überblick über > 6000 natürlich vorkommende Substitutionen in Glimmern ($x \sim 1$, nicht-quellfähig) wird von Tischendorf^[80] gegeben und einige Arbeiten haben sich mit synthetisch zugänglichen 2:1 Schichtsilikaten beschäftigt.^[15, 73, 77, 81-86] Probleme können durch Mischungslücken oder mehrphasige Schmelzen und hohe Viskositäten bei Schmelzsynthesen entstehen, was viele Herausforderungen auf diesem Gebiet bietet. Einen Beitrag zur Diskussion zugänglicher Substitutionen stellt **Kap. 6.4.** dar, während in **Kap. 6.1** bis **Kap. 6.3.** bereits etablierte Substitutionen der Form $\{Na_x\} [Mg_{3-x}Li_x]^{okt} < Si_4 >^{tetr} O_{10}F_2$ verwendet werden.

3.5. Anwendungen von Nanoschichten

3.5.1. Polymernanokomposite

Eine prominente Anwendung von impermeablen Nanoschichten mit hohem Aspektverhältnis ist die Herstellung von Polymernanokompositen für Gasbarrieren. Das Prinzip dieser Anwendung kann durch das Cussler-Modell beschrieben werden (**Abb. 4**, *tortuous path*).^[87]

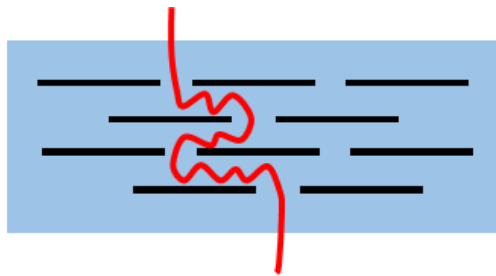


Abb. 4: Verlängerter Perkolationspfad (*tortuous path*) nach dem Cussler-Modell^[87] in Polymernanokompositen mit Hochaspektverhältnis-Materialien als Füllstoff (Blau: Polymermatrix, schwarz: Füllstoff, rot: schematischer Perkolationspfad eines Permeatmoleküls).

Zur Herstellung solcher Komposite kann beispielsweise eine Suspension aus vollständig delaminierten Nanoschichten und gelöster Polymermatrix als nematisches Sol (**Kap. 3.3.2.**) aufgetragen und getrocknet werden. Der resultierende Barriere-Lack weist eine erhöhte Gasbarriere gegenüber der reinen Polymermatrix auf. Hier ist der Idealfall skizziert, in dem keine Phasenseparation im Kompositmaterial auftritt.

Die Flexibilität von einzelnen Nanoschichten wurde vorhergesagt^[88] und experimentell bestätigt^[89] und ist im Polymernanokomposit durch die mechanische Entkopplung der Nanoschichten durch die Polymermatrix gegeben. Dies stellt einen Vorteil gegenüber den weitverbreiteten Barriere-Materialien SiO_x bzw. Al_2O_3 dar. Diese sind zwar ebenfalls für Gase impermeabel, sind aber auch spröde auf Grund ihrer dreidimensionalen Kristallinität. Damit werden durch wiederholte mechanische Verformung solcher SiO_x - bzw. Al_2O_3 -Filme Brüche möglich, womit die Gasdiffusion durch die entstehenden Defekte dominiert wird (vgl. Ref. [90] und Ref. [91]). Die Brüche durch wiederholte mechanische Verformung und die resultierende Permeabilität sind möglicherweise der Grund dafür, dass bereits im Jahr 2013 flexible OLED-Displays vorgestellt wurden (*Consumer Electronics Show*), aber bis heute nicht in einer Form in Serie verfügbar sind, in der sie auch der Endkunde verformen kann. Die Anforderungen an die Barriere sind aufgrund der Empfindlichkeit der OLED gegenüber Sauerstoff und Wasserdampf sehr hoch.^[92] Polymernanokomposite auf Schichtsilicat-Basis sind flexibel und verformbar. Einige weisen Barriere-Eigenschaften auf, die nahe an den Barriere-Anforderungen für flexible OLEDs liegen.^[16, 93]

3.5.2. Heterostrukturen

Heterostrukturen aus unterschiedlichen Nanoschichten

Zwei oder mehr chemisch verschiedene Nanoschichten können durch Stapelung zu Heterostrukturen verarbeitet werden. Hierbei besteht die Hoffnung, eine Vielfalt an neuen Materialeigenschaften durch Synergieeffekte bei der Kombination von unterschiedlichen Nanoschichten zu erreichen.^[94] Für die atomeffiziente Herstellung solcher Strukturen ist die Kontrolle über die Schichtdicke durch quantitative repulsive Delaminierung notwendig.

Eine Auftragungsmethode, die Kontrolle über die Anzahl und die Art der Schichten in Stapelrichtung in mehreren Auftragungsschritten ermöglicht, ist die Langmuir-Blodgett-Technik. Auf diese Weise wurde durch Kombination von zwei repulsiv delaminierten Nanoschichten (die beide jeweils paraelektrisch sind) eine ferroelektrische Heterostruktur erhalten ($\text{LaNb}_2\text{O}_7^- \{\text{Z}^+\} / \text{Ca}_2\text{Nb}_3\text{O}_{10}^- \{\text{Z}^+\}$).^[95]

Darüber hinaus versprechen Heterostrukturen die Miniaturisierung elektrischer Bauteile: Die Kombination der Nanoschichten $\text{Ru}_{0.95}\text{O}_2^{0.2-} \{\text{Z}_{0.2}^+\} / \text{Ca}_2\text{Nb}_3\text{O}_{10}^- \{\text{Z}^+\} / \text{Ru}_{0.95}\text{O}_2^{0.2-} \{\text{Z}_{0.2}^+\}$ ist metallisch leitfähig / isolierend / metallisch leitfähig und erlaubt die Herstellung von Nano-Kondensatoren mit Kapazitäten von ca. $27.5 \mu\text{F}/\text{cm}^2$.^[96]

Interkalations-Heterostrukturen durch Ionenaustausch

Der Zwischenschichtraum von Schichtverbindungen kann durch geeignete Kationen funktionalisiert werden (z.B. Mikroporösität,^[97] Belegung durch optische Emittoren^[98]). Durch alternierende Besetzung der Zwischenschichträume in Stapelrichtung können geordnete Wechsellagerungen ($\{\text{Kation-A}\} - [2:1 \text{ Schicht}] - \{\text{Kation-B}\} - [2:1 \text{ Schicht}]$) erhalten werden.^[99-100] Dies entspricht Heterostrukturen in Form von alternierenden Nano-Reaktionsräumen, die durch eine ca. 1 nm dicke 2:1 Schicht voneinander getrennt sind; dieser Zustand der geordneten Wechsellagerung ist unter geeigneten Synthesebedingungen thermodynamisch gegenüber der statistischen Wechsellagerung bevorzugt.^[101] Die thermodynamische Stabilität resultiert aus einer Segregation der Kationendichten für die beiden Kationensorten (die Kationenaustauschkapazität wird alternierend über- und unterschritten).^[101] Erforderlich für die Synthese ist ein stöchiometrisch kontrollierter, partieller Kationen-Austausch, der an das Verteilungsgleichgewicht zwischen gelösten und interkalierten Ionen angepasst ist (weitere Details: Ref. [101]).

Solche Heterostrukturen können in einer Schicht labil gegenüber osmotischer Quellung in Wasser sein, während die andere Schicht stabil gegenüber osmotischer Quellung in Wasser ist und eine weitere Funktionalisierung aufweist (Beispiel: $\{\text{Na}\} - [2:1 \text{ Schicht}] - \{\text{Farbstoff-Ka-}$

Einleitung

tion} - [2:1 Schicht]).^[102] Durch repulsive osmotische Quellung der {Na}-Ionen werden delaminierte „Sandwich“-Strukturen ([2:1 Schicht] - {Farbstoff-Kation} - [2:1 Schicht]) erhalten, die den hydrophoben Farbstoff in anorganisch-organischen Hybridpigmenten in wässriger Suspension kolloidal stabilisieren.^[102]

In **Kap. 6.1.** wird eine Heterostruktur ({Na} - [2:1 Schicht] - {C4} - [2:1-Schicht]) mit hoher Ladungsdichte synthetisiert, die osmotisch quellfähig ist und keine „Sandwich“-Strukturen als Endprodukt liefert, sondern einzelne delaminierte Nanoschichten. Die homoionischen Randphasen (reine {Na}- bzw. {C4}-Form) hingegen können nicht osmotisch quellen. Damit ist dies ein Beispiel für Synergieeffekte in Heterostrukturen.

3.6. Problemstellung

Das wirtschaftliche Interesse an flexiblen und transparenten Barrierelacken (auf Basis von Nanoschichten Struktur-inhärenter Dicke) dient in dieser Arbeit als Motivation, um die Bedingungen die das Einsetzen der osmotischen Quellung erlauben näher zu beleuchten. Daraus sollen einfache und robuste Methoden zur Herstellung nematischer Sole aus Nanoschichten abgeleitet werden. In diesem Zusammenhang sind bislang insbesondere Ladungsdichte-übergreifende Untersuchungen vernachlässigt worden.

Synthetische 2:1 Schichtsilicate der Summenformel $\{Z^{a+}\}_{x/a} [Mg_{3-x}Li_x]^{0kt} < Si_4 >^{tetr} O_{10}F_2$ bieten die Möglichkeit die Ladungsdichte durch isomorphe Substitution gezielt zu variieren. Dies ermöglicht Ladungsdichte-übergreifende Untersuchungen bei vergleichbarer chemischer Zusammensetzung. Im Hinblick auf weitere zukünftige Anwendungen sollen die Möglichkeiten weiterer Funktionalisierung der 2:1 Schichten durch isomorphe Substitution mit Übergangsmetallen diskutiert werden.

Das Konzept dieser Arbeit basiert auf den folgenden präparativen Schritten:

- Synthese von 2:1 Schichtsilikaten
 - Variation der Schichtladung
- Charakterisierung der 2:1 Schichtsilikate
 - Homogenität der Ladungsdichte, der Reinheit und der lateralen Ausdehnung
- Interkalationsverbindungen und osmotische Quellung
 - Synthese einer Heterostruktur durch partiellen Kationenaustausch
 - Systematische Kombinationen von Kationen und Ladungsdichten
 - Ladungsdichte-übergreifende Delaminierung
- Untersuchung der isomorphen Substitution der 2:1 Schichtsilicatstruktur mit Eisen
 - Einkristall-Struktur Analyse
 - Bestimmung der Leitfähigkeit

Synopsis

4. Synopsis

Die vorliegende kumulative Dissertation enthält vier Manuskripte. Die ersten drei Manuskripte beschreiben neue Erkenntnisse über die repulsive osmotische Quellung und deren verständnisbasierte Ladungsdichte-übergreifende Anwendung. Das letzte Manuskript trägt zur Diskussion der Funktionalisierung der 2:1 Schicht durch isomorphe Substitution bei (graphische Synopsis aller Manuskripte: **Abb. 5**).

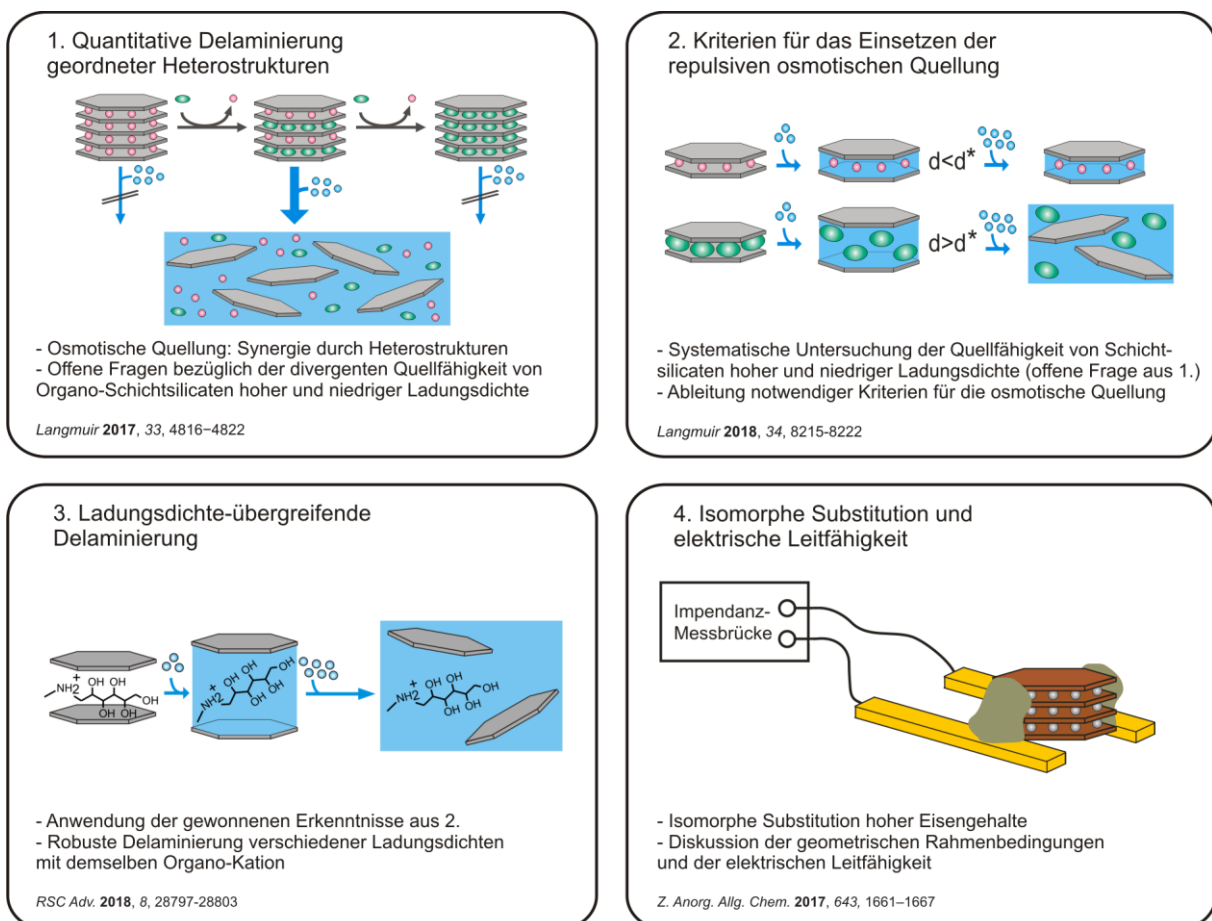


Abb. 5: Graphische Synopsis und Kommentare zum Zusammenhang der Kapitel dieser Arbeit.

Als erstes Teilergebnis wird in **Kap. 6.1.** das Quellverhalten einer Interkalations-Heterostruktur besprochen und ein möglicher Mechanismus ihrer osmotischen Quellung diskutiert. Dies wirft weiterhin Fragen bezüglich der divergenten Quellfähigkeit von Organo-Schichtsilikaten hoher und niedriger Ladungsdichte auf.

Daran schließt sich in **Kap. 6.2.** die systematische Untersuchung der kristallinen und repulsiv osmotischen Quellfähigkeit von unterschiedlichen Ladungsdichten in Kombination mit verschiedenen Organo-Zwischenschichtionen an. Hieraus werden Einblicke in notwendige Bedingungen für die repulsive osmotische Quellung erhalten.

Synopsis

Diese Erkenntnisse werden in **Kap. 6.3.** angewendet, um eine robuste Methode zu entwickeln, die die quantitative Delaminierung durch repulsive osmotische Quellung Ladungsdichte-übergreifend erlaubt, was auch für ladungsheterogene Systeme gilt. Dies senkt die Anforderungen an das Ausgangsmaterial bezüglich Ladungshomogenität und suggeriert, dass osmotische Quellung unabhängig von der Ladungsdichte möglich sein könnte, wenn das Zwischenschichtion entsprechend an die Ladungsdichte angepasst wird.

Im Hinblick auf potentielle Anwendungen wird in **Kap. 6.4.** ein 2:1 Schichtsilicat untersucht, das reich an oktaedrischem Eisen ist. Die geometrischen Rahmenbedingungen der isomorphen Substitution von Eisen werden anhand der Einkristallstruktur diskutiert und der Einfluss dieser Substitution auf die elektrische Leitfähigkeit wird bestimmt.

Synopsis

4.1. Quantitative Delaminierung geordneter Heterostrukturen

Über osmotische Quellung von 2:1 Schichtsilicaten ist bekannt, dass sie von niedrig geladenen {Na}-Smectiten einer Schichtladung von $x < 0.55$ p.f.u. (< 2.3 Ladungen/nm² bzw. > 43 Å²/Ladung) in Wasser realisiert wird,^[32] während {Na}-Schichtsilicate höherer Schichtladung dafür eine zu starke elektrostatische Attraktion aufweisen. Darüber hinaus ist bekannt, dass hochgeladene {C4}-Vermiculite (typischerweise $x > 0.65$ p.f.u.) repulsiv quellen, während dies für {C4}-Smectite trotz ihrer geringeren Schichtladung nicht möglich ist.^[52]

Für die Untersuchung des Quellverhaltens einer Interkalations-Heterostruktur aus diesen beiden Ionen (Na⁺ und C4) wurde ein 2:1 Schichtsilicat der Summenformel {Na_{0.6}} [Mg_{2.4}Li_{0.6}]^{okt}<Si₄>^{tetr}O₁₀F₂ ($x = 0.6$ p.f.u.) als Ausgangsmaterial verwendet, dessen Schichtladung per Definition zwischen den Smectiten und den Vermiculiten liegt.^[5] Pulverdiffraktometrie, Kationenaustauschkapazität, spektroskopische Analyse und die Bestimmung der Ladungsäquivalentfläche über Interkalationsreaktionen bestätigen eine hohe Reinheit und das Vorliegen der angegebenen Zusammensetzung. Die homoionische {Na}-Randphase delaminiert in Übereinstimmung mit oben genanntem Literaturbefund aufgrund $x > 0.55$ p.f.u. nicht, die kristalline Quellung ist auch in Wasser auf $d = 15.1$ Å limitiert. Ähnliches wird für die homoionische {C4}-Randphase beobachtet, hier ist die kristalline Quellung auf $d = 14.7$ Å limitiert.

Die Herstellung einer Heterostruktur durch partiellen Kationen-Austausch mit C4 gelang in einem Ethanol-Wasser-Gemisch (1:1) und weist die mittlere Zusammensetzung {Na_{0.33}C_{4.0.27}} [Mg_{2.4}Li_{0.6}]^{okt}<Si₄>^{tetr}O₁₀F₂ auf. Die hohe kristallographische Ordnung dieser Heterostruktur ({Na} - [2:1 Schicht] - {C4} - [2:1 Schicht]) in Stapelrichtung wird durch Pulverdiffraktogramme bestätigt.

Die intrakristalline Reaktivität dieser Heterostruktur bezüglich Quellung unterscheidet sich signifikant von der Reaktivität der homoionischen Randphasen: Die dort beobachtete Limitierung auf kristalline Quellung gilt hier nicht, vielmehr wurde für die Heterostruktur quantitative Delaminierung durch repulsive osmotische Quellung in einzelne Lamellen nachgewiesen (Röntgenkleinwinkelbeugung, Rasterkraftmikroskopie). Dies ist ein Beispiel für synergistische Effekte durch Heterostrukturen, da keine der homoionischen Randphasen über den kristallinen Bereich hinaus quellfähig ist. Des Weiteren stellt der partielle Ionenaustausch eine atomeffiziente Methode zur Delaminierung dar.

Als Mechanismus wird ein zweistufiger Prozess vorgeschlagen (**Abb. 6**), in dem die {Na}-Zwischenschichträume zunächst osmotisch zu „Sandwich“-Aggregaten der Form

([2:1 Schicht] - {C4} - [2:1 Schicht]) quellen. Hierfür spricht, dass die Hydrophilie von Na^+ größer als die von C4 ist und dass die Quellung bei hohen Luftfeuchten für den {C4}-Zwischen-schichtraum der Heterostruktur auf $d = 14.7 \text{ \AA}$ limitiert ist. Dahingegen zeigen Organo-Zwi-schenschichträume, wenn sie osmotisch quellfähig sind, immer exzessive kristalline Quellung ($d \gtrsim 17.5 \text{ \AA}$) bei hohen Luftfeuchten (s. **Kap. 6.2.**). Die „Sandwich“-Struktur ([2:1 Schicht] - {C4} - [2:1 Schicht]) zerfällt schließlich in einzelne Lamellen. Der Grund hier-für kann sein, dass Na^+ aus der diffusen Doppelschicht mit C4 um die verbleibenden Zwischen-schichtpositionen konkurriert und die „Sandwich“-Strukturen quellfähiger macht.

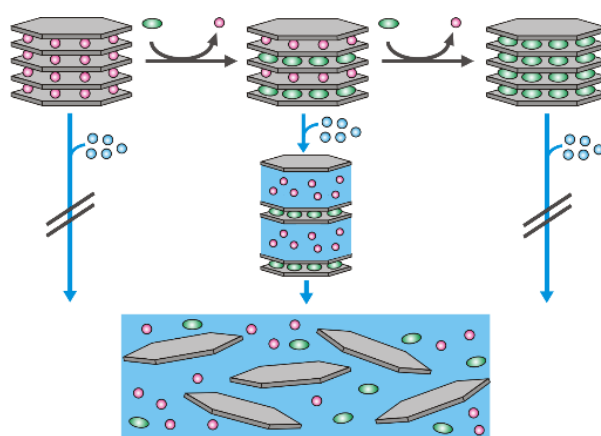


Abb. 6: Vorgeschlagener Mechanismus für die Delaminierung der Heterostruktur.

In einem allgemeinen Ansatz, der nicht auf n -Alkylammoniumionen limitiert ist, wird im Fol-gekapitel untersucht, weshalb - wie auch hier beobachtet - Organo-Schichtsilicate hoher La-dungsdichte eine höhere intrakristalline Reaktivität aufweisen als ihre niedriger geladenen Äquivalente.

Synopsis

4.2. Kriterien für das Einsetzen der repulsiven osmotischen Quellung

Eine Erklärung für das Einsetzen der osmotischen Quellung der hochgeladenen {C4}-Vermiculite wurde von *Lagaly* vorgeschlagen.^[53] Diese beruht darauf, dass die hohe Ladungsdichte die *n*-Butylammoniumkette in eine „Paraffin-artige“ Orientierung zwingt (schräg zur Oberflächennormalen stehend). Dies sei eine hydrophilere Anordnung als die flachliegende Kette in niedrig geladenen {C4}-Smectiten. Da auch andere Organo-Kationen als *n*-Alkylammoniumionen osmotische Quellung hervorrufen können, wäre eine allgemeinere Erklärung wünschenswert. Dazu trägt dieses Kapitel bei.

In dieser Arbeit wurden Kombinationen verschiedener Ladungsdichten mit unterschiedlichen Zwischenschichtkationen untersucht. Hierzu wurden zwei synthetische 2:1 Schichtsilicate ($\{\text{Na}_x\} [\text{Mg}_{3-x}\text{Li}_x]^{\text{oxt}} \langle \text{Si}_4 \rangle^{\text{tetra}} \text{O}_{10}\text{F}_2$) synthetisiert, deren Schichtladung jeweils im Bereich der Smectite ($x = 0.5$ p.f.u., $48 \text{ \AA}^2/\text{Ladung}$) und im Bereich der Vermiculite liegt ($x = 0.7$ p.f.u., $34 \text{ \AA}^2/\text{Ladung}$). Die hohe Reinheit dieser Silicate und die angegebene Schichtladung wurde durch Pulverdiffraktometrie, Kationenaustausch und die Bestimmung der Ladungsäquivalentfläche über Interkalationsreaktionen bestätigt.

Das Quellverhalten der beiden {Na}-Schichtsilicate in Wasser steht im Einklang mit Literaturbefunden.^[14, 32] Nur {Na}-Smectit ist osmotisch quellfähig ($x = 0.5$ p.f.u.), während {Na}-Vermiculit auf den kristallinen Quellbereich ($d = 15.1 \text{ \AA}$) beschränkt ist ($x = 0.7$ p.f.u., aufgrund seiner hohen Schichtladung hier als Vermiculit bezeichnet). Dieses Bild kehrt sich nach Interkalation von Organo-Kationen um. Die verwendeten Ionen sind *n*-Butylammonium (C4, $37 \text{ \AA}^2/\text{Ladung}$), 2-Ammonium-2-(hydroxymethyl)-1,3-propandiol (TRIS, $37 \text{ \AA}^2/\text{Ladung}$), Diethylammoniummethanol (DEAE, $41 \text{ \AA}^2/\text{Ladung}$) und 2-(Trimethylammonium)ethylmethacrylat (TMAEMA, $60 \text{ \AA}^2/\text{Ladung}$). Die Organo-Vermiculite ($34 \text{ \AA}^2/\text{Ladung}$) quellen repulsiv osmotisch, während die Organo-Smectite ($48 \text{ \AA}^2/\text{Ladung}$) auch in entsalztem Wasser nur kristalline Quellung mit Zwischenschichtabständen von $d < 17.5 \text{ \AA}$ ($q > 0.36 \text{ \AA}^{-1}$) zeigen (**Abb. 7**).

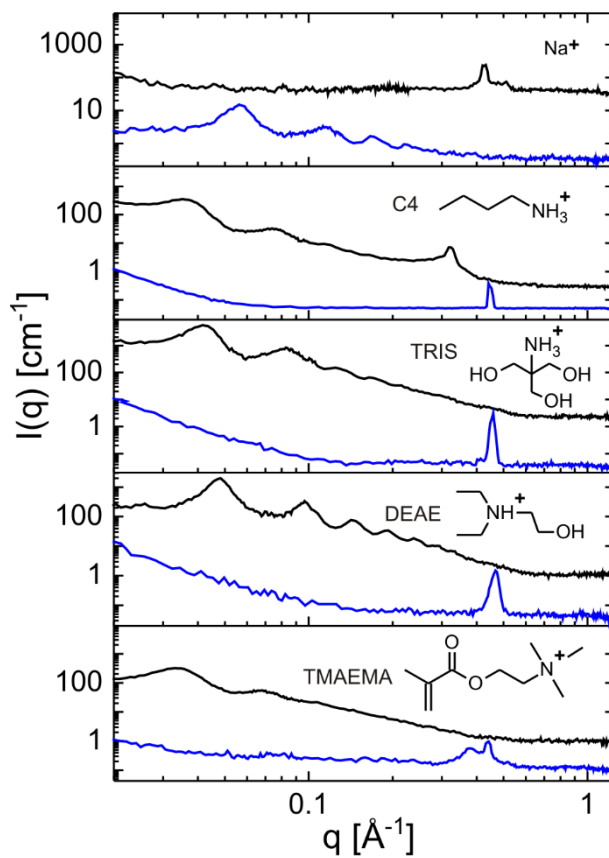


Abb. 7: Röntgenkleinwinkelbeugung der unterschiedlich geladenen Schichtsilicate in wässriger Suspension (blau: Smectit mit $x = 0.5$ p.f.u., schwarz: Vermiculit mit $x = 0.7$ p.f.u.). Die Zwischenschichtionen sind Na^+ , C4, TRIS, DEAE, TMAEMA (von oben nach unten). Osmotische Quellung wird nur für den niedrig geladenen $\{\text{Na}\}$ -Smectit und die hochgeladenen Organo-Vermiculite beobachtet (Reflexe bei $q < 0.06 \text{ \AA}^{-1}$, $d > 100 \text{ \AA}$, nähere Diskussion der Volumenbruch-abhängigen d -Werte in Kap. 6.2.).

Dieses Verhalten wird auch in der kristallinen Quellung wiedergegeben (Schichtabstand der trockenen Proben im Vergleich zu Messungen bei 98 % Luftfeuchte, $\Delta d = d_{98\% \text{Luftfeuchte}} - d_{\text{trocken}}$). Auch hier zeigen Organo-Vermiculite systematisch ein stärker ausgeprägtes Quellverhalten als Organo-Smectite. Ein Blick auf die Ladungsäquivalentflächen macht deutlich, dass für alle Organo-Vermiculite das Verhältnis der Ladungsäquivalentflächen von Interkalat (A_I) und Silicat (A_C) größer als 1 ist. $A_I/A_C \gtrsim 1$ beschreibt den „sterischen Druck“ der Organo-Vermiculite, da unter diesen Umständen eine Besetzung des Zwischenschichttraumes mit (flach liegenden) Monolagen nicht mehr ausreichend ist um Elektroneutralität zu gewährleisten, insbesondere wenn erste Wassermoleküle aufgenommen werden. Dies verursacht exzessive kristalline Quellung der Organo-Vermiculite bei hohen Luftfeuchten. Die exzessive kristalline Quellung ist dadurch gekennzeichnet, dass der d -Wert um $\Delta d \gtrsim 3.5 \text{ \AA}$ zunimmt. Δd ist ein Maß für die Hygroskopizität der Interkalationsverbindung sowie den sterischen Druck durch Wasseraufnahme. Ein weiteres Kennzeichen ist das Erreichen eines absoluten d -Wertes von $d^* \gtrsim 17.5 \text{ \AA}$ bei 98% Luftfeuchte. Abhängig von der Funktionalisierung des Zwischenschichtions könnten

Synopsis

unterschiedlich hohe Separationen d^* notwendig werden: für besonders hydrophile Zwischenschichtionen mit einer hohen Dichte an Hydroxylgruppen wie TRIS ist bereits eine geringere Separation als beispielsweise für TMAEMA ausreichend, um osmotische Quellung in Wasser sicherzustellen. Für die meisten Organo-Smectite hingegen ist $A_l/A_c < 1$ und eine exzessive kristalline Quellung kann für keinen der Organo-Smectite beobachtet werden.

Von allen drei notwendigen Kriterien für das Einsetzen der repulsiven osmotischen Quellung ($A_l/A_c \gtrsim 1$, $\Delta d \gtrsim 3.5 \text{ \AA}$, $d^* \gtrsim 17.5 \text{ \AA}$) ist das Letzte – die Überschreitung eines Mindest- d -Wertes – ein essentieller Beitrag, um die attraktiven Wechselwirkungen entscheidend zu schwächen.

Diese Ergebnisse erklären allgemein, weshalb als Delaminierungsmittel bekannte Organo-Kationen nur hoch geladene Vermiculite osmotisch quellen lassen, wohingegen dieselben Organo-Kationen keine Smectite delaminieren, trotz deren niedriger Schichtladung. Die hier gewonnenen Erkenntnisse werden im nächsten Teil der Arbeit angewendet um eine Ladungsdichte-übergreifende Delaminierung zu erreichen.

4.3. Ladungsdichte-übergreifende Delaminierung

Die osmotische Quellung von niedrig geladenen Organo-Smectiten ist bislang nicht bekannt. Basierend auf den Einblicken in die Bedingungen, die repulsive osmotische Quellung von Organo-Vermiculiten erlauben, wurde in diesem Kapitel ein sterisch anspruchsvoller Ammoniumzucker (z.B. *N*-Methyl-*D*-glucammonium (Meglumin), 77 Å²/Ladung) als Organo-Kation identifiziert, das erstmals Ladungsdichte-übergreifend sowohl niedrig geladene Smectite als auch hochgeladene Vermiculite delaminieren lässt. Vier synthetische 2:1 Schichtsilicate ($\{Z^{a+}\}_{x/a} [Mg_{3-x}Li_x]^{okt} < Si_4 >^{tet} O_{10}F_2$) mit $x = 0.3, 0.4, 0.5$ und 0.7 p.f.u. (entsprechend 79, 59, 48 und 34 Å²/Ladung) wurden zur Interkalation mit Meglumin verwendet. Die Reinheit und das Vorliegen der angegebenen Schichtladungen wurde durch Pulverdiffraktometrie, Kationenaustausch und die Bestimmung der Ladungsäquivalentfläche über Interkalationsreaktionen bestätigt.

Das Verhältnis der Ladungsäquivalentflächen von Interkalat (Meglumin) und Silicat beträgt selbst für die niedrigste Schichtladung $A_I/A_C \gtrsim 1$. Deswegen und aufgrund der hohen Hygrokopizität von Meglumin weisen alle Schichtladungen exzessive kristalline Quellung ($\Delta d \gtrsim 3.5$ Å, $d^* \gtrsim 17.5$ Å) bei 98 % Luftfeuchte auf. Dieses Verhalten wurde in **Kap. 6.2.** als notwendige Bedingung für das Einsetzen der osmotischen Quellung in Wasser identifiziert und tatsächlich setzt repulsive osmotische Quellung für alle Schichtladungen ein.

Da die osmotische Quellung mit Meglumin für einen solch breiten Bereich an Schichtladungen möglich ist, ist dies auch für Systeme möglich, die aufgrund von Ladungsheterogenität nicht vollständig osmotisch quellen können. Dies ist der Fall für einen nicht-getemperten {Na}-Smectit der Schichtladung $x = 0.5$ p.f.u.. Im Gegensatz zu dem getemperten (ladungshomogenen) Material kann dieser nicht vollständig osmotisch in Wasser quellen. Kationenaustausch mit Meglumin ersetzt daher im Hinblick auf quantitative Delaminierung den aufwändigen Temper-Schritt (6 Wochen im gasdichten Molybdän-Tiegel bei 1045°C). Hiermit sinken die Anforderungen an 2:1 Schichtsilicate als Barriere-Füllstoffe für Polymernanokomposite beträchtlich: der Wert der Ladungsdichte und deren Homogenität sind keine limitierenden Faktoren mehr bezüglich der vollständigen Delaminierung in die benötigten Hochaspektverhältnis-Nanoschichten.

Die Resultate aus **Kap. 6.2.** und **Kap. 6.3.** suggerieren, dass diese Überlegungen auch auf andere Schichtverbindungen unabhängig von ihrer Ladungsdichte übertragen werden könnten, wenn die Organo-Kationen an die betreffende Schichtladung angepasst und erfolgreich interkaliert werden können.

Synopsis

4.4. Isomorphe Substitution und elektrische Leitfähigkeit

Im Hinblick auf spätere Anwendungen, beispielsweise in Heterostrukturen, soll die 2:1 Schicht durch isomorphe Substitution weiter funktionalisiert werden. Das Einbringen von Übergangsmetallen verspricht die elektrische Leitfähigkeit in der 2:1 Schicht zu erhöhen.

In diesem Teil der Arbeit wurde daher ein Ferro-Kinoshitalit (nominelle Zusammensetzung: $\{\text{Ba}\} [\text{Fe}_3]^{\text{oxt}} < \text{Si}_2\text{Al}_2 >^{\text{tetr}} \text{O}_{10}\text{F}_2$; gefundene Zusammensetzung: $\{\text{Ba}_{0.96}\} [\text{Fe}_{2.68}\text{Al}_{0.28}]^{\text{oxt}} < \text{Si}_{2.01} \text{Al}_{1.99} >^{\text{tetr}} \text{O}_{10}\text{F}_2$) aus der Schmelze synthetisiert. Dessen Fe^{III} -Gehalt beträgt ca. 6 % des gesamten Eisenanteils. Die geometrischen Rahmenbedingungen dieser isomorphen Substitution werden anhand der Einkristallstrukturanalyse durch einen Vergleich mit bereits publizierten Kristallstrukturen diskutiert. Hierzu werden eisenreiche 2:1 Schichtsilicate und ein eisenfreies 2:1 Schichtsilicat mit ähnlicher chemischer Zusammensetzung der Tetraederschicht zum Vergleich herangezogen. Die Diskussion der geometrischen Rahmenbedingungen der isomorphen Substitution beruht auf der Tatsache, dass ideale unverzerrte Oktaeder- und Tetraederschichten nicht zusammenpassen (**Abb. 8**): Für typische Bindungslängen der 2:1 Schichtsilicate ist die ideale unverzerrte Tetraederschicht meist größer als die ideale unverzerrte Oktaederschicht. Anpassungsmechanismen werden notwendig, da die apikalen Sauerstoffatome der Tetraederschicht auch Teil der Oktaederschicht sind (stellvertretend für die Oktaederschicht sind diejenigen Dreiecksflächen der Oktaeder gezeigt (schwarz, **Abb.8**), die an die Tetraederschicht an kondensiert sind). Als Maß für den strukturellen *mismatch* werden die idealen (a,b) -Ausdehnungen der Tetraederschicht und der Oktaederschicht berechnet (für die jeweilige chemische Zusammensetzung anhand der Ionenradien) und ins Verhältnis $(a,b)_t / (a,b)_o$ gesetzt.

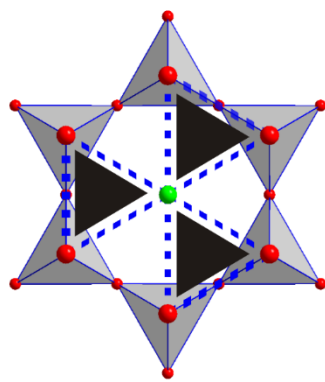


Abb. 8: Schematische Darstellung des strukturellen *mismatch* einer idealen unverzerrten Tetraederschicht, die ihre apikalen Sauerstoffatome mit einer idealen unverzerrten Oktaederschicht teilt. Stellvertretend für die Oktaederschicht sind diejenigen Dreiecksflächen der Oktaeder gezeigt (schwarz), die an die Tetraederschicht an kondensiert sind und im unverzerrten Zustand meist zu klein wären.

Synopsis

Die diskutierten Kristallstrukturen ($1.03 < (a,b)_t / (a,b)_o < 1.15$) suggerieren, dass die Randphase Ferro-Kinoshitalit $\{Ba\} [Fe_3]^{okt} < Si_2Al_2 >^{tet} O_{10}F_2$ mit $(a,b)_t / (a,b)_o = 1.10$ zugänglich sein sollte, was (zumindest durch Schmelzsynthese) nicht der Fall ist. Diese Arbeit schließt sich daher Vorarbeiten an, die geometrische Randbedingungen nicht als hauptsächliches Kriterium für die Zugänglichkeit einer isomorphen Substitution sehen. Dies wird jedoch in einigen Literaturstellen suggeriert.

Die Anpassungsmechanismen der diskutierten Kristallstrukturen (z.B. Abflachung der Oktaeder zur Vergrößerung von deren lateralen Ausdehnung oder Rotation der Tetraeder um die c^* -Achse gegeneinander um die Tetraederschicht zu verkleinern) wurden anhand der Strukturdaten quantifiziert. Die skalaren Beträge für die jeweiligen Anpassungsmechanismen verhalten sich der Größe des Verhältnisses $(a,b)_t / (a,b)_o$ entsprechend, dies wird im Vergleich mit Strukturdaten anderer 2:1 Schichtsilicate deutlich.

Die Leitfähigkeit des synthetisierten Ferro-Kinoshitalites liegt in der Größenordnung $\mu S/cm$ (200°C, unter N₂-Atmosphäre) und steigt für alle Proben um einen Faktor > 2, wenn die Gasatmosphäre oxidierend wird (Luft). Damit geht eine Zunahme des Fe^{III}-Gehaltes auf ca. 13 % durch Oxidation einher. Ein Vergleich mit einem Ferro-Tainiolit ($\{Cs\} [Fe_2Li]^{okt} < Si_2Al_2 >^{tet} O_{10}F_2$) zeigt, dass bei den untersuchten Eisengehalten die Leitfähigkeit stärker von dem Oxidationszustand dominiert wird als von dem Gesamtanteil an strukturellem Eisen. Die Abhängigkeit der Leitfähigkeit von der Oxidationsstufe ist auf die Art des Ladungstransportes (*polaron hopping*) zurückzuführen, hier wirkt Fe^{III} als *hopping-Zentrum*.^[103]

5. Literatur

- [1] Will, G., Kirfel, A., Josten, B., Charge density and chemical bonding in cubic boron nitride. *J. Less Common Met.* **1986**, *117*, 61-71.
- [2] Pease, R., An X-ray study of boron nitride. *Acta Crystallogr.* **1952**, *5*, 356-361.
- [3] Ma, R., Sasaki, T., Two-Dimensional Oxide and Hydroxide Nanosheets: Controllable High-Quality Exfoliation, Molecular Assembly, and Exploration of Functionality. *Acc. Chem. Res.* **2015**, *48*, 136-143.
- [4] Roth, W. J., Gil, B., Makowski, W., Marszalek, B., Eliasova, P., Layer like porous materials with hierarchical structure. *Chem. Soc. Rev.* **2016**, *45*, 3400-3438.
- [5] Bergaya, F., Lagaly, G., General Introduction: Clays, Clay Minerals, and Clay Science. In *Handbook of Clay Science*, Bergaya, F., Theng, D. K. G., Lagaly, G., Eds. Elsevier Ltd.: Amsterdam, 2006, Vol. 1, p 6.
- [6] Dolotko, O., Senyshyn, A., Mühlbauer, M. J., Nikolowski, K., Ehrenberg, H., Understanding structural changes in NMC Li-ion cells by in situ neutron diffraction. *J. Power Sources* **2014**, *255*, 197-203.
- [7] Feicht, P., Breu, J., Gas-phase Preparation of SO₃-Graphite: Host-Exchange and Exfoliation. *Z. Allg. Anorg. Chem.* **2015**, *641*, 1093-1098.
- [8] Mariychuk, R., Baumgartner, A., Wagner, F. E., Lerf, A., Dubbe, A., Moos, R., Breu, J., Synthesis, Structure, and Electric Conductivity of Ferrous Tainiolite and Its Oxidative Conversion into Coarse-Grained Swellable Smectite. *Chem. Mater.* **2007**, *19*, 5377-5387.
- [9] Perdikatsis, B., Burzlaff, H., Strukturverfeinerung am Talk Mg₃[(OH)₂Si₄O₁₀]. *Z. Kristallogr. – Cryst. Mater.* **1981**, *156*, 177.
- [10] Toraya, H., Iwai, S., Marumo, F., Hirao, M., The crystal structure of taeniolite, KLiMg₂Si₄O₁₀F₂. *Z. Krist. – Cryst. Mater.* **1977**, *146*, 73.
- [11] Teppen, B. J., Aggarwal, V., Thermodynamics of Organic Cation Exchange Selectivity in Smectites. *Clays Clay Miner.* **2007**, *55*, 119-130.
- [12] Mermut, A. R., Lagaly, G., Baseline Studies of the Clay Minerals Society Source Clays: Layer-charge Determination and Characteristics of those Minerals Containing 2:1 Layers. *Clays Clay Miner.* **2001**, *49*, 393-397.

- [13] Sasaki, T., Watanabe, M., Hashizume, H., Yamada, H., Nakazawa, H., Macromolecule-like Aspects for a Colloidal Suspension of an Exfoliated Titanate. Pairwise Association of Nanosheets and Dynamic Reassembling Process Initiated from It. *J. Am. Chem. Soc.* **1996**, *118*, 8329-8335.
- [14] Rosenfeldt, S., Stöter, M., Schlenk, M., Martin, T., Albuquerque, R. Q., Förster, S., Breu, J., In-Depth Insights into the Key Steps of Delamination of Charged 2D Nanomaterials. *Langmuir* **2016**, *32*, 10582-10588.
- [15] Stöter, M., Kunz, D. A., Schmidt, M., Hirsemann, D., Kalo, H., Putz, B., Senker, J., Breu, J., Nanoplatelets of Sodium Hectorite Showing Aspect Ratios of ~20 000 and Superior Purity. *Langmuir* **2013**, *29*, 1280-1285.
- [16] Kunz, D. A., Schmid, J., Feicht, P., Erath, J., Fery, A., Breu, J., Clay-Based Nanocomposite Coating for Flexible Optoelectronics Applying Commercial Polymers. *ACS Nano* **2013**, *7*, 4275-4280.
- [17] Strupinski, W., Grodecki, K., Wysmolek, A., Stepniewski, R., Szkopek, T., Gaskell, P. E., Grüneis, A., Haberer, D., Bozek, R., Krupka, J., Baranowski, J. M., Graphene Epitaxy by Chemical Vapor Deposition on SiC. *Nano Lett.* **2011**, *11*, 1786-1791.
- [18] Cai, J., Ruffieux, P., Jaafar, R., Bieri, M., Braun, T., Blankenburg, S., Muoth, M., Seitsonen, A. P., Saleh, M., Feng, X., Müllen, K., Fasel, R., Atomically precise bottom-up fabrication of graphene nanoribbons. *Nature* **2010**, *466*, 470.
- [19] Park, J., Mitchel, W. C., Grazulis, L., Smith, H. E., Eyink, K. G., Boeckl, J. J., Tomich, D. H., Pacley, S. D., Hoelscher, J. E., Epitaxial Graphene Growth by Carbon Molecular Beam Epitaxy (CMBE). *Adv. Mater.* **2010**, *22*, 4140-4145.
- [20] Michot, L. J., Bihannic, I., Maddi, S., Funari, S. S., Baravian, C., Levitz, P., Davidson, P., Liquid-crystalline aqueous clay suspensions. *Proc. Nat. Acad. Sci.* **2006**, *103*, 16101-16104.
- [21] Gabriel, J. C., Camerel, F., Lemaire, B. J., Desvaux, H., Davidson, P., Batail, P., Swollen liquid-crystalline lamellar phase based on extended solid-like sheets. *Nature* **2001**, *413*, 504-508.
- [22] Wan, X., Huang, Y., Chen, Y., Focusing on Energy and Optoelectronic Applications: A Journey for Graphene and Graphene Oxide at Large Scale. *Acc. Chem. Res.* **2012**, *45*, 598-607.
- [23] Gardolinski, J. E. F. C., Lagaly, G., Grafted organic derivatives of kaolinite: II. Intercalation of primary n-alkylamines and delamination. *Clay Miner.* **2005**, *40*, 547.

Literatur

- [24] Bergaya, F., Lagaly, G., General Introduction: Clays, Clay Minerals, and Clay Science. In *Handbook of Clay Science*, Bergaya, F., Theng, D. K. G., Lagaly, G., Eds. Elsevier Ltd.: Amsterdam, 2013, Vol. 2, p 6.
- [25] Gasperin, M., Le Bihan, M. T., Mecanisme d'hydratation des niobates alcalins lamellaires de formule $A_4Nb_4O_{17}$ ($A = K, Rb, Cs$). *J. Solid State Chem.* **1982**, *43*, 346-353.
- [26] Fink, D. H., Thomas, G. W., X-ray Studies of Crystalline Swelling in Montmorillonites. *Soil Sci. Soc. Am. Proc.* **1964**, *28*, 747-750.
- [27] Kalo, H., Milius, W., Breu, J., Single crystal structure refinement of one- and two-layer hydrates of sodium fluorohectorite. *RSC Adv.* **2012**, *2*, 8452-8459.
- [28] Dazas, B., Ferrage, E., Delville, A., Lanson, B., Interlayer structure model of tri-hydrated low-charge smectite by X-ray diffraction and Monte Carlo modeling in the Grand Canonical ensemble. *Am. Mineral.* **2014**, *99*, 1724.
- [29] Martins, M. L., Gates, W. P., Michot, L., Ferrage, E., Marry, V., Bordallo, H. N., Neutron scattering, a powerful tool to study clay minerals. *Appl. Clay Sci.* **2014**, *96*, 22-35.
- [30] Naji, A., Jungblut, S., Moreira, A. G., Netz, R. R., Electrostatic interactions in strongly coupled soft matter. *Physica A* **2005**, *352*, 131-170.
- [31] Pellenq, R. J. M., Caillol, J. M., Delville, A., Electrostatic Attraction between Two Charged Surfaces: A (N,V,T) Monte Carlo Simulation. *J. Phys. Chem. B* **1997**, *101*, 8584-8594.
- [32] Jasmund, K., Lagaly, G., Tonminerale und Tone: Struktur, Eigenschaften, Anwendungen und Einsatz in Industrie und Umwelt. Steinkopff: Darmstadt, **1993**, p. 110.
- [33] Daab, M., Rosenfeldt, S., Kalo, H., Stöter, M., Bojer, B., Siegel, R., Förster, S., Senker, J., Breu, J., Two-Step Delamination of Highly Charged, Vermiculite-like Layered Silicates via Ordered Heterostructures. *Langmuir* **2017**, *33*, 4816-4822.
- [34] Smith, D. W., Ionic hydration enthalpies. *J. Chem. Ed.* **1977**, *54*, 540.
- [35] Mathieson, A. M., Walker, G. F., Crystal Structure of Magnesium-Vermiculite. *Amer. Min.* **1954**, *39*, 231-255.
- [36] Norrish, K., Rausell-Colom, J. A., Low-Angle X-Ray Diffraction Studies of the Swelling of Montmorillonite and Vermiculite. *Clays Clay Miner.* **1961**, *10*, 123-149.

- [37] Salles, F., Bildstein, O., Douillard, J.-M., Jullien, M., Van Damme, H., Determination of the Driving Force for the Hydration of the Swelling Clays from Computation of the Hydration Energy of the Interlayer Cations and the Clay Layer. *J. Phys. Chem. C* **2007**, *111*, 13170-13176.
- [38] Kim, H.-N., Keller, S. W., Mallouk, T. E., Schmitt, J., Decher, G., Characterization of Zirconium Phosphate/Polycation Thin Films Grown by Sequential Adsorption Reactions. *Chem. Mater.* **1997**, *9*, 1414-1421.
- [39] Clearfield, A., Smith, G. D., Crystallography and structure of alpha.-zirconium bis(monohydrogen orthophosphate) monohydrate. *Inorg. Chem.* **1969**, *8*, 431-436.
- [40] Geng, F., Ma, R., Nakamura, A., Akatsuka, K., Ebina, Y., Yamauchi, Y., Miyamoto, N., Tateyama, Y., Sasaki, T., Unusually stable ~100-fold reversible and instantaneous swelling of inorganic layered materials. *Nat. Commun.* **2013**, *4*, 1632.
- [41] Sasaki, T., Kooli, F., Iida, M., Michiue, Y., Takenouchi, S., Yajima, Y., Izumi, F., Chakoumakos, B. C., Watanabe, M., A Mixed Alkali Metal Titanate with the Lepidocrocite-like Layered Structure. Preparation, Crystal Structure, Prototypic Form, and Acid/Base Intercalation Properties. *Chem. Mater.* **1998**, *10*, 4123-4128.
- [42] Song, Y., Iyi, N., Hoshide, T., Ozawa, T. C., Ebina, Y., Ma, R., Yamamoto, S., Miyamoto, N., Sasaki, T., Massive hydration-driven swelling of layered perovskite niobate crystals in aqueous solutions of organo-ammonium bases. *Dalton Trans.* **2018**, *47*, 3022-3028.
- [43] Yamaguchi, D., Miyamoto, N., Koizumi, S., Nakato, T., Hashimoto, T., Hierarchical structure of niobate nanosheets in aqueous solution. *J. Appl. Crystallogr.* **2007**, *40*, 101-105.
- [44] Fukuoka, H., Isami, T., Yamanaka, S., Crystal Structure of a Layered Perovskite Niobate $KCa_2Nb_3O_{10}$. *J. Solid State Chem.* **2000**, *151*, 40-45.
- [45] Walker, G. F., Macroscopic Swelling of Vermiculite Crystals in Water. *Nature* **1960**, *187*, 312-313.
- [46] Omomo, Y., Sasaki, T., Wang, Watanabe, M., Redoxable Nanosheet Crystallites of MnO_2 Derived via Delamination of a Layered Manganese Oxide. *J. Am. Chem. Soc.* **2003**, *125*, 3568-3575.
- [47] Gaillot, A.-C., Lanson, B., Drits, V. A., Structure of Birnessite Obtained from Decomposition of Permanganate under Soft Hydrothermal Conditions. 1. Chemical and Structural Evolution as a Function of Temperature. *Chem. Mater.* **2005**, *17*, 2959-2975.

Literatur

- [48] Steudel, A., Batenburg, L. F., Fischer, H. R., Weidler, P.G., Emmerich, K., Alteration of swelling clay minerals by acid activation. *Appl. Clay. Sci.* **2009**, *44*, 105-115.
- [49] Geng, F., Ma, R., Ebina, Y., Yamauchi, Y., Miyamoto, N., Sasaki, T., Gigantic Swelling of Inorganic Layered Materials: A Bridge to Molecularly Thin Two-Dimensional Nanosheets. *J. Am. Chem. Soc.* **2014**, *136*, 5491-5500.
- [50] McCarney, J., Smalley, M. V., Electron Microscopy Study of n-Butylammonium Vermiculite Swelling. *Clay Miner.* **1995**, *30*, 187-194.
- [51] Swain, M., chemicalize.org. *J. Chem. Inf. Model.* **2012**, *52*, 613-615.
- [52] Garret, W. G., Walker, G. F., Swelling of some vermiculite-organic complexes in water. *Clays Clay Miner.* **1960**, *9*, 557-567.
- [53] Schmidt, C. U., Lagaly, G., Surface modification of bentonites: I. Betaine montmorillonites and their rheological and colloidal properties. *Clay Miner.* **1999**, *34*, 447-458.
- [54] Piffard, Y., Lachgar, A., Tournoux, M., Structure cristalline du phosphatoantimonate $K_3Sb_3P_2O_{14}$. *J. Solid State Chem.* **1985**, *58*, 253-256.
- [55] Langmuir, I., The Role of Attractive and Repulsive Forces in the Formation of Tactoids, Thixotropic Gels, Protein Crystals and Coacervates. *J. Chem Phys.* **1938**, *6*, 873-896.
- [56] Michot, L. J., Paineau, E., Bihannic, I., Maddi, S., Duval, J. F. L., Baravian, C., Davidson, P., Levitz, P., Isotropic/nematic and sol/gel transitions in aqueous suspensions of size selected nontronite NAu1. *Clay Miner.* **2013**, *48*, 663-685.
- [57] Paineau, E., Dozov, I., Bihannic, I., Baravian, C., Krapf, M.-E. M., Philippe, A.-M., Rouzière, S., Michot, L. J., Davidson, P., Tailoring Highly Oriented and Micropatterned Clay/Polymer Nanocomposites by Applying an a.c. Electric Field. *ACS Appl. Mater. Interfaces* **2012**, *4*, 4296-4301.
- [58] Dozov, I., Paineau, E., Davidson, P., Antonova, K., Baravian, C., Bihannic, I., Michot, L. J., Electric-Field-Induced Perfect Anti-Nematic Order in Isotropic Aqueous Suspensions of a Natural Beidellite Clay. *J. Phys. Chem. B* **2011**, *115*, 7751-7765.
- [59] Hemmen, H., Ringdal, N. I., De Azevedo, E. N., Engelsberg, M., Hansen, E. L., Méheust, Y., Fossum, J. O., Knudsen, K. D., The Isotropic–Nematic Interface in Suspensions of Na–Fluorohectorite Synthetic Clay. *Langmuir* **2009**, *25*, 12507-12515.
- [60] Braganza, L. F., Crawford, R. J., Smalley, M. V., Thomas, R. K., Swelling of n-Butylammonium Vermiculite in Water. *Clays Clay Miner.* **1990**, *38*, 90-96.

- [61] Lagaly, G., Ziesmer, S., Colloid chemistry of clay minerals: the coagulation of montmorillonite dispersions. *Adv. Coll. Interface Sci.* **2003**, *100-102*, 105-128.
- [62] Breu, J., Seidl, W., Stoll, A. J., Lange, K. G., Probst, T. U., Charge Homogeneity in Synthetic Fluorohectorite. *Chem. Mater.* **2001**, *13*, 4213-4220.
- [63] Stoll, A., Synthese ladungshomogener Smectite aus der Schmelze zur Einlagerung von Trischelatmetall(II)-Komplexkationen. Universität Bayreuth, **2000**.
- [64] Seidl, W., Hochtemperatursynthese von Smectiten und deren dreidimensional geordnete Einlagerungsverbindungen. Universität Bayreuth, **2004**.
- [65] Möller, M. W., Massgeschneiderte Schichtsilikate für Materialwissenschaftliche Anwendungen. Universität Bayreuth, **2010**.
- [66] Kalo, H., Melt Synthesis, Structural, Characterization and Scaling of Swelling 2:1 Layer Silicate Materials. Universität Bayreuth, **2012**.
- [67] Kunz, D. A., Schichtsilikate als effiziente Bausteine für funktionelle Nanokomposite. Universität Bayreuth, **2013**.
- [68] Stöter, M., Funktionale Nanobausteine mittels kontrollierter Exfolierung von Schichtsilicaten. Universität Bayreuth, **2016**.
- [69] Palin, E. J., Dove, M. T., Hernandez-Laguna, A., Sainz-Diaz, C. I., A computational investigation of the Al/Fe/Mg order-disorder behavior in the dioctahedral sheet of phyllosilicates. *Am. Mineral.* **2004**, *89*, 164-175.
- [70] Kalo, H., Möller, M. W., Kunz, D. A., Breu, J., How to maximize the aspect ratio of clay nanoplatelets. *Nanoscale* **2012**, *4*, 5633-5639.
- [71] Taruta, S., Obara, R., Takusagawa, N., Kitajima, K., Effect of layer charge on chemical and physical properties of synthetic K-fluorine micas. *J. Mater. Sci.* **2005**, *40*, 5597-5602.
- [72] Meunier, A., Why are clay minerals small? *Clay Miner.* **2006**, *41*, 551-566.
- [73] Breu, J., Seidl, W., Stoll, A., Fehlordnung bei Smectiten in Abhängigkeit vom Zwischenschichtkation. *Z. Allg. Anorg. Chem.* **2003**, *629*, 503-515.
- [74] Redhammer, G. J., Beran, A., Dachs, E., Amthauer, G., A Mössbauer and X-ray diffraction study of annites synthesized at different oxygen fugacities and crystal chemical implications. *Phys. Chem. Miner.* **1993**, *20*, 382-394.

Literatur

- [75] Redhammer, G. J., Beran, A., Schneider, J., Amthauer, G., Lottermoser, W., Spectroscopic and structural properties of synthetic micas on the annite-siderophyllite binary: Synthesis, crystal structure refinement, Mössbauer, and infrared spectroscopy. *Am. Mineral.* **2000**, 85, 449-465.
- [76] Redhammer, J. G., Amthauer, G., Lottermoser, W., Bernroider, M., Tippelt, G., Roth, G., X-ray powder diffraction and ^{57}Fe Mossbauer spectroscopy of synthetic trioctahedral micas $\{\text{K}\}[\text{Me}_3]\text{Si}_3\text{T}_1\text{O}_{10}(\text{OH})_2$, $\text{Me} = \text{Ni}^{2+}, \text{Mg}^{2+}, \text{Co}^{2+}, \text{Fe}^{3+}$, $\text{T} = \text{Al}^{3+}, \text{Fe}^{3+}$. *Mineral. Petrol.* **2005**, 85, 89-115.
- [77] Yamada, H., Yoshioka, K., Tamura, K., Fujii, K., Nakazawa, H., Compositional Gap in Dioctahedral-Trioctahedral Smectite System: Beidellite-Saponite Pseudo-binary Join. *Clays Clay Miner.* **1999**, 47, 803-810.
- [78] Herling, M. M., Kalo, H., Seibt, S., Schobert, R., Breu, J., Tailoring the Pore Sizes of Microporous Pillared Interlayered Clays through Layer Charge Reduction. *Langmuir* **2012**, 28, 14713-14719.
- [79] Loewenstein, W., The distribution of aluminum in the tetrahedra of silicates and aluminates. *Am. Mineral.* **1954**, 39, 92-96.
- [80] Tischendorf, G., Förster, H. J., Gottesmann, B., Rieder, M., True and brittle micas: composition and solid-solution series. *Mineral. Mag.* **2007**, 71, 285-320.
- [81] Baumgartner, A., Butterhof, C., Koch, S., Mariychuk, R., Breu, J., Melt Synthesis and Characterization of Synthetic Mn-Rich Tainiolite. *Clays Clay Miner.* **2009**, 57, 271-277.
- [82] Franklin, K. R., Lee, E., Synthesis and ion-exchange properties of Na-4-mica. *J. Mater. Chem. C* **1996**, 6, 109-115.
- [83] Kloprogge, J. T., Komarneni, S., Amonette, J. E., Synthesis of smectite clay minerals: a critical review. *Clays Clay Miner.* **1999**, 47, 529-554.
- [84] Solin, S. A., Mines, D., Haushalter, R., The Synthesis, Structure and Intercalation Properties of Fluormica Clays. *Mol. Cryst. Liq. Cryst. Sci. Tech. A* **1994**, 244, 143-148.
- [85] Vogels, R. J. M. J., Kerkhoffs, M. J. H. V., Geus, J. W., Non-hydrothermal synthesis, characterisation and catalytic properties of saponite clays. In Studies in Surface Science and Catalysis: Preparation of Catalysis VI Scientific Bases for the Preparation of Heterogeneous Catalysts Proceedings of the Sixth International Symposium, Volume 91 ed., Poncelet, G., Ed. Elsevier: **1995**, pp. 1153-1161.

- [86] Hatch, R., HumphreyR.A., Eitel.W., Comerford, J. E., Synthetic mica investigations IX: reviews of progress from 1947 to 1955. U. S. Department of Interior, Bureau of mines, Investigation Report 5337, **1957**.
- [87] Cussler, E. L., Hughes, S. E., Ward III, W. J., Aris, R., Barrier membranes. *J. Membrane Sci.* **1988**, *38*, 161-174.
- [88] Sato, H., Yamagishi, A., Kawamura, K., Molecular Simulation for Flexibility of a Single Clay Layer. *J. Phys. Chem. B* **2001**, *105*, 7990-7997.
- [89] Kunz, D. A., Erath, J., Kluge, D., Thurn, H., Putz, B., Fery, A., Breu, J., In-Plane Modulus of Singular 2:1 Clay Lamellae Applying a Simple Wrinkling Technique. *ACS Appl. Mater. Interfaces* **2013**, *5*, 5851-5855.
- [90] Lewis, J. S., Weaver, M. S., Thin-Film Permeation-Barrier Technology for Organic Light-Emitting Devices. *IEEE J. Sel. Top. Quantum Electron.* **2004**, *10*, 45-57.
- [91] Yanaka, M., Henry, B. M., Roberts, A. P., Grovenor, C. R. M., Briggs, G. A. D., Sutton, A. P., Miyamoto, T., Tsukahara, Y., Takeda, N., Chater, R. J., How cracks in SiO_x-coated polyester films affect gas permeation. *Thin Solid Films* **2001**, *397*, 176-185.
- [92] Kumar, R. S., Auch, M., Ou, E., Ewald, G., Jin, C. S., Low moisture permeation measurement through polymer substrates for organic light emitting devices. *Thin Solid Films* **2002**, *417*, 120-126.
- [93] Tsurko, E. S., Feicht, P., Habel, C., Schilling, T., Daab, M., Rosenfeldt, S., Breu, J., Can high oxygen and water vapor barrier nanocomposite coatings be obtained with a waterborne formulation? *J. Membrane Sci.* **2017**, *540*, 212-218.
- [94] Geim, A. K., Grigorieva, I. V., Van der Waals heterostructures. *Nature* **2013**, *499*, 419-425.
- [95] Li, B.-W., Osada, M., Ozawa, T. C., Ebina, Y., Akatsuka, K., Ma, R., Funakubo, H., Sasaki, T., Engineered Interfaces of Artificial Perovskite Oxide Superlattices via Nanosheet Deposition Process. *ACS Nano* **2010**, *4*, 6673-6680.
- [96] Wang, C., Osada, M., Ebina, Y., Li, B.-W., Akatsuka, K., Fukuda, K., Sugimoto, W., Ma, R., Sasaki, T., All-Nanosheet Ultrathin Capacitors Assembled Layer-by-Layer via Solution-Based Processes. *ACS Nano* **2014**, *8*, 2658-2666.

Literatur

- [97] Bärwinkel, K., Herling, M. M., Rieß, M., Sato, H., Li, L., Avadhut, Y. S., Kemnitzer, T. W., Kalo, H., Senker, J., Matsuda, R., Kitagawa, S., Breu, J., Constant Volume Gate-Opening by Freezing Rotational Dynamics in Microporous Organically Pillared Layered Silicates. *J. Am. Chem. Soc.* **2017**, *139*, 904-909.
- [98] Kunz, D. A., Leitl, M. J., Schade, L., Schmid, J., Bojer, B., Schwarz, U. T., Ozin, G. A., Yersin, H., Breu, J., Quasi-epitaxial Growth of $[\text{Ru}(\text{bpy})_3]^{2+}$ by Confinement in Clay Nano-platelets Yields Polarized Emission. *Small* **2015**, *11*, 792-796.
- [99] Ijdo, W. L., Lee, T., Pinnavaia, T. J., Regularly interstratified layered silicate heterostructures: Precursors to pillared rectorite-like intercalates. *Adv. Mater.* **1996**, *8*, 79-83.
- [100] Möller, M. W., Hirsemann, D., Haarmann, F., Senker, J., Breu, J., Facile Scalable Synthesis of Rectorites. *Chem. Mater.* **2009**, *22*, 186-196.
- [101] Stöter, M., Biersack, B., Reimer, N., Herling, M., Stock, N., Schobert, R., Breu, J., Ordered Heterostructures of Two Strictly Alternating Types of Nanoreactors. *Chem. Mater.* **2014**, *26*, 5412-5419.
- [102] Stöter, M., Biersack, B., Rosenfeldt, S., Leitl, M. J., Kalo, H., Schobert, R., Yersin, H., Ozin, G. A., Förster, S., Breu, J., Encapsulation of Functional Organic Compounds in Nano-glass for Optically Anisotropic Coatings. *Angew. Chem. Int. Ed.* **2015**, *54*, 4963-4967.
- [103] Crine, J. P., Friedmann, A., Wertheimer, M. R., Yelon, A., The relationship between chemical composition and electrical conductivity of some North American micas. *Can. J. Phys.* **1977**, *55*, 270-275.

6. Ergebnisse

6.1. Quantitative Delaminierung geordneter Heterostrukturen

Matthias Daab,[†] Sabine Rosenfeldt,^{‡,§} Hussein Kalo,[§] Matthias Stöter,[†] Beate Bojer,^{||} Renée Siegel,^{||} Stephan Förster[‡], Jürgen Senker^{||} and Josef Breu^{*;†,‡}

Two-Step Delamination of Highly Charged, Vermiculite-like Layered Silicates via Ordered Heterostructures

Veröffentlicht: *Langmuir* 2017, 33, 4816-4822.

Reprinted with permission, Copyright (2017) American Chemical Society.

Impact Factor (2016) Langmuir: 3.833

<http://dx.doi.org/10.1021/acs.langmuir.7b01008>

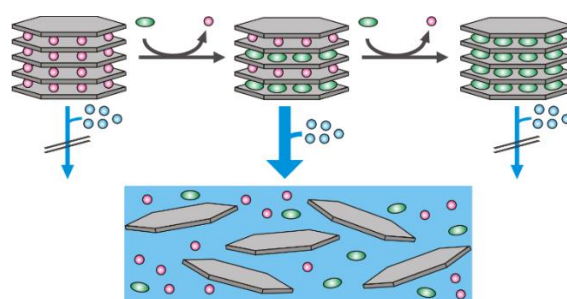
[†]Lehrstuhl für Anorganische Chemie I, Universität Bayreuth, D-95440 Bayreuth, Germany

[‡]Bayerisches Polymerinstitut, D-95440 Bayreuth, Germany

[§]Lehrstuhl für Physikalische Chemie I, Universität Bayreuth, D-95440 Bayreuth, Germany

^{||}BYK Chemie GmbH, D-85368 Moosburg, Germany

^{*}Lehrstuhl für Anorganische Chemie III, Universität Bayreuth, D-95440 Bayreuth, Germany



Darstellung des Eigenanteils:

Das Konzept der Publikation wurde von mir und Prof. Dr. Josef Breu erarbeitet. Das Manuskript wurde von mir geschrieben und wurde mit Prof. Dr. Josef Breu zur Einreichung überarbeitet. Von mir wurden die Auswertungen (Ausnahme SAXS) und deren Interpretation, die Messungen (Ausnahme SAXS und NMR) und alle Experimente durchgeführt. Die Experimente und graphischen Auftragungen habe ich zu einem großen Teil in meiner Masterarbeit durchgeführt. Die Diskussion dieser Heterostruktur im Kontext der Organo-Vermiculite habe ich im ersten Promotionsjahr erarbeitet. Dr. Sabine Rosenfeldt und Prof. Dr. Stephan Förster waren für SAXS-Messungen und für die Auswertung davon verantwortlich. Beate Bojer, Dr. Renée Siegel und Prof. Dr. Jürgen Senker waren für die NMR-Messungen verantwortlich. Dr. Hussein Kalo und Dr. Matthias Stöter trugen zur wissenschaftlichen Diskussion bei. Textauszüge der vorliegenden Publikation habe ich für eine Patentanmeldung vor dem Einreichen des Manuskriptes zur Verfügung gestellt. Mein Eigenanteil beträgt ca. 85 %.

Two-Step Delamination of Highly Charged, Vermiculite-like Layered Silicates via Ordered Heterostructures

Matthias Daab,[†] Sabine Rosenfeldt,^{‡,§} Hussein Kalo,^{||} Matthias Stöter,[†] Beate Bojer,[†] Renée Siegel,[†] Stephan Förster,[§] Jürgen Senker,[†] and Josef Breu^{*†,‡,§,ID}

[†]Lehrstuhl für Anorganische Chemie I, Universität Bayreuth, D-95440 Bayreuth, Germany

[‡]Bayerisches Polymerinstitut, D-95440 Bayreuth, Germany

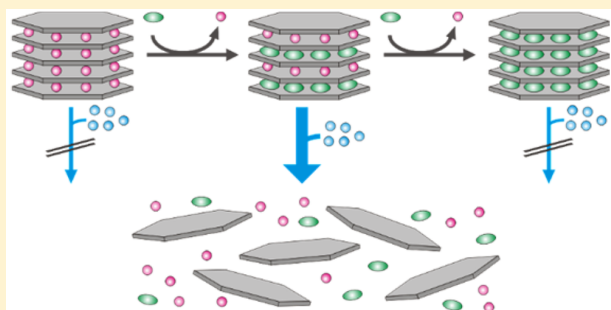
[§]Lehrstuhl für Physikalische Chemie I, Universität Bayreuth, D-95440 Bayreuth, Germany

^{||}BYK Chemie GmbH, D-85368 Moosburg, Germany

^{*}Lehrstuhl für Anorganische Chemie III, Universität Bayreuth, D-95440 Bayreuth, Germany

Supporting Information

ABSTRACT: Because of strong Coulomb interactions, the delamination of charged layered materials becomes progressively more difficult with increasing charge density. For instance, highly charged sodium fluorohectorite ($\text{Na}_{0.6}\text{Mg}_{2.4}\text{Li}_{0.6}\text{Si}_4\text{O}_{10}\text{F}_2$, Na-Hec) cannot be delaminated directly by osmotic swelling in water because its layer charge exceeds the established limit for osmotic swelling of 0.55 per formula unit $\text{Si}_4\text{O}_{10}\text{F}_2$. Quite surprisingly, we found that this hectorite at the border of the smectite and vermiculite group can, however, be utterly delaminated into 1-nm-thick platelets with a high aspect ratio (24 000) in a two-step process. The hectorite is first converted by partial ion exchange into a one-dimensionally ordered, interstratified heterostructure with strictly alternating Na^+ and *n*-butylammonium (C4) interlayers. This heterostructure then spontaneously delaminates into uniform single layers upon immersion in water whereas neither of the homoionic phases (Na-Hec and C4-Hec) swells osmotically. The delamination of more highly charged synthetic layered silicates is a key step to push the aspect ratio beyond the current limits.



INTRODUCTION

The utter delamination of bulk layered materials into nanosheets of unimodal thickness can be regarded as the key challenge for two-dimensional (2D) materials. The combination of different nanosheets into heterostructures^{1–3} and the formation of ordered nanocomposites^{4,5} requires sheets of uniform thickness. This is a challenge for charge-neutral layered materials such as graphite,^{6,7} boron nitride,⁸ black phosphorus,⁹ and metal dichalcogenides^{10,11} where delamination mostly relies on shearing forces. The conversion of such compounds by redox chemistry into charged layered salts that can be stabilized in suitable polar aprotic solvents¹² was recently suggested as a smart workaround. Layered titanates,^{13–15} layered antimonyphosphates,¹⁶ and layered silicates^{17–20} are redox-inert anionic layered materials that have been shown to spontaneously delaminate by rapid osmotic swelling when immersed in water. This repulsive delamination represents the most gentle route,^{21–23} allowing for separation into nanosheets that inherit the lateral diameter of the parent material and thus yield a maximum aspect ratio α (ratio of lateral dimensions and height). The aspect ratio is of particular importance if the nanosheets are applied as barrier pigments because the gas permeability of nanocomposites decreases to α^2 .^{24–28}

The melt synthesis of layered silicates (hectorite, $\text{Na}_{0.5}\text{Mg}_{2.5}\text{Li}_{0.5}\text{Si}_4\text{O}_{10}\text{F}_2$) gave access to nanosheets with mean $\alpha = 18\,000$ via osmotic swelling.²¹ Flexible, 1.5- μm -thick polyurethane-based barrier films made with this filler material allowed for a reduction of the oxygen transmission rate by 6 orders of magnitude.²⁹ For the most challenging packaging of organic light-emitting diodes, even larger aspect ratios are required without sacrificing optical transparency.²⁸

The preferred mechanism for delamination, osmotic swelling, however, is dependent on the layer charge of the layered silicate and the charge and hydration enthalpy of interlayer ions. On one side, osmotic swelling for Na-hectorites is observed only if the layer charge does not exceed 0.55 per formula unit $\text{Si}_4\text{O}_{10}\text{F}_2$ (p.f.u.).³⁰ On the other side, the lateral dimension of layered silicates increases with the layer charge.^{31–33} It would therefore be highly desirable to extend the regime of osmotic swelling to higher layer charges and thus gain access to even larger aspect ratios.

Received: March 27, 2017

Revised: April 27, 2017

Published: April 28, 2017

For some highly charged Na-vermiculites ($0.6 < x < 0.9$) after cation exchange with amino acids^{34,35} or *n*-butylammonium (C4),^{18,19,36–38} macroscopic swelling or gel formation was reported. Uniform swelling, however, requires a very time-consuming (typically >1 year) conversion of the pristine, natural vermiculite into its homoionic Na form. Moreover, these materials are typically ochre-colored, rendering them useless for optoelectronic packaging.

We were able to overcome the layer charge limit of 0.55 p.f.u. for the osmotic swelling of Na-hectorites via a two-step process. $\text{Na}_{0.6}\text{Mg}_{2.4}\text{Li}_{0.6}\text{Si}_4\text{O}_{10}\text{F}_2$ (Na-Hec) is converted by partial ion exchange into a one-dimensionally (1D)-ordered, regularly interstratified heterostructure with strictly alternating Na^+ and *n*-butylammonium (C4) interlayers. This heterostructure spontaneously delaminates uniformly into single layers upon immersion in water whereas neither of the homoionic phases (Na-Hec, C4-Hec) swells osmotically. The delamination of more highly charged synthetic layered silicates is a key step to push the aspect ratio beyond current limits.

EXPERIMENTAL SECTION

Synthesis and Characterization of Na-Hec. A highly charged Na-fluorohectorite $\text{Na}_{0.6}\text{Mg}_{2.4}\text{Li}_{0.6}\text{Si}_4\text{O}_{10}\text{F}_2$ (Na-Hec) was prepared by melt synthesis according to a published procedure,⁴² followed by annealing (6 weeks, 1050 °C) to improve charge homogeneity.²¹ These steps were carried out in gastight molybdenum crucibles. Educts NaF (99.995%, Alfa Aesar), LiF (>99.9%, ChemPur), MgF2 (>99.9%, ChemPur), MgO (99.95%, Alfa Aesar), and SiO₂ (Merck, fine granular quartz, purum) are mixed according to the nominal composition. The crucible was ramped to 1750 °C (15 °C/min), held at this temperature for 70 min, and cooled to 1300 °C (55 °C/min) and then to 1050 °C (10 °C/min). Finally, it was quenched by switching off the power. The obtained Na-Hec was washed with deionized water until a conductivity of $<10 \mu\text{S}/\text{cm}$ was reached. The cation exchange capacity (CEC) was measured by the [Cu(trien)] method^{43,44} and the layer charge density was determined according to Lagaly.^{45,46}

Powder X-ray Diffraction. Powder X-ray diffraction (PXRD) patterns were recorded on a STOE Stadi P powder diffractometer using Cu K α_1 radiation. To minimize texture, the samples were placed in a glass capillary. Prior to measurement, samples were heated to 150 °C for 12 h (dry sample) followed by equilibration for 24 h over saturated K₂CO₃ (43% relative humidity (r.h.) sample) or K₂SO₄ solution (98% r.h. sample). After equilibration, the capillaries were sealed. Textured samples were measured in Bragg–Brentano geometry on a PANalytical Xpert Pro equipped with an X’Celerator Scientific RTMS detector (Cu K α radiation). PXRD patterns at fixed relative humidities were recorded in a temperature–humidity chamber (Anton Paar temperature humidity chamber driven by a VTI corp. RH-200 humidity generator) mounted on the PANalytical Xpert Pro.

MAS NMR Measurements. ¹⁹F MAS spectra were recorded on a Bruker Avance III spectrometer (600 MHz) in a 1.3 mm HX MAS rotor, with the MAS frequency being 62.5 kHz. The spectrum was obtained using a 90° pulse (1.2 μs , four scans). A relaxation time of 900 s was used, and longer relaxation showed no changes in relative peak intensities, justifying the chosen relaxation time.

Partial Ion Exchange of Na-Hec. The partial exchange was carried out at room temperature in an ethanol/water mixture (1:1). Typically, 20 mg of Na-Hec was weighed into glass vessels with screw caps, and aliquots of a 0.05 M aqueous solution of *n*-butylammonium formate were added that correspond to 15 to 150% of the CEC of Na-Hec. The suspensions were adjusted to a final concentration of 3.5 mmol/L of *n*-butylammonium formate and were placed in an overhead shaker for 24 h. After exchange, samples were washed three times in ethanol/water and one time in ethanol.

Complete Ion Exchange of Na-Hec. Na-Hec (100 mg) was suspended in 2 mL water and treated five times for 24 h with a 100-fold excess of the CEC of *n*-butylammonium formate (2 M) in order

to ensure complete ion exchange. The product was washed three times with water and one time with ethanol.

CHN Analysis. A PerkinElmer 2400 CHN equipped with a combustion tube filled with tungsten(VI) oxide granules was used at a combustion temperature of 1050 °C. Samples were dried at 110 °C for 48 h and stored in a glovebox prior to measurement.

Small-Angle X-ray Scattering (SAXS). SAXS data were measured using a Double Ganesha AIR system (SAXSLAB, Denmark). The X-ray source of this laboratory-based system is a rotating anode (copper, MicroMax 007HF, Rigaku Corporation, Japan) providing a microfocused beam. The data are recorded by a position-sensitive detector (Pilatus 300 K, Dectris). The measurements on the suspensions were made in 1 mm glass capillaries and analyzed as described previously.⁴⁷ For suspensions that sediment (Na-Hec, C4-Hec), the position of the capillary was adjusted to ensure the sediment to be in the SAXS’s beam focus. Control measurements in the supernatant yield the scattering pattern of water.

Particle Size. The particle size distribution was determined by static light scattering (SLS) according to ISO 13320 (Retsch LA-950, Horiba) in a flow cell using a measurement routine called mica in water (with a refractive index of 1.5 for the solid phase). When measured in a dilute suspension (0.005 wt %), SLS gives a good approximation of the radius of gyration, which may be attributed to the radius of the platelets. Particle size distributions as determined by SLS correspond well to particle diameters derived from other methods⁴⁸ such as scanning electron microscopy (SEM, Figure S1).

Atomic Force Microscopy (AFM). AFM was done in tapping mode using a Dimension 3100 NanoScope IV unit equipped with OTESPA-R3 (Bruker) silicon tips. Samples were prepared by dropping a very dilute aqueous dispersion (5 mg/L) in Millipore water onto silicon wafers.

RESULTS AND DISCUSSION

Synthesis and Characterization of Na-Hec. Powder X-ray diffraction (PXRD) proves a single-phase material (Figure 1a). As indicated by the appearance of distinct diffraction peaks in the 2 θ range of the 02/11 band, for all hydration levels $\text{Na}_{0.6-x}\text{Hec}$ shows a very low degree of stacking faults as compared to $\text{Na}_{0.5}\text{-Hec}$.²¹

The nonhydrated (0 water layer, 0 WL) material shows a basal spacing (d_{00l}) of 9.7 Å. Upon exposure to moist air, stepwise hydration to 1 WL (43% r.h., $d_{00l} = 12.3$ Å) and to 2 WL (98% r.h., $d_{00l} = 15.4$ Å) is observed. The 00l series is sharp and rational, indicating a homogeneous intracrystalline reactivity leading to the same hydration level and therefore interlayer spaces of uniform height. Indexing of the 2 WL phase was straightforward ($C2/m$, $a = 5.245$ Å, $b = 9.077$ Å, $c = 15.217$ Å, $\beta = 96.591^\circ$), and all peaks can be assigned to this cell.

Mg/Mg/Mg and Mg/Mg/Li moieties surrounding the structural F nuclei give rise to two clearly separated bands in the ¹⁹F NMR spectra,⁴⁹ and their ratio can therefore be used to determine the Mg/Li ratio in the octahedral layer⁵⁰ to be $[\text{Mg}_{2.40}\text{Li}_{0.60}]^{oct}$ (Figure S2). The CEC was 152 mval/100 g, which again is in good agreement with the CEC expected for a layer charge of 0.6 p.f.u. (155 mval/100g). The charge density was evaluated according to Lagaly.⁴⁶ Herein, interlayer Na^+ is completely exchanged with *n*-alkylammonium ($\text{C}_n\text{H}_{2n+1}\text{NH}_3^+$, Figure 1b), for which the equivalent area per charge is known for a dense packing. For short chains, charge neutrality can be realized with monolayers as for *n*-butylammonium ($n = 4$, $d_{00l} = 13.1$ Å). A dense packing of this chain length has a charge density corresponding to a layer charge of 0.65 p.f.u.. Increasing the chain length to $n = 5$ broadens and shifts the d_{00l} peak to higher d spacings. This indicates that with this larger equivalent area charge neutrality can no longer be achieved with only

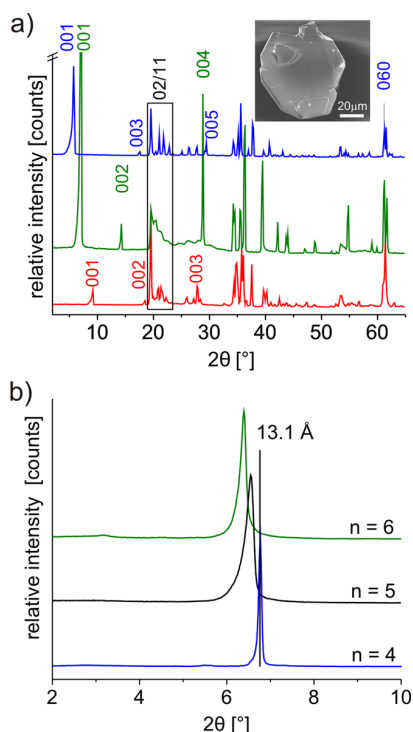


Figure 1. (a) PXRD patterns of dried Na-Hec (OWL, red) and Na-Hec at 43% r.h. (1 WL, green) and at 98% r.h. (2 WL, blue), along with a typical SEM image of Na-Hec. (b) PXRD patterns of textured Na-Hec completely exchanged with *n*-alkylammonium ions of different chain length ranging from *n*-butylammonium (*n* = 4) to *n*-hexylammonium (*n* = 6). By this means, the layer charge was determined according to Lagaly.

monolayers but some bilayers need to be mixed in. Monolayers of *n* = 5 would correspond to a layer charge of 0.56 p.f.u.. Consequently, the charge density as determined with the Lagaly method can be narrowed down to 0.56 < *x* < 0.65 p.f.u.. In summary, the ¹⁹F NMR spectra, CEC, and charge density all agree within experimental errors with a composition of [Na_{0.60}]_{inter}[Mg_{2.40}Li_{0.60}]^{oct}Si₄O₁₀F₂, indicating that no amorphous material is present.

Synthesis of the 1D-Ordered Heterostructure. With charge homogeneous layered silicates, upon partial ion exchange, incoming organocations will segregate into distinct interlayers. Moreover, this will inevitably lead to the formation of 1D-ordered interstratifications of two strictly alternating (Reichweite 1⁵¹) types of interlayer cations.⁵² The two types of interlayers in such heterostructures will, however, have different charge densities. Therefore, besides the desire to build a 1D heterostructure, equal probability (*w*₁ = *w*₂) of the two types is obligatory and requires the identification of the required degree of ion exchange to meet this criterion. Because the partition equilibrium is dependent on the degree of exchange, the conditions⁵² (e.g., solubility and concentration of incoming cation, solvent and temperature) for *w*₁ = *w*₂ have to be determined empirically in an iterative way. The solubility of *n*-butylammonium in ethanol/water (1:1) is high; consequently, the preference of this cation to be intercalated is low, with typically 60:40 partitioning (Table S1, Figure S3). For instance, upon addition of 15% CEC only 9% of Na cations are exchanged. Nevertheless, even at this low degree of exchange, the preference for Reichweite 1 becomes obvious by a weak and

broad superstructure reflection representing the 1D heterostructure. To fix the swelling, all PXRDs were recorded at 43% r.h. (Figure 2a) where the Na interlayers adopt the 1 WL

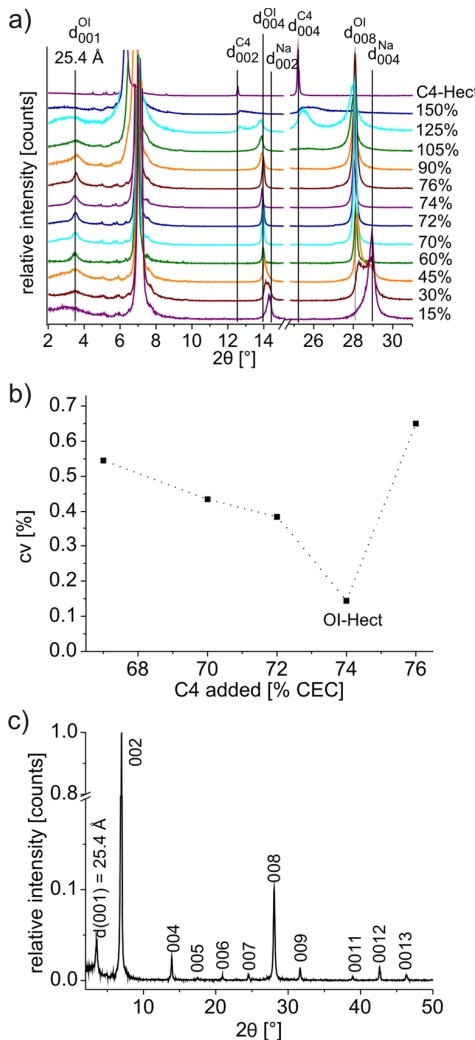


Figure 2. (a) PXRD patterns of textured samples at 43% r.h. for Na-Hec partially exchanged with C4 (15 to 150% of CEC added) and for the completely exchanged C4-HeC phase. Furthermore, the *d* spacings of the homoionic phases (Na- and C4-HeC) are shown by straight lines. (b) Coefficient of variation (cv) of the 00*l* series of partially exchanged phases. The most ordered interstratified phase, OI-HeC, is obtained upon addition of 74% CEC. (c) PXRD pattern of textured OI-HeC.

hydration with *d* = 12.3 Å. With the superstructure reflex being observed at 25.4 Å, the C4 interlayers correspond to a *d* spacing of 13.1 Å, which is characteristic of nonhydrated *n*-butylammonium monolayers (Figure 1b).

With progressive ion exchange, the basal reflections of the superstructure become more intense, narrower, and more rational as indicated by the coefficient of variation (cv). The cv represents the standard deviation of the mean *d* spacing as calculated from the 00*l* series. The smaller the cv, the more regular the *d* spacing in a stack, indicating that the 00*l* series obeys Bragg's law and integer (rational) *l* values are derived from diffraction peaks. A larger cv indicates that wrong *d*

spacings are built into the stack in a random-type interstratification.⁵³ The minimum in the *cv* was found when *n*-butylammonium corresponding to 74% of the CEC was added (*cv* = 0.14%, Figure 2b,c and Table S2). According to Bailey, a *cv* of <0.75% indicates well-ordered regularly interstratified compounds.⁵⁴ A *cv* of 0.14% therefore suggests that both criteria, Reichweite 1 and $w_{\text{Na}} = w_{\text{C}4}$, are met at this point. The quality of the ordering is, moreover, reflected by clearly visible higher-order reflections of the basal series (e.g., 0013). This phase will be referred to as OI-Hec. The partition equilibrium at this point was determined by CHN analysis, which reveals the composition of OI-Hec to be $[\text{Na}_{0.33}\text{C}4_{0.27}]_{\text{inter}}$ (Table S1). This composition would suggest that the Na interlayers have a higher charge density as compared to C4 interlayers. It can, however, not be ruled out that some of the Na^+ cations were trapped in the C4 interlayers as previously reported for rectorite-type interstratifications.⁵⁵

OI-Hec represents a thermodynamically preferred state.⁵² Including additional C4 interlayers beyond $w_{\text{Na}} = w_{\text{C}4}$ requires progressive *n*-butylammonium concentrations because the partition equilibrium is shifted in favor of the solution phase (Figure S3). Complete ion exchange (Table S1) requires an *n*-butylammonium concentration exceeding 200% CEC. For homoionic C4-Hec at 43% r.h., a basal spacing of $d_{001} = 14.0 \text{ \AA}$ is observed, which is significantly higher than the monolayer of *n*-butylammonium (13.1 \AA). Moreover, the basal spacing changes with the r.h. (Figure S4), indicating that homoionic C4-Hec is also capable of limited swelling.

Osmotic Swelling. When adding increasing amounts of water to melt-synthesized lower-charged $\text{Na}_{0.5}\text{Mg}_{2.5}\text{Li}_{0.5}\text{Si}_4\text{O}_{10}\text{F}_2$, adjacent silicate layers become progressively separated by water via repulsive osmotic swelling.⁵⁶ With small-angle X-ray scattering (SAXS), a basal series is observed, indicating a uniform separation (>100 \AA). In line with the charge limit suggested for osmotic swelling by Lagaly (0.55 p.f.u.),³⁰ that for $\text{Na}_{0.6}\text{Mg}_{2.4}\text{Li}_{0.6}\text{Si}_4\text{O}_{10}\text{F}_2$ (Na-Hec) swelling in water is limited to 15.1 \AA , corresponding to the 2WL hydrate. Similarly, the swelling of the other homoionic compound, C4-Hec, is limited to 14.7 \AA when being immersed in water. The very weak extra signals observed for the homoionic phases represent traces of more highly swollen interlayers. These materials do not form gels, and both homoionic phases sediment quickly within less than a minute if suspended in water (10 wt %, Figure 3). Contrary to the end members, OI-Hec swells osmotically in water and instantly and spontaneously forms a gel-like dispersion upon addition of 90 wt % water that is stable over months. As indicated by the absence of peaks $>q = 0.25 \text{ \AA}^{-1}$ (Figure 3), this gel does not contain any multistacks but all adjacent layers are separated to the same large distance. Most people would refer to the delaminated state as an isotropic suspension of freely rotating individual layers. For such large-diameter platelets as here, this isotropic state can, however, be realized only at very low solid contents (e.g., <0.005 wt %), allowing the separation of adjacent layers to distances larger than their diameter. A principal problem with attributing delamination to the isotropic phase is that delamination then is determined not only by the lack of cohesion of adjacent layers but also by their diameter. Smaller platelets will be allowed to freely rotate at lower dilutions as compared to large platelets. We therefore refer to delaminated materials whenever repulsive osmotic swelling is observed that separates adjacent layers to distances that can be controlled by stoichiometry (solid content of gels, Figure 3). At

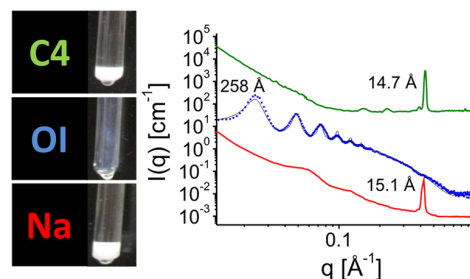


Figure 3. (Left) Aqueous suspensions of Na-Hec, OI-Hec, and C4-Hec in water. The homoionic phases will sediment in water within less than a minute, whereas OI-Hec forms a transparent gel-like dispersion that is stable over months. (Right) SAXS measurements of aqueous suspensions in which only the 1D-ordered heterostructure (blue) reveals osmotic swelling to a d spacing up to 258 \AA . A y offset for the homoionic phases (Na, red; C4, green) has been applied to avoid overlap.

10 wt %, adjacent silicate layers of OI-Hec are uniformly separated to a d spacing of 258 \AA (248 \AA interlayer volume + 10 \AA silicate layer). Assuming a density of 1 g cm^{-3} for the aqueous interlayer volume and 2.7 g cm^{-3} for the silicate layer, respectively, for a uniformly swollen gel of 10 wt % a separation of 243 \AA can be calculated, which is in fair agreement with observations (details in the Supporting Information). This would suggest that upon osmotic swelling of the 1D heterostructure a gel is obtained that is formed by widely separated singular silicate layers.

Further evidence for the formation of single layers of 1 nm thickness is provided by AFM measurements. For this, highly diluted dispersions (0.0005 wt %) were suspended on Si wafers and dried. Because the height of a silicate layer is about 1 nm,^{21,57} all nanosheets of less than 2 nm height can be attributed to single layers. Observed heights, however, are expected to be somewhat larger than 1 nm because of the adsorption of hydrated ions. Only nanosheets of 1.4 nm height were identified with AFM (Figure 4a,c). At spots with higher concentrations, bandlike structures are formed upon drying, again with discrete steps of ~1.4 nm in the height profiles (Figure 4b,d).

The particle size distribution as determined by SLS is in good agreement with the lateral dimensions of the silicate layers.²¹ For OI-Hec, a number-weighted mean particle size of 24 μm

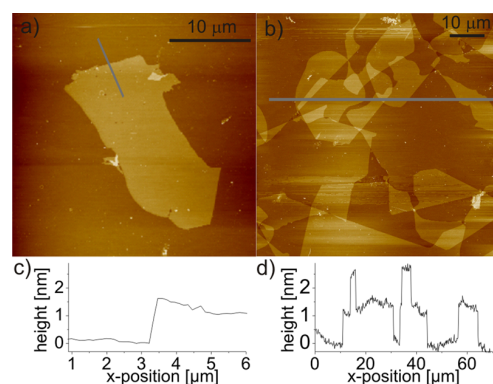


Figure 4. Atomic force microscopy of OI-Hec. A single layer (a) and several layers that have been restacked randomly upon drying are shown (b), along with their height profiles (c, d).

was observed (Figure S5). As expected, because of the higher layer charge, this value is higher (33%) than the mean particle size of $\text{Na}_{0.5}\text{Mg}_{2.5}\text{Li}_{0.5}\text{Si}_4\text{O}_{10}\text{F}_2$ ($18 \mu\text{m}$).

Why Does OI-Hec Delaminate While the Homoionic End Members Do Not Swell Osmotically? We have previously observed that 1D-ordered heterostructures of Na^+ interlayers and nonswelling interlayers of NH_4^{+22} or hydrophobic dyes⁴⁷ delaminate into double stacks by osmotic swelling being restricted to the Na^+ interlayers. Moreover, the segregation of the two types of interlayer cations will be accompanied by a differentiation of the charge densities of interlayers, which may differ by as much as about 20% in the different interlayer types.^{52,53} The onset of osmotic swelling is determined by a subtle balance of electrostatic interactions between interlayer cations and silicate layers and among interlayer cations versus their hydration enthalpy and translational entropy.⁵⁶ Consequently, the swelling behavior of heterostructures is actually expected to be significantly different from that of the homoionic materials. Although we believe that the different swelling behavior has thermodynamic origins, the kinetic hindrance of swelling of homoionic phases cannot be ruled out experimentally.

We propose double stacks of an *n*-butylammonium interlayer being sandwiched between two silicate layers as a transient intermediate (Figure 5). The hydration enthalpy of

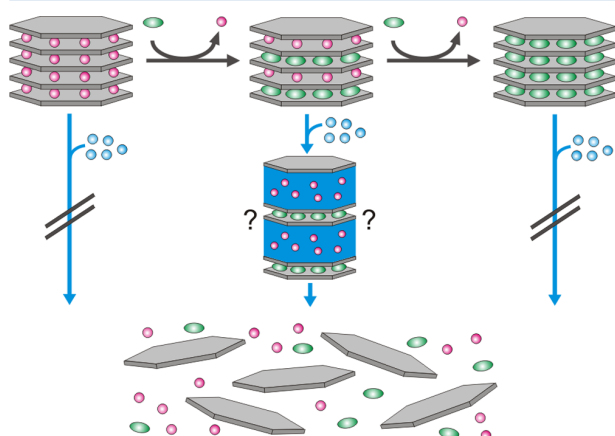


Figure 5. Sketch of the synthesis and swelling behavior of OI-Hec. Na^+ (red) is partially exchanged with C4 (green), and obtained OI-Hec disintegrates into single nanosheets upon immersion in water. The proposed transient intermediate state of double stacks is shown. Such swelling behavior is not observed for end members Na-Hec and C4-Hec.

the Na^+ interlayers is expected to be higher than that of the C4 interlayers. Once the Na^+ interlayer cations are released into the diffuse double layer of the double stacks, they will compete with *n*-butylammonium for the remaining interlayer sites, imparting to them more swelling and eventually leading to complete delamination into singular silicate layers. The swelling behavior of C4 interlayers in OI-Hec and C4-Hec in any case differs significantly from that of corresponding vermiculite compounds described previously. Completely ion exchanged *n*-butylammonium vermiculites spontaneously form gels^{18,19,36–41} when immersed in deionized water. Contrary to this, for C4-Hec swelling is restricted to 14.7 \AA even when immersed in water (Figure 3). Along the same lines, at 95% r.h. the *n*-butylammonium form of Eucatex vermiculite swells to about 20

\AA (Figure S6), a value considerably higher than the 14.7 \AA observed for C4-Hec. Counterintuitively and despite its higher layer charge, it seems that the intracrystalline reactivity of *n*-butylammonium vermiculites is higher than that of C4-Hec.

CONCLUSIONS

Whereas neither homoionic Na-Hec nor C4-Hec end members show osmotic swelling, the 1D-ordered heterostructure of the two readily delaminates when immersed in water. We propose a mechanism involving transient double stacks. This gentle top-down procedure delivers delaminated nanosheets with a very high aspect ratio (24 000) without the need to apply any shearing force. Although the layer charge of Na-Hec nominally is at the lower range of vermiculites, surprisingly the swelling behavior of the two is distinctly different. The reason for this difference will be addressed in future work.

ASSOCIATED CONTENT

Supporting Information

The Supporting Information is available free of charge on the ACS Publications website at DOI: 10.1021/acs.langmuir.7b01008.

SEM image; ^{19}F -NMR and corresponding calculations; CHN analysis and distribution equilibrium; PXRD of partial ion exchange; humidity-dependent *d* spacings of Na-, OI-, and C4-Hec; static light scattering; PXRD of C4-vermiculite at 95% r.h.; and calculations concerning the *d* spacing of a gel (PDF)

AUTHOR INFORMATION

Corresponding Author

*Phone +49 921 55 2531. Fax: +49 921 55 2788. E-mail: Josef.Breu@uni-bayreuth.de.

ORCID

Josef Breu: 0000-0002-2547-3950

Funding

This work was supported by the Deutsche Forschungsgemeinschaft (SFB 840) and by the BYK Chemie GmbH. M.D. thanks the Fonds der Chemischen Industrie for a fellowship.

Notes

The authors declare no competing financial interest.

ACKNOWLEDGMENTS

Prof. A. Fery and Prof. G. Papastavrou are acknowledged for making AFM equipment available.

REFERENCES

- (1) Geim, A. K.; Grigorieva, I. V. Van der Waals heterostructures. *Nature* 2013, 499, 419–425.
- (2) Jariwala, D.; Marks, T. J.; Hersam, M. C. Mixed-dimensional van der Waals heterostructures. *Nat. Mater.* 2017, 16, 170–181.
- (3) Lotsch, B. V. Vertical 2D Heterostructures. *Annu. Rev. Mater. Res.* 2015, 45, 85–109.
- (4) Doblhofer, E.; Schmid, J.; Rieß, M.; Daab, M.; Suntlinger, M.; Habel, C.; Bargel, H.; Hugenschmidt, C.; Rosenfeldt, S.; Breu, J.; Scheibel, T. Structural Insights into Water-Based Spider Silk Protein–Nanoclay Composites with Excellent Gas and Water Vapor Barrier Properties. *ACS Appl. Mater. Interfaces* 2016, 8, 25535–25543.
- (5) Wong, M.; Ishige, R.; White, K. L.; Li, P.; Kim, D.; Krishnamoorti, R.; Gunther, R.; Higuchi, T.; Jinnai, H.; Takahara, A.; Nishimura, R.; Sue, H. J. Large-scale self-assembled zirconium

- phosphate smectic layers via a simple spray-coating process. *Nat. Commun.* **2014**, *5*, 3589.
- (6) Novoselov, K. S.; Geim, A. K.; Morozov, S. V.; Jiang, D.; Zhang, Y.; Dubonos, S. V.; Grigorieva, I. V.; Firsov, A. A. Electric Field Effect in Atomically Thin Carbon Films. *Science* **2004**, *306*, 666.
- (7) Meyer, J. C.; Geim, A. K.; Katsnelson, M. I.; Novoselov, K. S.; Booth, T. J.; Roth, S. The structure of suspended graphene sheets. *Nature* **2007**, *446*, 60–63.
- (8) Jiang, X. F.; Weng, Q.; Wang, X. B.; Li, X.; Zhang, J.; Golberg, D.; Bando, Y. Recent Progress on Fabrications and Applications of Boron Nitride Nanomaterials: A Review. *J. Mater. Sci. Technol.* **2015**, *31*, 589–598.
- (9) Bridgman, P. W. Two new modifications of phosphorous. *J. Am. Chem. Soc.* **1914**, *36*, 1344–1363.
- (10) Zhou, M.; Lou, X. W.; Xie, Y. Two-dimensional nanosheets for photoelectrochemical water splitting: Possibilities and opportunities. *Nano Today* **2013**, *8*, 598–618.
- (11) Yin, Z.; Li, H.; Li, H.; Jiang, L.; Shi, Y.; Sun, Y.; Lu, G.; Zhang, Q.; Chen, X.; Zhang, H. Single-Layer MoS₂ Phototransistors. *ACS Nano* **2012**, *6*, 74–80.
- (12) Cullen, P. L.; Cox, K. M.; Bin Subhan, M. K.; Picco, L.; Payton, O. D.; Buckley, D. J.; Miller, T. S.; Hodge, S. A.; Skipper, N. T.; Tileli, V.; Howard, C. A. Ionic solutions of two-dimensional materials. *Nat. Chem.* **2017**, *9*, 244–249.
- (13) Geng, F.; Ma, R.; Nakamura, A.; Akatsuka, K.; Ebina, Y.; Yamauchi, Y.; Miyamoto, N.; Tateyama, Y.; Sasaki, T. Unusually stable ~100-fold reversible and instantaneous swelling of inorganic layered materials. *Nat. Commun.* **2013**, *4*, 1632.
- (14) Maluangnont, T.; Matsuba, K.; Geng, F.; Ma, R.; Yamauchi, Y.; Sasaki, T. Osmotic Swelling of Layered Compounds as a Route to Producing High-Quality Two-Dimensional Materials. A Comparative Study of Tetramethylammonium versus Tetrabutylammonium Cation in a Lepidocrocite-type Titanate. *Chem. Mater.* **2013**, *25*, 3137–3146.
- (15) Sasaki, T.; Watanabe, M. Osmotic Swelling to Exfoliation. Exceptionally High Degrees of Hydration of a Layered Titanate. *J. Am. Chem. Soc.* **1998**, *120*, 4682–4689.
- (16) Gabriel, J. C.; Camerel, F.; Lemaire, B. J.; Desvaux, H.; Davidson, P.; Batail, P. Swollen liquid-crystalline lamellar phase based on extended solid-like sheets. *Nature* **2001**, *413*, 504–508.
- (17) Schmidt, C. U.; Lagaly, G. Surface modification of bentonites: I. Betaine montmorillonites and their rheological and colloidal properties. *Clay Miner.* **1999**, *34*, 447–458.
- (18) Garret, W. G.; Walker, G. F. Swelling of some vermiculite-organic complexes in water. *Clays Clay Miner.* **1962**, *9*, 557–567.
- (19) Smalley, M. V. The ion distribution in n-butylammonium vermiculite gels. *Mol. Phys.* **1992**, *76*, 1501–1502.
- (20) Meleshyn, A.; Bunnenberg, C. The gap between crystalline and osmotic swelling of Na-montmorillonite: A Monte Carlo study. *J. Chem. Phys.* **2005**, *122*, 034705.
- (21) Stöter, M.; Kunz, D. A.; Schmidt, M.; Hirsemann, D.; Kalo, H.; Putz, B.; Senker, J.; Breu, J. Nanoplatelets of Sodium Hectorite Showing Aspect Ratios of 20 000 and Superior Purity. *Langmuir* **2013**, *29*, 1280–1285.
- (22) Stöter, M.; Gödrich, S.; Feicht, P.; Rosenfeldt, S.; Thurn, H.; Neubauer, J. W.; Seuss, M.; Lindner, P.; Kalo, H.; Möller, M.; Fery, A.; Förster, S.; Papastavrou, G.; Breu, J. Controlled Exfoliation of Layered Silicate Heterostructures into Bilayers and Their Conversion into Giant Janus Platelets. *Angew. Chem., Int. Ed.* **2016**, *55*, 7398–7402.
- (23) Stöter, M.; Rosenfeldt, S.; Breu, J. Tunable Exfoliation of Synthetic Clays. *Annu. Rev. Mater. Res.* **2015**, *45*, 129–151.
- (24) Cussler, E. L.; Hughes, S. E.; Ward, W. J., III; Aris, R. Barrier membranes. *J. Membr. Sci.* **1988**, *38*, 161–174.
- (25) Priolo, M. A.; Holder, K. M.; Greenlee, S. M.; Grunlan, J. C. Transparency, Gas Barrier, and Moisture Resistance of Large-Aspect-Ratio Vermiculite Nanobrick Wall Thin Films. *ACS Appl. Mater. Interfaces* **2012**, *4*, 5529–5533.
- (26) Tzeng, P.; Lugo, E. L.; Mai, G. D.; Wilhite, B. A.; Grunlan, J. C. Super Hydrogen and Helium Barrier with Polyelectrolyte Nanobrick Wall Thin Film. *Macromol. Rapid Commun.* **2015**, *36*, 96–101.
- (27) Ebina, T.; Mizukami, F. Flexible Transparent Clay Films with Heat-Resistant and High Gas-Barrier Properties. *Adv. Mater.* **2007**, *19*, 2450–2453.
- (28) Möller, M. W.; Lunkenbein, T.; Kalo, H.; Schieder, M.; Kunz, D. A.; Breu, J. Barrier Properties of Synthetic Clay with a Kilo-Aspect Ratio. *Adv. Mater.* **2010**, *22*, 5245–5249.
- (29) Kunz, D. A.; Schmid, J.; Feicht, P.; Erath, J.; Fery, A.; Breu, J. Clay-Based Nanocomposite Coating for Flexible Optoelectronics Applying Commercial Polymers. *ACS Nano* **2013**, *7*, 4275–4280.
- (30) Jasmund, K.; Lagaly, G. *Tonminerale und Tone: Struktur, Eigenschaften, Anwendungen und Einsatz in Industrie und Umwelt*; Steinkopff: Darmstadt, 1993.
- (31) Kalo, H.; Möller, M. W.; Kunz, D. A.; Breu, J. How to maximize the aspect ratio of clay nanoplatelets. *Nanoscale* **2012**, *4*, 5633–5639.
- (32) Taruta, S.; Obara, R.; Takusagawa, N.; Kitajima, K. Effect of layer charge on chemical and physical properties of synthetic K-fluorine micas. *J. Mater. Sci.* **2005**, *40*, 5597–5602.
- (33) Meunier, A. Why are clay minerals small? *Clay Miner.* **2006**, *41*, 551–566.
- (34) Walker, G. F.; Garrett, W. G. Complexes of Vermiculite with Amino-Acids. *Nature* **1961**, *191*, 1389–1389.
- (35) Rausell-Colom, J. A.; Saez-Anuon, J.; Pons, C. H. Vermiculite Gelation: Structural and Textural Evolution. *Clay Miner.* **1989**, *24*, 459–478.
- (36) Braganza, L. F.; Crawford, R. J.; Smalley, M. V.; Thomas, R. K. Swelling of n-Butylammonium Vermiculite in Water. *Clays Clay Miner.* **1990**, *38*, 90–96.
- (37) Jimenez de Haro, M. C.; Ruiz-Conde, A.; Perez-Rodriguez, J. L. Stability of n-Butylammonium Vermiculite in Powder and Flake Forms. *Clays Clay Miner.* **1998**, *46*, 687–693.
- (38) Walker, G. F. Macroscopic Swelling of Vermiculite Crystals in Water. *Nature* **1960**, *187*, 312–313.
- (39) McCarney, J.; Smalley, M. V. Electron Microscopy Study of n-Butylammonium Vermiculite Swelling. *Clay Miner.* **1995**, *30*, 187–194.
- (40) Walker, G. F. Vermiculite-Organic Complexes. *Nature* **1950**, *166*, 695–696.
- (41) Williams, G. D.; Skipper, N. T.; Smalley, M. V.; Soper, A. K.; King, S. M. Structure of alkyl ammonium solutions in vermiculite clays. *Faraday Discuss.* **1996**, *104*, 295–306.
- (42) Breu, J.; Seidl, W.; Stoll, A. J.; Lange, K. G.; Probst, T. U. Charge Homogeneity in Synthetic Fluorohectorite. *Chem. Mater.* **2001**, *13*, 4213–4220.
- (43) Ammann, L.; Bergaya, F.; Lagaly, G. Determination of the cation exchange capacity of clays with copper complexes revisited. *Clay Miner.* **2005**, *40*, 441–453.
- (44) Meier, L. P.; Kahr, G. Determination of the cation exchange capacity (CEC) of clay minerals using the complexes of copper(II) ion with triethylenetetramine and tetraethylenepentamine. *Clays Clay Miner.* **1999**, *47*, 386–388.
- (45) Lagaly, G.; Fernandez Gonzalez, M.; Weiss, A. Problems in Layer-Charge Determination of Montmorillonites. *Clay Miner.* **1976**, *11*, 173–187.
- (46) Mermut, A. R.; Lagaly, G. Baseline Studies of the Clay Minerals Society Source Clays: Layer-charge Determination and Characteristics of those Minerals Containing 2:1 Layers. *Clays Clay Miner.* **2001**, *49*, 393–397.
- (47) Stöter, M.; Biersack, B.; Rosenfeldt, S.; Leitl, M. J.; Kalo, H.; Schobert, R.; Yersin, H.; Ozin, G. A.; Förster, S.; Breu, J. Encapsulation of Functional Organic Compounds in Nanoglass for Optically Anisotropic Coatings. *Angew. Chem., Int. Ed.* **2015**, *54*, 4963–4967.
- (48) Goossens, D. Techniques to measure grain-size distributions of loamy sediments: a comparative study of ten instruments for wet analysis. *Sedimentology* **2008**, *55*, 65–96.
- (49) Huve, L.; Delmotte, L.; Martin, P.; le Dred, R.; Baron, J.; Saehr, D. 19F MAS-NMR Study of Structural Fluorine in some Natural and Synthetic 2:1 Layer Silicates. *Clays Clay Miner.* **1992**, *40*, 186–191.
- (50) Keenan, C. D.; Herling, M. M.; Siegel, R.; Petzold, N.; Bowers, C. R.; Rössler, E. A.; Breu, J.; Senker, J. Porosity of Pillared Clays

Studied by Hyperpolarized ^{129}Xe NMR Spectroscopy and Xe Adsorption Isotherms. *Langmuir* **2013**, *29*, 643–652.

(S1) Jagodzinski, H. Eindimensionale Fehlordnung in Kristallen und ihr Einfluss auf die Röntgeninterferenzen. I. Berechnung des Fehlordnungsgrades aus den Röntgenintensitäten. *Acta Crystallogr.* **1949**, *2*, 201–207.

(S2) Stöter, M.; Biersack, B.; Reimer, N.; Herling, M.; Stock, N.; Schobert, R.; Breu, J. Ordered Heterostructures of Two Strictly Alternating Types of Nanoreactors. *Chem. Mater.* **2014**, *26*, 5412–5419.

(S3) Moore, D. M.; Reynolds, R. C. *X-ray Diffraction and the Identification and Analysis of Clay Minerals*, 2nd ed.; Oxford University Press: Oxford, 1997.

(S4) Bailey, S. W. Nomenclature for regular interstratifications. *Clay Miner.* **1982**, *17*, 243–248.

(S5) Möller, M. W.; Hirsemann, D.; Haarmann, F.; Senker, J.; Breu, J. Facile Scalable Synthesis of Rectorites. *Chem. Mater.* **2010**, *22*, 186–196.

(S6) Rosenfeldt, S.; Stöter, M.; Schlenk, M.; Martin, T.; Albuquerque, R. Q.; Förster, S.; Breu, J. In-Depth Insights into the Key Steps of Delamination of Charged 2D Nanomaterials. *Langmuir* **2016**, *32*, 10582–10588.

(S7) Balnois, E.; Durand-Vidal, S.; Levitz, P. Probing the Morphology of Laponite Clay Colloids by Atomic Force Microscopy. *Langmuir* **2003**, *19*, 6633–6637.

6.1.1. Supporting Information

Two-Step Delamination of Highly-charged, Vermiculite-like Layered Silicates via Ordered Heterostructures

Matthias Daab,[†] Sabine Rosenfeldt,^{‡,⊥} Hussein Kalo,[§] Matthias Stöter,[†] Beate Bojer,^{||} Renée Siegel,^{||} Stephan Förster[⊥], Jürgen Senker^{||} and Josef Breu^{*,†,‡}

[†]Lehrstuhl für Anorganische Chemie I, Universität Bayreuth, D-95440 Bayreuth, Germany

[‡]Bayerisches Polymerinstitut, D-95440 Bayreuth, Germany

[⊥]Lehrstuhl für Physikalische Chemie I, Universität Bayreuth, D-95440 Bayreuth, Germany

[§]BYK Chemie GmbH, D-85368 Moosburg, Germany

^{||}Lehrstuhl für Anorganische Chemie III, Universität Bayreuth, D-95440 Bayreuth, Germany

Supporting Information

Content:

1. Supporting Data
 - Scanning Electron Microscopy
 - ¹⁹F-NMR-Spectroscopy
 - CHN-Analysis and Distribution Equilibrium
 - PXRD of Partial Ion-Exchange
 - Humidity-dependent d-spacings
 - Static Light Scattering
 - C4-Vermiculite at 95% relative humidity
 - Calculations: d-spacing of a Gel
2. Supporting References

Ergebnisse

1. Supporting Data

Scanning Electron Microscopy.

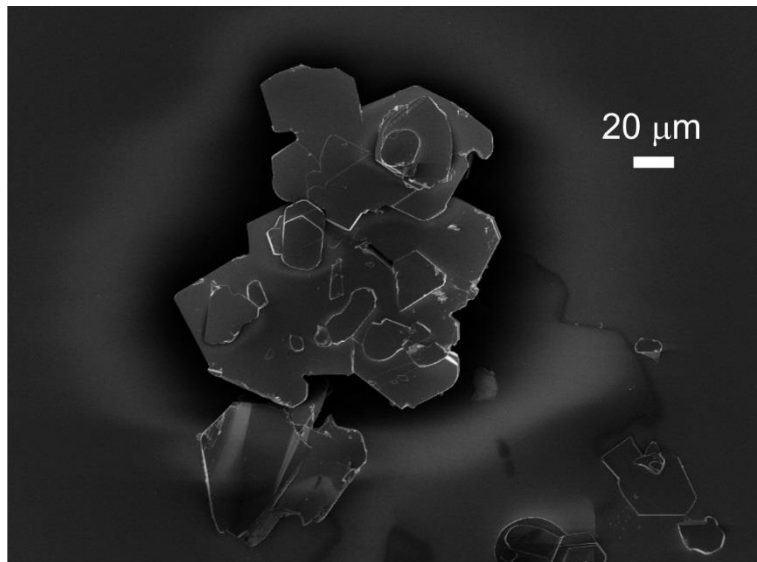


Figure S1. SEM of a Na-Hec agglomerate as obtained from melt synthesis.

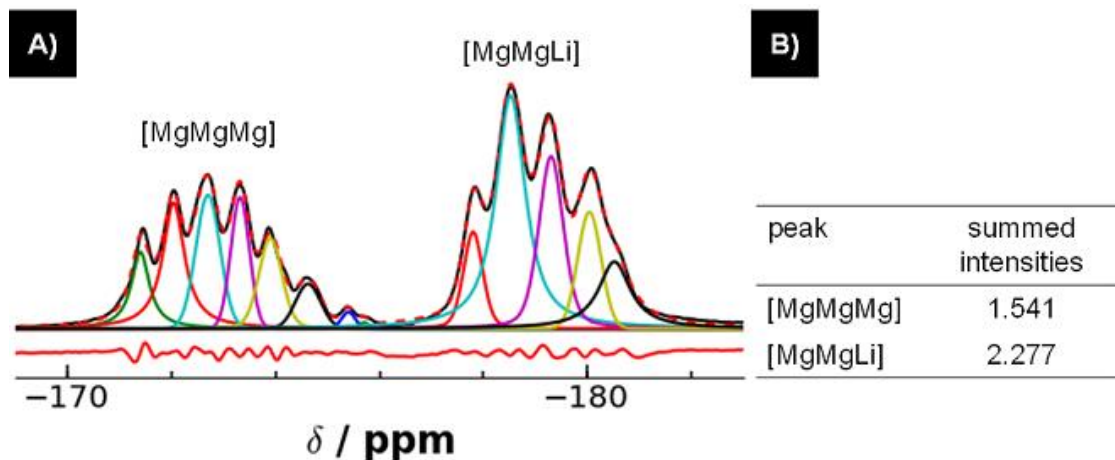
¹⁹F-NMR-Spectroscopy.

Figure S2. (A) shows the ¹⁹F-NMR of Na-Hec with two separated bands that can be assigned to [MgMgMg]- and [MgMgLi]-environments of ¹⁹F in the octahedral layer.¹ As no other fluorine sites were detected, the obtained Na-Hec is therefore perfectly trioctahedral. Deconvolution was performed using Pseudo-Voigt-functions with the same FWHM for Gaussian- and Lorentzian-part. Part (B) of the same figure shows the summed intensities of the two peaks.

Calculations of the composition of the octahedral layer based on these integrals are explained in the following.

First the site intensities belonging to Mg (S_{Mg}) and to Li (S_{Li}) are calculated from the integrals (I):

$$S_{Mg} = 3 \cdot I_{[MgMgMg]} + 2 \cdot I_{[MgMgLi]} = 9.177 \quad (1)$$

$$S_{Li} = 1 \cdot I_{[MgMgLi]} = 2.277 \quad (2)$$

The total intensity is obtained by summation:

$$S_{total} = S_{Mg} + S_{Li} = 11.454 \quad (3)$$

As there are three octahedral positions surrounding each structural F ion which are fully occupied for trioctahedral clay minerals, the stoichiometry of the octahedral layer (O) can be calculated:

$$O_{Mg} = \frac{3}{S_{total}} \cdot S_{Mg} = 2.40 \quad (4)$$

$$O_{Li} = \frac{3}{S_{total}} \cdot S_{Li} = 0.60 \quad (5)$$

Hence the layer charge per formula unit Si₄O₁₀F₂ according to the obtained octahedral composition [Mg_{2.40}Li_{0.60}]^{okt.} is 0.60.

Ergebnisse

CHN-Analysis and Distribution Equilibrium.

Carbon content was determined by CHN-analysis. The molar mass of the partial exchanged phase $[Na_{0.6-y}C4]^{inter}$ varies with the amount of n-butylammonium intercalated. Carbon content therefore has to be calculated iteratively. By this means y is varied till the molar mass of $[C4_yNa_{0.60-y}]^{inter} \cdot [Mg_{2.4}Li_{0.6}]^{oct} \cdot <Si_4>^{tetr} \cdot O_{10}F_2$ is equal to the experimentally determined carbon content.

Example: OI-Hect (Addition of 74% CEC) features an experimental carbon content of 3.288 wt% as determined by CHN. $y=0.2741$ leads to a carbon content of 3.288 wt% which is in line with the experimentally determined one. Therefore OI-Hect features a formula of $[Na_{0.33}C4_{0.27}]^{inter} \cdot [Mg_{2.4}Li_{0.6}]^{oct} \cdot Si_4O_{10}F_2$. Hence 46 % of interlayer ions are exchanged ($0.2741 : 0.60 = 45.7\%$). As 75 % of CEC of Na-Hect have been added, 39 % of n-butylammonium ions are remaining in solution ($100\% - 45.7\% : 75\% = 39.1\%$).

Data following this calculation for all partial exchanged products (15 to 200% of CEC) are given in Table S1 along with the carbon content of C4-Hec. This table is plotted in Figure S3.

Table S1. Distribution equilibrium for partial exchange of Na-Hec with n-butylammonium (C4) as determined by CHN-analysis.

Addition C4 [% of CEC]	C-content [Gew.%]	Na [p.f.u.]	C4 [p.f.u.]	C4 intercalated [% of CEC]	C4 remaining in solution [% of addition]
15	0.696	0.54	0.06	9	37
30	1.366	0.49	0.11	19	38
45	1.999	0.44	0.16	27	39
60	2.842	0.36	0.24	39	35
74	3.288	0.33	0.27	46	39
90	3.815	0.28	0.32	53	41
105	4.105	0.26	0.35	58	45
125	5.139	0.16	0.44	73	42
150	6.099	0.08	0.53	88	42
200	6.632	0.03	0.57	96	52
C4-Hec, complete exchange	6.935	0.00 (-0.003)	0.60 (0.603)		

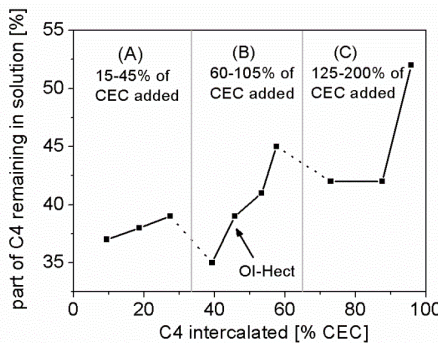


Figure S3. Distribution equilibrium of the partial exchange of Na-Hec with n-butylammonium. The part of n-butylammonium remaining in solution is plotted over the amount intercalated for different amounts of CEC added to the neat hectorite.

PXRD of Partial Ion-Exchange.

Table S2. $00l$ -series and coefficient of variation (cv) for different stages of partial exchange in % of CEC of Na-Hect (at 43 % r.h.).

$00l$	$d(00l)$ for different additions of C4 in % of CEC of Na-Hect						
	60 %	67 %	70 %	72 %	74 %	76 %	90 %
001	25.282	25.000	25.078	25.120	25.392	24.845	24.861
002	12.663	12.616	12.650	12.644	12.745	12.615	12.724
004	6.346	6.336	6.344	6.344	6.367	6.338	6.372
005	5.103	5.098	5.093	5.086	5.105	5.069	5.041
006	4.234	4.230	4.233	4.233	4.243	4.234	4.243
007	3.636	3.641	3.639	3.635	3.642	3.625	3.616
008	3.175	3.174	3.176	3.176	3.183	3.174	3.180
009	2.834	2.832	2.831	2.830	2.835	2.824	2.816
0011	2.317	2.316	2.316	2.316	2.320	2.314	2.308
0012	2.119	2.118	2.119	2.119	2.121	2.118	2.119
0013	1.961	1.961	1.961	1.959	1.963	1.958	1.953
0014	1.815	1.816	1.816	1.816	1.819	1.816	1.821
0016	1.588	1.589	1.589	1.590	1.591	1.590	1.594
average							
$d(00l) \cdot l [\text{\AA}]$	25.42	25.39	25.40	25.38	25.48	25.32	25.37
cv [%]	0.27	0.55	0.44	0.39	0.14	0.65	0.68

Ergebnisse

Humidity-dependent d-spacings.

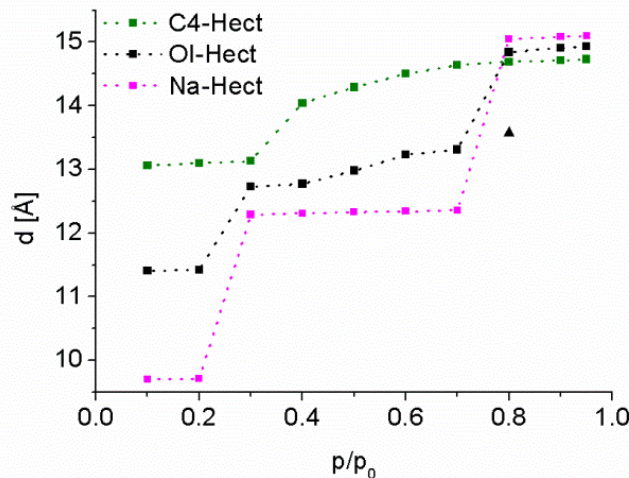


Figure S4. Humidity dependent d-spacings of C4-Hect (d_{001}), OI-Hect (d_{002}) and Na-Hect (d_{001}) measured in a humidity chamber. For the homoionic phases d_{001} is shown. In case of OI-Hect d_{002} is shown that corresponds to the averaged d-spacing of the superstructure. A slight shoulder at about 13.6 \AA ($p/p_0 = 0.8$) is marked by a triangle. D-spacings at $p/p_0 = 0.98$ did not deviate from the d-spacings measured under a drop of ethanol/water (1:1).

Static Light Scattering.

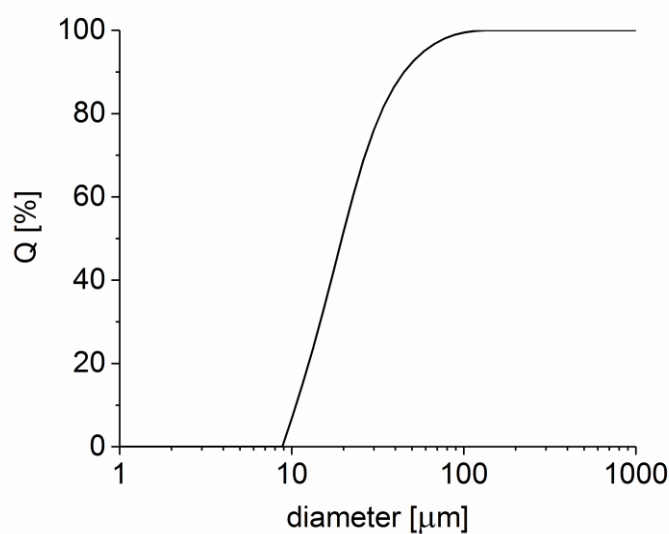


Figure S5. Particle size distribution as determined by SLS, the number weighting yields an average diameter of $24 \mu\text{m}$.

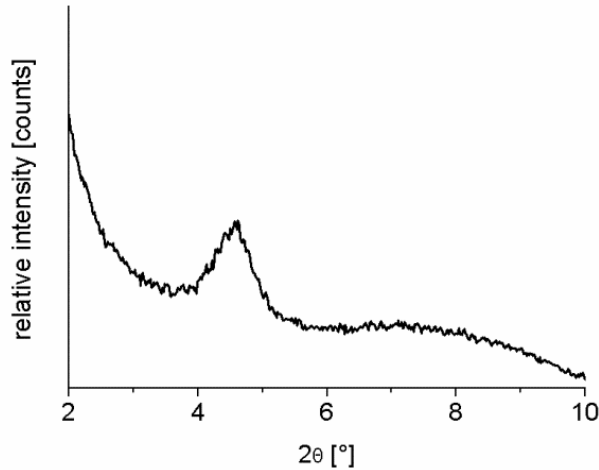
C4-Vermiculite at 95% relative humidity.

Figure S6. PXRD of a n-butylammonium exchanged vermiculite (Eucatex) measured in a humidity chamber at 95% relative humidity with a d-spacing of 19.2 Å.

Calculations: d-spacing of a Gel.

The d-spacing of a homogeneously swollen gel can be calculated via the volume fraction ϕ using the thickness of a single lamella D:

$$\phi = \frac{m_{Hec}/\rho_{Hec}}{m_{Hec}/\rho_{Hec} + m_{water}/\rho_{water}} \quad (1)$$

$$d = \frac{D}{\phi} \quad (2)$$

Ergebnisse

2. Supporting References

- (1) Huve, L.; Delmotte, L.; Martin, P.; le Dred, R.; Baron, J.; Saehr, D. ¹⁹F MAS-NMR Study of Structural Fluorine in some Natural and Synthetic 2:1 Layer Silicates. *Clays Clay Miner.* **1992**, *40*, 186-191.

6.2. Kriterien für das Einsetzen der repulsiven osmotischen Quellung

Matthias Daab,[†] Natalie J. Eichstaedt,[†] Christoph Habel,[†] Sabine Rosenfeldt,[‡] Hussein Kalo,[§] Hubert Schießling,[§] Stephan Förster^{*⊥} and Josef Breu^{*†}

The Onset of Osmotic Swelling in Highly Charged Clay Minerals

Submitted to Langmuir (14.02.2018)

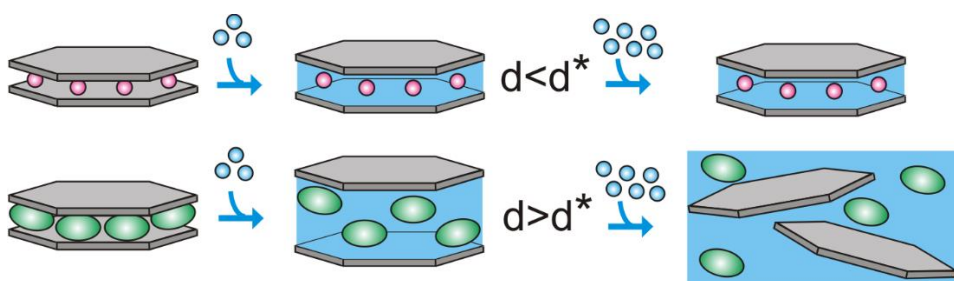
Reprinted with permission, Copyright (2018) American Chemical Society.

[†]Bavarian Polymerinstitute and Department of Chemistry, University of Bayreuth, D-95440 Bayreuth, Germany

[‡]Bavarian Polymerinstitute, D-95440 Bayreuth, Germany

[§]BYK Chemie GmbH, D-85368 Moosburg, Germany

[⊥]Forschungszentrum Jülich, Institute of Complex Systems (ICS-1), D-52425 Jülich, Germany



Darstellung des Eigenanteils:

Das Konzept der Publikation von experimenteller Seite wurde von mir erarbeitet. Das Manuskript wurde hauptsächlich von mir verfasst und wurde hauptsächlich mit Prof. Dr. Josef Breu zur Einreichung überarbeitet. Prof. Dr. Stephan Förster steuerte hierbei die Idee und die Ausarbeitung des Modells zur qualitativen Abschätzung des osmotischen Druckes bei. Von mir wurden die Auswertungen und Interpretationen der Experimente durchgeführt. Die Experimente und Messungen wurden von mir bzw. unter meiner Anleitung von Natalie Eichstaedt im Rahmen ihrer Bachelorarbeit durchgeführt.

Dr. Sabine Rosenfeldt half bei SAXS-Messungen. Christoph Habel, Dr. Hussein Kalo und Dr. Hubert Schießling trugen zur wissenschaftlichen Diskussion bei. Textauszüge des Manuskriptes habe ich für eine Patentanmeldung vor dem Einreichen dieser Arbeit zur Verfügung gestellt. Mein Eigenanteil beträgt ca. 70 %.

Veröffentlichung nach Fertigstellung dieser Arbeit:

Langmuir 2018, 34, 8215-8222.

<http://dx.doi.org/10.1021/acs.langmuir.8b00492>

The Onset of Osmotic Swelling in Highly Charged Clay Minerals

Matthias Daab,[†] Natalie J. Eichstaedt,[†] Christoph Habel,[†] Sabine Rosenfeldt,[†] Hussein Kalo,[‡] Hubert Schießling,[‡] Stephan Förster[§] and Josef Breu^{*†}

[†]Bavarian Polymerinstitute and Department of Chemistry, University of Bayreuth, D-95440 Bayreuth, Germany

[‡]BYK Chemie GmbH, D-85368, Moosburg, Germany

[§]Forschungszentrum Jülich, Institute of Complex Systems (ICS-1), D-52425 Jülich, Germany

KEYWORDS *layered silicate, vermiculite, delamination, exfoliation, osmotic swelling, macroscopic swelling, n-butylammonium, graphene, nanosheet.*

ABSTRACT: Delamination by osmotic swelling of layered materials is generally thought to become increasingly difficult, if not impossible, with increasing layer charge density because of strong Coulomb-interactions. Nevertheless, for the class of 2:1 layered silicates, very few examples of delaminating organo-vermiculites were reported in literature. We propose a mechanism for this repulsive osmotic swelling of highly charged vermiculites based on repulsive counter ion translational entropy that dominates the interaction of adjacent layers above a certain threshold separation. Based on this mechanistic insight, we were able to identify several organic interlayer cations appropriate to delaminate highly charged, vermiculite-type clay minerals. These findings suggest that the osmotic swelling of highly charged organo-clays is a generally applicable phenomenon rather than the odd exemption.

INTRODUCTION

One major advantage of charged two dimensional materials like clay minerals,¹⁻³ lepidocrocite-type titanates⁴⁻⁶ or layered antimony phosphates⁷ over graphite⁸⁻¹⁰ is their capability to delaminate by osmotic swelling. Osmotic swelling leads to the formation of 2D-nanosheets of structure-inherent thickness and represents a gentle top-down procedure guaranteeing a maximization of aspect ratio.^{6, 11} The high aspect ratio restricts free rotation and consequently suspensions with a clay content of ~2 wt% represent liquid-crystalline phases and the various phases have been structurally characterized in detail.¹²⁻²⁰

The osmotic swelling of low layer charged smectite-type clays is thought to be driven by the hydration of interlayer cations like Na⁺ winning over the attractive electrostatic interaction of interlayer cations and silicate layers. This led to a widely accepted upper limit of the layer charge (x) of 0.55 per formula unit Si₄O₁₀F₂ (half a unit cell, p.f.u.) that still allows delamination.²¹ Higher layer charges cannot be delaminated as periodic Coulomb attraction dominates over the hydration of the interlayer cation and limits swelling to the crystalline swelling regime. This swelling regime includes one layer, two layer and three layer hydrates corresponding to d-spacings of ~12, ~15 and ~18 Å, respectively.²²⁻²⁷

Quite counterintuitively, very few examples of osmotic swelling in highly charged vermiculites were reported. For instance Na-vermiculites were reported to swell upon addition of zwitter-ionic aminoacids.^{28,29} Even more surprising Na-Vermiculites that have been cation exchanged with less hydrophilic n-butylammonium (C4) swell osmotically,³⁰⁻³⁴

while C4-smectites do not osmotically swell but form crystalline hydrates with a basal spacing of 14.7 Å in water.³⁵ The only explanation for the osmotic swelling of C4-vermiculites has been proposed by Lagaly.³⁶ He claims that the relatively high charge density of vermiculites forces n-butylammonium into a paraffinic arrangement and that such inclined orientations of alkyl-chains tend to be more readily hydrated than a flat lying alkyl-chain. Therefore, for short chains as in n-ethylammonium-vermiculites the energetics would rather be governed by electrostatic attraction preventing osmotic swelling. Chains longer than n-butyl-chains in turn would no longer be hydrophilic despite a paraffinic orientation but rather hydrophobic and would therefore also not swell osmotically.

Clearly, a general concept explaining the swelling behavior of highly charged clay minerals that is not limited to n-alkylammonium would be highly desirable. This would open the door for easy delamination of vermiculites, which tend to have large platelet diameters and where hence delamination produces nanoplatelets with huge aspect ratio.

We recently proposed that the interaction of adjacent layers is repulsive above at a certain threshold separation. For smectites this threshold separation is met for the three water layer hydrate (~18 Å) leading to osmotic swelling when immersing smectites into water.³⁷ Highly charged Na-vermiculites, however, when immersed in water, only swell to the two water layer hydrate (~15 Å). This layer separation apparently is below the threshold separation and consequently Na-vermiculites do not swell osmotically.

Ergebnisse

To validate and expand our model for repulsive osmotic swelling to the class of highly charged vermiculite-type 2:1 layered silicates, we test various hydrophilic organo-cations capable to overcome the threshold separation by a steric contribution.

EXPERIMENTAL

Synthesis and Characterization of the Clays. A low charged Na-fluorohectorite $\text{Na}_{0.5}\text{Mg}_{2.5}\text{Li}_{0.5}\text{Si}_4\text{O}_{10}\text{F}_2$ (Hec) and a vermiculite-type, highly charged Na-fluorohectorite $\text{Na}_{0.75}\text{Mg}_{2.25}\text{Li}_{0.75}\text{Si}_4\text{O}_{10}\text{F}_2$ (Verm) with a charge density in the range of vermiculites were prepared by melt synthesis according to a published procedure followed by annealing (6 weeks, 1045 °C) to improve charge homogeneity and phase purity.¹¹ These steps were carried out in gas tight molybdenum crucibles. The educts NaF (99.995%, Alfa Aesar), LiF (>99.9%, ChemPur), MgF₂ (>99.9%, ChemPur), MgO (99.95%, Alfa Aesar) and SiO₂ (Merck, fine granular quarz, purum) are mixed according to the nominal composition. The crucible was ramped to 1750 °C (15 °C/min), held at this temperature for 70 min, cooled to 1300 °C (55 °C/min) and then to 1050 °C (10 °C/min). Finally, it was quenched by switching of the power. The cation exchange capacity was determined according to DIN ISO 11260 using BaCl₂ and the layer charge density was determined according to Lagaly.^{38,39}

Powder X-ray Diffraction. Powder X-ray diffraction (PXRD) patterns of as-synthesized clays were recorded on a STOE Stadi P powder diffractometer using Cu K α_1 radiation. The samples were placed in a glass capillary. Prior to measurement samples were equilibrated for one week over saturated K₂CO₃-solution (43 % relative humidity, r.h.) to obtain the one water layer hydrate. After equilibration, the capillaries were sealed. All other PXRD were measured with textured samples in Bragg-Brentano geometry on a PANalytical X'pert Pro equipped with an X'Celerator Scientific RTMS detector (Cu K α radiation). PXRD patterns at fixed relative humidities were recorded in a temperature-humidity chamber (Anton Paar temperature humidity chamber driven by a VTI corp. RH-200 humidity generator) mounted on the PANalytical Xpert Pro. Dry samples were obtained by drying at 110°C under vacuum for 24 h and PXRDs of the hot samples were measured within 2 min each after removal from the vacuum furnace.

Microprobe Analysis. The chemical composition of Hec and Verm was determined by wavelength dispersive X-ray spectroscopy on crystals with flat lying surfaces on a carbon tape using an electron microprobe (Jeol JXA-8200, Bayerisches Geoinstitut, Bayreuth). The settings were 15 kV acceleration voltage, 15 nA initial beam current, a beam spot diameter of 10 μm , 10 s counting time at the peak position and 5 s counting time at each side of the peak.

Inductive-coupled plasma atomic emission spectroscopy (ICP-OES). The lithium and magnesium content of Hec and Verm was determined by ICP-OES. Samples of about 20 mg of dry clay were weighed into clean Teflon flasks of 15 mL volume. After addition of 1.5 mL 30 wt. % HCl (Merck), 0.5 mL of 85 wt. % H₃PO₄ (Merck), 0.5 mL 65 wt. % HNO₃ (Merck) and 1 mL of 48 wt. % HBF₄ (Merck) the sample was digested in a MLS 1200 Mega microwave digestion apparatus for 6.5 min and heated at 600W (MLS GmbH, Mikrowellen-Labor-Systeme, Leutkirch, Germany). The closed sample container was cooled to room temperature and the clear solution was diluted to 100 mL in a volumetric flask and analyzed on Vista-PRO radial spectrometer.

Preparation of organo-cations. Diethylaminoethanol (DEAE, >99.5%, Aldrich), 2-Amino-2-(hydroxymethyl)-1,3-

propanediol (TRIS, >99%, Aldrich), n-Butlyamin (C4, 99.5%, Aldrich) were titrated in Millipore-water to pH = 7 with HCl. The solutions were diluted to 1 molL⁻¹. 2-(Dimethylamino)ethyl methacrylate (DMAEMA, 98%, Aldrich) was methylated with Methyliodide resulting in TMAEMA-iodide: DMAEMA (10 g) was dissolved in acetone (1 L) and methyl iodide was added at a molar ratio of 1.5 compared to amino groups. The mixture was stirred overnight. The precipitate was washed several times with acetone and finally dried using high vacuum. Completeness of quaternization was approved by ¹H-NMR. TMAEMA-iodide was dissolved in Millipore-water to yield a 1 molL⁻¹ solution.

Ion-exchange to Organo-Clays. 200 mg of the clays were suspended in 10 mL of a 1 M solution of the organic salt (> 25-fold excess of the CEC, delamination is prevented by the high ionic strength). The procedure was repeated 5 times. Finally, the obtained organo-clays were washed free of halide-ions (AgNO₃-test) with Millipore-water. Gels were concentrated by centrifugation between the washing cycles. The organo-clays were finally washed one times with acetone and dried at 60°C. The only exception are TMAEMA-exchanged clays that were freeze-dried from water, in order to prevent the polymerization of TMAEMA resulting in polycations, that render osmotic swelling impossible.

CHN-Analysis. A PerkinElmer 2400 CHN equipped with a combustion tube filled with tungsten(VI)-oxide-granules was used at a combustion temperature of 1050 °C. Samples were dried at 110 °C and vacuum for 24 h and stored in a glovebox prior to measurement.

Scanning Electron Microscopy and Energy Dispersive X-ray Spectroscopy (REM-EDX). REM-EDX was measured on a Zeiss 1530 with a EDX INCA 400 unit (Oxford). Samples were prepared on a carbon tape and sputtered with 10 nm carbon.

Small angle X-ray scattering (SAXS). SAXS data were measured using a “Double Ganesh AIR” system (SAXSLAB, Denmark). The X-ray source of this laboratory-based system is a rotating anode (copper, MicroMax 007HF, Rigaku Corporation, Japan) providing a micro-focused beam. The data are recorded by a position sensitive detector (PILATUS 300K, Dectris). Samples were prepared by adding a defined amount of millipore-water to the dry organo-clay. After equilibration for one week SAXS-patterns were recorded in 1 mm glass capillaries.

Gravimetric analysis of water content. TRIS-Hec and DEAE-Hec were dried (110°C, vacuum, 24 h) prior to weighing. Their water uptake at 98 % r.h. (48 h equilibration in the atmosphere of saturated K₂SO₄-solution) was determined gravimetrically.

Ergebnisse

RESULTS AND DISCUSSION

Synthesis and Characterization of the Clays.

PXRD patterns of Hec and Verm recorded at 43 % r.h. (Figure 1) indicate a crystalline swollen phase with one layer of water molecules in the interlayer space ($d_{001} = 12.5 \text{ \AA}$).⁴⁰ All lines can be indexed in C2/m (No. 12). Least squares refinement resulted in the following lattice parameters: Hec ($a = 5.20(1) \text{ \AA}$, $b = 9.10(1) \text{ \AA}$, $c = 12.48(4) \text{ \AA}$, $\gamma = 95.44(4)^\circ$) and Verm ($a = 5.26(1) \text{ \AA}$, $b = 9.07(2) \text{ \AA}$, $c = 12.48(4) \text{ \AA}$, $\gamma = 95.22(4)^\circ$).

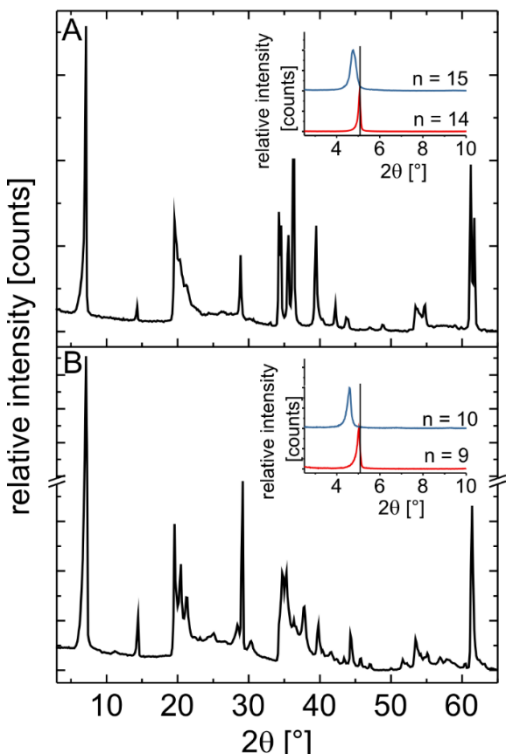


Figure 1. A) PXRD patterns of Hec (A) and of Verm (B) at 43% r.h.; the insets show PXRD patterns of dried, textured samples of the n-alkylammonium intercalates ($C_nH_{2n+1}NH_3^+$) of Hec for $n = 14$ (red) and $n = 15$ (blue) and of Verm for $n = 9$ (red) and $n = 10$ (blue). The straight line ($d = 17.6 \text{ \AA}$) equals the d -spacing of a bilayer of n-alkylammonium ions in the interlayer space.

The chemical composition was determined by microprobe analysis. Microprobe analysis is insensitive to Li. Therefore, the Mg/Li-ratio was derived from ICP-OES analysis by assuming a complete occupancy of the tetrahedral positions ($Si = 4$) and by normalizing stoichiometric coefficients of the cations to match the 22 negative charges of the anionic sublattice ($O_{10}F_2$). This way a composition of $Na_{0.52(2)}Mg_{2.51(4)}Li_{0.46(2)}Si_4O_{10}F_2$ is obtained for Hec (nominally $Na_{0.5}^{inter}[Mg_{2.5}Li_{0.5}]^{oct}<Si_4>^{tetr}O_{10}F_2$) and a composition of $Na_{0.71(4)}Mg_{2.28(4)}Li_{0.72(4)}Si_4O_{10}F_2$ is obtained for Verm (nominally $Na_{0.75}^{inter}[Mg_{2.25}Li_{0.75}]^{oct}<Si_4>^{tetr}O_{10}F_2$). Cation exchange capacities (CEC) as determined by the BaCl₂-method are close to the CECs expected according to the nominal composition: 129 meq/100 g for Hec (130 meq/ 100 g nominally) and 185 meq/100 g for Verm (194 meq/100 g nominally). The layer charge density was determined experimentally by the method of Lagaly.^{38,39} For this purpose, interlayer Na⁺ is exchanged with n-alkylammonium ($C_nH_{2n+1}NH_3^+$, Figure 1, insets) for which the charge equivalent area per charge (of a flat lying molecule) is known for a dense packing of either flat lying mono- ($d_{001} = 13.4 \text{ \AA}$) or bilayers ($d_{001} = 17.6 \text{ \AA}$). The onset of the transition of mono- to bi-

layer- or from bilayer to pseudo-trilayer arrangement with increasing chain length was converted into upper limits of charge densities (Table S1). As described by Lagaly for some natural vermiculites with $x \sim 0.7$ p.f.u., Verm forms bilayers instead of paraffinic structures with $n > 7$.³⁹ Therefore for both, Hec and Verm the charge density could be determined from the onset of the transition from bilayer ($d_{001} = 17.6 \text{ \AA}$) to pseudo-trilayer: Once charge neutrality can no longer be realized with a densely packed bilayer some pseudo-trilayers have to be mixed in to maintain charge neutrality. As a consequence of this random interstratification the basal spacing starts shifting and at the same time its full width of half maximum increases.

In case of Hec (Figure 1A, inset) $n = 14$ is the longest chain that can saturate the charge of the clay by a bilayer occupancy (red trace, $d_{001} = 17.6 \text{ \AA}$). For $n = 15$ (blue trace) the d -spacing is clearly shifted. A dense bilayer of $n = 14$ corresponds to a layer charge of $x = 0.51$ p.f.u., whereas a dense bilayer of $n = 15$ corresponds to a layer charge of $x = 0.48$ p.f.u.; the layer charge of Hec is consequently in the range of $0.51 \geq x \geq 0.48$ p.f.u.. In case of Verm (Figure 1B, inset) $n = 9$ is the longest chain that can saturate the charge of the clay by a bilayer occupancy (red trace, $d_{001} = 17.6 \text{ \AA}$). For $n = 10$ (blue trace) the d -spacing is clearly shifted. A dense bilayer of $n = 9$ corresponds to a layer charge of $x = 0.73$ p.f.u., whereas a dense bilayer of $n = 10$ corresponds to a layer charge of $x = 0.67$ p.f.u.; the layer charge of Verm is consequently in the range of $0.73 \geq x \geq 0.67$ p.f.u.. The layer charge densities as determined by Lagaly agrees well with what is expected based on the nominal compositions. Within experimental errors, all analytical data are in line with the nominal composition suggesting that no amorphous impurities are left after long-term annealing of Hec and Verm.

Swelling Behavior of Organo-Clays.

Lagaly stated that “this reaction [the delamination of n-butylammonium vermiculites] is difficult to understand”.⁴¹ He argued that for gel-forming C4-exchanged vermiculites the arrangement of water molecules around the n-butylammonium chain might play a role.³⁶ In an attempt to validate the universality of osmotic swelling of highly charged organo-clays, both, Hec and Verm were ion-exchanged with hydrophilic organic cations (n-butylammonium (C4), 2-Ammonium-2-(hydroxymethyl)-1,3-propanediol (TRIS), Diethylammoniummethanol (DEAE) and 2-(Trimethylammonium)ethyl methacrylate (TMAEMA)). This organo-cations vary in charge equivalent areas and therefore differ in steric demand of a completely ion-exchanged organo-clay. The degree of ion exchange was checked by CHN- and EDX-analysis of residual Na⁺ (Table S2). Exchange was found to be complete for C4-, TRIS- and DEAE-Hec. In case of TMAEMA-Hec 92% of Na-ions were exchanged. In case of C4- and TRIS-Verm exchange is complete according to CHN-analysis, although minor amounts of Na⁺ are still detected with EDX (~2-3 % CEC). In DEAE- and TMAEMA-Verm ~90 % of Na-ions could be exchanged.

The swelling behavior of the Na- and the organo-clays was monitored by SAXS. Hereby, the samples were suspended in a defined amount of Millipore-water (Figure 2).

Ergebnisse

expected for TRIS-Verm), 131 Å (6.9 vol%, 139 Å expected for DEAE-Verm), 189 Å (5.2 vol%, 185 Å expected for TMAEMA-Verm). Only for C4-Verm a separation of 175 Å is found that is clearly beyond expectations (9.3 vol%, 103 Å expected). At the same time part of the C4-Verm does not swell beyond $d = 19.6 \text{ \AA}$. This would suggest that this part adopts a different interlayer structure showing a diverging hydration behavior. As a consequence, the observed layer separation in the gel phase is larger than expected because the clay content in this volume is depleted by the segregation of the 19.6 Å-phase. The reason for the heterogeneity in respect to intracrystalline reactivity for this particular organo-clay is unknown. However, similar observations were made for natural C4-Vermiculites previously as well.³³

The striking difference in swelling extent in water observed for organo-Hec- and organo-Verm is to some extent reflected in the crystalline swelling behavior in humid air (Figure 3). Unfortunately, a large gap in water activity between humid air and liquid water (55.5 mol/L) arises for experimental reasons. At 98 % relative humidity (r.h.) both Na-Hec and Na-Verm swell to crystalline 2 water layer hydrates (15.1 Å). While Na-Hec and Na-Verm show the same hydrated states, the increase in d-spacing upon hydration in humid air of organo-Verm is systematically higher than of organo-Hec (Figure 3, values for all d-spacings: Table S3). The maximum d-spacings of all organo-Verm samples significantly exceed the d-spacing of the two water layer structure of Na^+ and also of their organo-Hec counterparts.

A subtle interplay of hydrophilicity, the charge equivalent area of interlayer cations (area occupied per charge of a flat lying molecule, A_1) and the charge density of the clay controls the extent of crystalline swelling upon changing the water activity from 0 % to 98 % r.h.. The charge densities of the clay $x \sim 0.7 \text{ p.f.u.}$ (Verm) and $x \sim 0.5 \text{ p.f.u.}$ (Hec) can be converted to charge equivalent areas (A_C) of $\sim 34 \text{ \AA}^2/\text{charge}$ (Verm) and $\sim 48 \text{ \AA}^2/\text{charge}$ (Hec) that are available in the interlayer space to balance the clay's charge.³⁸ If the ratio of A_1/A_C becomes significantly larger than 1 a flat lying monolayer arrangement is no longer capable of balancing the clay's permanent charge and organo-cations start exerting a steric pressure that eventually will increase the d-spacing.

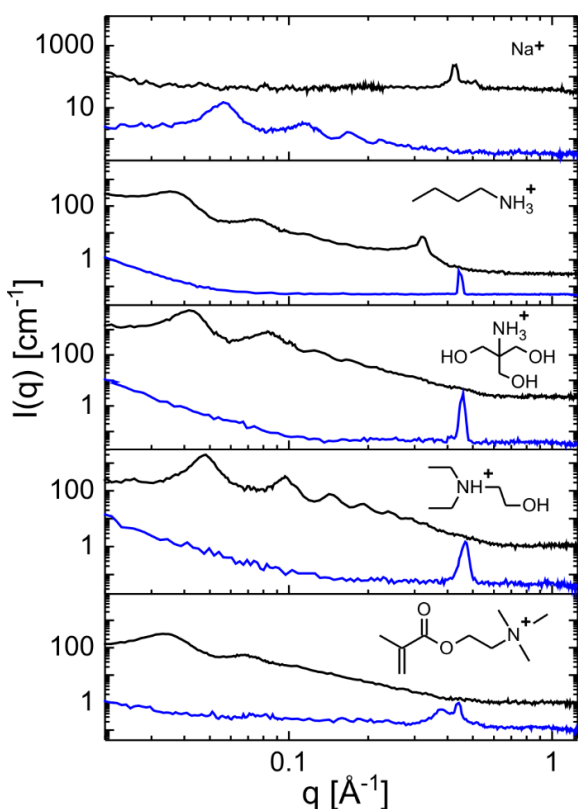


Figure 2. SAXS-patterns of organo-Clays in water of Verm (black) and Hec (blue). Interlayer ions are (from top to bottom): Na^+ , C4, TRIS, DEAE and TMAEMA.

Because of different charge densities organo-Hec and organo-Verm display different swelling behaviors. As expected, highly charged Na-Verm is not able to delaminate in water by repulsive osmotic swelling. Swelling of Na-Verm is rather limited to crystalline swelling with a d-spacing of 15.1 Å ($q = 0.42 \text{ \AA}^{-1}$, two water layer hydrate). In contrast, as reported before, a gel is obtained by repulsive osmotic swelling for Na-Hec.³⁷ Because of the large diameter individual layers cannot rotate freely and the gel formed represents a lamellar liquid crystal. Adjacent silicate layers are separated to a distance corresponding to the clay/water-ratio: For instance, for the dispersion with a volume fraction of $\phi = 8.4 \text{ vol\%}$ adjacent silicate layers are separated to $d = 112 \text{ \AA}$ ($q = 0.056 \text{ \AA}^{-1}$). This is in line with the expected value of 114 Å for this volume fraction based on a lamella thickness of 9.6 Å ($d_{\text{expected}} = 9.6 \text{ \AA} / \phi$; Supporting Information). This suggests that by the repulsive nature of the osmotic swelling all layers are separated to the same distance. The sample is homogeneously swollen and the gel is representing a mono-phase gel. The Na-clays follow the expectations inasmuch as the degree of swelling decreases with increasing layer charge and stronger electrostatic attraction of silicate layers with interlayer cations.

These expectations are seriously messed up when looking at the organo-clays: Whereas for the low charged Hec swelling is limited to the crystalline regime ($d < 25 \text{ \AA}$, $q > 0.25 \text{ \AA}^{-1}$) for all organo-Verm samples repulsive osmotic swelling is observed with a typical separation $> 100 \text{ \AA}$ ($q < 0.06 \text{ \AA}^{-1}$). Please note, that the d-spacing increases linearly with decreasing clay content in the concentration regime $> 2 \text{ vol\%}$ (where $d_{\text{expected}} = 9.6 \text{ \AA} / \phi$ is valid), we therefore used concentrations of 5 – 10 vol%.

Organic-Verm samples swell osmotically to mono-phase gels as validated by the d-spacings of 150 Å (6.7 vol%, 143 Å

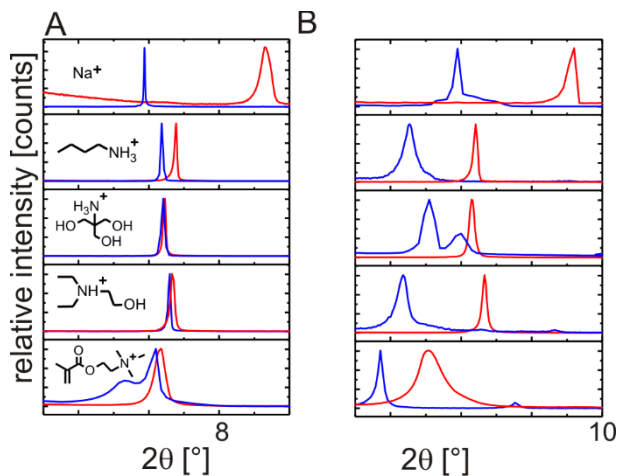


Figure 3. PXRD pattern of (organo-)clays, Hec (A) and Verm (B). Red traces represent dry samples while the blue traces represent samples at 98 % r.h..

Ergebnisse

The charge equivalent areas of the organo cations were calculated by chemicalize.org (ChemAxon)⁴² as their maximum projection areas (35 \AA^2 C4, 37 \AA^2 TRIS, 41 \AA^2 DEAE and 60 \AA^2 TMAEMA). All A_l of these organo-cations are significantly larger than A_l of interlayer $[\text{Na}(\text{H}_2\text{O})_6]^+$ ($\sim 12 \text{ \AA}^2$)⁴⁰ which is found in 2 water layer hydrate. The pronounced difference in charge equivalent areas of Verm ($\sim 34 \text{ \AA}^2$) and Hec ($\sim 48 \text{ \AA}^2$) in collaboration with the packing arrangement of the specific interlayer cation will influence both, the d-spacing and the packing density of the interlayer space. Unfortunately, for layered systems, observed d-spacings may shift either because the interlayer structure is changing the same way in each interlayer or because interlayer spaces with a larger d-spacing are mixed in randomly (interstratified). Moreover, the hydration enthalpy in a first approximation scales with the number of interlayer cations p.f.u. and at the same time the Coulomb attraction in the 1-dimensional crystal increases with charge density of the clay. The complex interplay of all these factors renders the degree of swelling unpredictable and quite counterintuitive behavior is observed:

For instance, while for C4-Hec the d-spacing increases from $d_{\text{dry}} = 13.3 \text{ \AA}$ to $d_{98\%r.h.} = 14.1 \text{ \AA}$ ($\Delta d = 0.8 \text{ \AA}$), C4-Verm expands from $d_{\text{dry}} = 13.8 \text{ \AA}$ to $d_{98\%r.h.} = 19.7 \text{ \AA}$ ($\Delta d = 5.9 \text{ \AA}$). This much higher increase for C4-Verm despite the much higher Coulomb attraction is surprising.

More striking is the case of DEAE-Hec ($\Delta d = 0.1 \text{ \AA}$, $d_{\text{dry}} = 13.4 \text{ \AA}$, $d_{98\%r.h.} = 13.5 \text{ \AA}$) where no significant change in d-spacing is observed while for DEAE-Verm a steep increase ($\Delta d = 6.9 \text{ \AA}$, $d_{\text{dry}} = 13.4 \text{ \AA}$, $d_{98\%r.h.} = 20.3 \text{ \AA}$; Table S3) was found. Moreover, the d-spacing of dry DEAE-Verm corresponds to a monolayer coverage with $A_l/A_c \sim 1.2$, which suggests that there is no free volume in the interlayer space for DEAE-Verm available for adsorbing water without increasing the d-spacing. Contrariwise, for TRIS-Hec and DEAE-Hec A_l/A_c is 0.77 and 0.85, respectively. A_l/A_c less than 1 would suggest that there is free volume between the organo-cations in these organo-clays. Indeed, both TRIS-Hec and DEAE-Hec take up water at 98 % r.h. (2.1 mol and 0.9 mol water per mol interlayer cation, respectively as determined gravimetrically). This significant hydration by filling voids in the interlayer does not show up in a shift in d-spacing. Surprisingly, this type of "void"-hydration does not foster any further hydration with concomitant increase in d-spacing, while C4-Hec with a similar ratio ($A_l/A_c = 0.72$) in turn swells significantly ($\Delta d = 0.8 \text{ \AA}$).

In the same line, the extend of swelling for TMAEMA-Verm ($\Delta d = 6.3 \text{ \AA}$, $d_{\text{dry}} = 17.4 \text{ \AA}$, $d_{98\%r.h.} = 23.7 \text{ \AA}$) is more pronounced than for TMAEMA-Hec ($\Delta d = 2.8 \text{ \AA}$, $d_{\text{dry}} = 13.7 \text{ \AA}$, $d_{98\%r.h.} = 16.8 \text{ \AA}$). With this organo-cation for both clays, A_l/A_c is larger than 1 indicating that this cation exerts some steric pressure and that no voids should exist in the interlayer arrangement of both organo-clays. Nevertheless, despite the higher Coulomb attraction swelling of TMAEMA-Verm is much higher than for TMAEMA-Hec.

Independently of the hydrophilicity of the organo-cation, it seems that a dense surface coverage or inclined chains ($A_l/A_c \gtrsim 1$) are a sine qua non criterion for observing a significant degree of crystalline swelling of organo-clays. This is true for TMAEMA-Hec ($\Delta d = 2.8 \text{ \AA}$) and all organo-Verm samples ($\Delta d \geq 3.5 \text{ \AA}$). $A_l/A_c \gtrsim 1$ is, however, only a necessary but not yet a sufficient criterion to guarantee osmotic swelling into a gel when the clay is immersed into water (Figure 2). Rather, phenomenologically all organo-clays that spontaneously delaminate upon addition of water due to repulsive osmotic swelling are characterized by three common features that are met at the same time: $A_l/A_c \gtrsim 1$, Δd is

$\gtrsim 3.5 \text{ \AA}$ and is significantly more pronounced than for the non-swelling layer charge and furthermore, the maximum d-spacing achieved at 98 % r.h. is $d \gtrsim 17.5 \text{ \AA}$ (Table S3). A_l/A_c relates to the steric pressure generated by the bulkiness of the interlayer cation. Δd relates somehow to the hydrophilicity of the interlayer cation and potentially also to the increase in steric pressure upon hydration of the organo-cation. The maximum d-spacing observed determines the counter ion translational entropy. The latter is an essential ingredient for obtaining an increased repulsive interaction between adjacent silicate layers characterized by d-spacings above the threshold separation d^* .

While it appears impossible to predict combinations of interlayer cation and charge density of clay for which d^* will be achieved based on A_l/A_c alone, it can be rationalized applying a simple model, why the osmotic pressure between adjacent silicate layer reverses sign and becomes repulsive, once a threshold separation d^* is achieved (Figure 4): In this model a discrete distribution of charges is assumed, since the distance between isomorphously substituted structural ions that represent the source of charges in the clay layer is in the range of 5 to 10 \AA . The length at which two elementary charges interact with thermal energy $k_B T$ (Bijerum-length, $l_B = \frac{e^2}{4\pi\epsilon_0\epsilon k_B T}$) is roundabout 7 \AA in water, i.e. it is in the same order of magnitude. Permanent and discrete negative point charges are located in the middle of the lamellae and they are balanced by positive point charges in the interlayer space. In a strongly coupled state, which shall describe the dry clay and the initial stages of crystalline swelling best, the clay can be described by a single charge neutral correlation box (red box in Figure 4). Within this non-boundary condition box the charges are separated by a distance $d/2$.

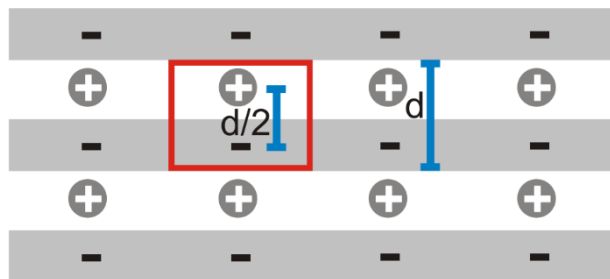


Figure 4. Simplified model of a strongly coupled state for a clay structure. Permanent and discrete negative point charges are located in the middle of the silicate layer and are balanced by positive point charges in the interlayer space. The red box (periodic boundary conditions neglected) can be described as a charge neutral correlation box with a distance $d/2$ of the charges.

In this model, the attractive Coulomb energy for a charge located on a silicate layer is given by the expression

$$E_{el} = -\frac{e^2}{4\pi\epsilon_0\epsilon d/2} \quad (1)$$

Using the Bijerum-length ($l_B = \frac{e^2}{4\pi\epsilon_0\epsilon k_B T}$) it follows:

$$E_{el} = -k_B T l_B \frac{1}{d/2} \quad (2)$$

Repulsive electrostatic interactions (ion-ion or layer-layer) can be neglected in a strongly coupled state. The counter ion translational entropy $S = k_B \ln(d/2)$ contributes to the free energy according to $-ST$, resulting in a repulsive energy contribution:

$$E_S = -k_B T \ln(d/2) \quad (3)$$

Ergebnisse

The osmotic pressure is derived according to $\Pi = -\sigma \frac{\delta E}{\delta d}$ leading to be

$$\Pi_{el} = -2\sigma k_B T l_B \frac{1}{d^2} \quad (4)$$

$$\Pi_S = \sigma k_B T \frac{1}{d} \quad (5)$$

The total osmotic pressure $\Pi_{total} = \Pi_S + \Pi_{el}$ is

$$\Pi_{total} = \frac{\sigma k_B T}{d} (1 - 2 l_B \frac{1}{d}) \quad (6)$$

$$\Pi_{total} \sim (1 - 2 l_B \frac{1}{d}) \quad (7)$$

At d-spacings $d > 2l_B$ (14 Å) the system becomes repulsive ($\Pi > 0$) and consequently $d^* = 2l_B$. The crystal chemical meaning of this approximation is, that upon exceeding the critical d-spacing d^* the system becomes repulsive and repulsive osmotic swelling can set in.

The model predicts d^* to be insensitive to the layer charge. The model, however, neglects the *Madelung* contribution inherent to a periodic 1-dimensional crystal which will proportionally increase the Coulomb energy that of course is strongly dependent on the layer charge. Taking this into account in a qualitative manner would suggest that clays with lower layer charge have a somewhat lower threshold separation. This might explain why Na-Hec delaminates in water contrary to Na-Verm. Neglecting the influence of confined space on dielectric constants of water and neglecting like charge repulsions represent some other serious simplifications. The net electrostatic interaction is, however, expected to be attractive.⁴³ After all, the model may therefore be regarded as a zeroth approximation. Qualitatively, it helps explaining the repulsive osmotic swelling of organo-vermiculites, while the absolute value of d^* may be questionable.

However, interestingly and in line with our discussion, for layered α -Zr-Phosphate exfoliation by intercalation of tetrabutylammonium was reported only in case the monolayer coverage was exceeded⁴⁴ which basically corresponds to $A_l/A_c \gtrsim 1$. Moreover, it was reported by Sasaki et. al. that Ethylamine was sufficient to trigger osmotic swelling in layered $H_{0.8}[Ti_{1.2}Fe_{0.8}]O_4$, while no osmotic swelling was observed with the smaller Methylamine.⁴ Hence it was argued that a certain separation of adjacent layers to trigger osmotic swelling might be necessary.⁴

CONCLUSION AND OUTLOOK

While for Na-smectites an upper limit of the layer charge for repulsive osmotic swelling is well established, a consistent explanation for the osmotic swelling of n-butylammonium-vermiculites is lacking. It was not even known whether osmotic swelling of organo-vermiculites is a general phenomenon that can be extended to other organo-cations. We offer a simple explanation for the onset of osmotic swelling by means of entropic repulsion at a critical d-spacing d^* . Unfortunately, a rational choice of interlayer cations that expand the interlayer space beyond this critical d-spacing remains difficult. Phenomenologically, bulky organic but hydrophilic interlayer cations are required. But more precisely, two further criterions have to be met at the same time: First, a certain steric demand of the (hydrated) interlayer cations needs to be exerted as expressed by $A_l/A_c \gtrsim 1$. Second, the hydration (solvation) enthalpy of the interlayer ions needs to be negative enough to trigger a degree of swelling sufficient to separate the adjacent layers above the threshold value d^* .

Unfortunately, we so far failed to identify organo-cations that do the job for 2:1 layered silicates with a larger range of charge densities. This would be highly desirable for robust and utter delamination of natural clays like montmorillonites

that are known to suffer from charge heterogeneities. We will continue our screening in this direction.

ASSOCIATED CONTENT

Supporting Information. Layer Charge Determination, Organo-Clays: CHN-Analyis and EDX, Volume Fration of a Gel and Expected d-spacing, Crystalline Swelling of Clays: d-spacings.

AUTHOR INFORMATION

Corresponding Author

*Phone +49 921 55 2531; Fax +49 921 55 2788; e-mail Josef.Breu@uni-bayreuth.de

Notes

The authors declare no competing financial interest.

Funding Sources

This work was supported by the Deutsche Forschungsgemeinschaft (SFB 840) and by BYK Chemie GmbH. M.D. thanks Fonds der chemischen Industrie for a fellowship.

ACKNOWLEDGEMENTS

Bayerisches Geoinstitut is acknowledged for microprobe analysis and BAYCEER for ICP-OES measurements.

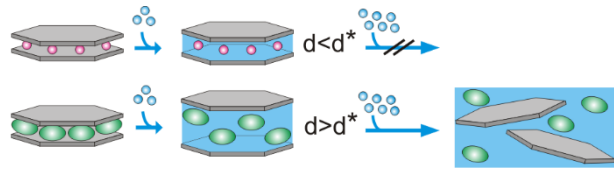
REFERENCES

- (1) Pauling, L.; The Structure of the Micas and Related Minerals. *Proc. Nat. Acad. Sci.* **1930**, *16*, 123-129.
- (2) Paineau, E.; Biannic, I.; Baravian, C.; Philippe, A. M.; Davidson, P.; Levitz, P.; Funari, S. S.; Rochas, C.; Michot, L. J.; Aqueous Suspensions of Natural Swelling Clay Minerals. 1. Structure and Electrostatic Interactions. *Langmuir* **2011**, *27*, 5562-5573.
- (3) Lagaly, G.; Ziesmer, S.; Colloid chemistry of clay minerals: the coagulation of montmorillonite dispersions. *Adv. Colloid Interface Sci.* **2003**, *100-102*, 105-128.
- (4) Geng, F.; Ma, R.; Ebina, Y.; Yamauchi, Y.; Miyamoto, N.; Sasaki, T.; Gigantic Swelling of Inorganic Layered Materials: A Bridge to Molecularly Thin Two-Dimensional Nanosheets. *J. Am. Chem. Soc.* **2014**, *136*, 5491-5500.
- (5) Maluangnont, T.; Matsuba, K.; Geng, F.; Ma, R.; Yamauchi, Y.; Sasaki, T.; Osmotic Swelling of Layered Compounds as a Route to Producing High-Quality Two-Dimensional Materials. A Comparative Study of Tetramethylammonium versus Tetrabutylammonium Cation in a Lepidocrocite-type Titanate. *Chem. Mater.* **2013**, *25*, 3137-3146.
- (6) Sasaki, T.; Watanabe, M.; Osmotic Swelling to Exfoliation. Exceptionally High Degrees of Hydration of a Layered Titanate. *J. Am. Chem. Soc.* **1998**, *120*, 4682-4689.
- (7) Gabriel, J. C.; Camerel, F.; Lemaire, B. J.; Desvaux, H.; Davidson, P.; Batail, P.; Swollen liquid-crystalline lamellar phase based on extended solid-like sheets. *Nature* **2001**, *413*, 504-508.
- (8) Meyer, J. C.; Geim, A. K.; Katsnelson, M. I.; Novoselov, K. S.; Booth, T. J.; Roth, S.; The structure of suspended graphene sheets. *Nature* **2007**, *446*, 60-63.
- (9) Novoselov, K. S.; Falko, V. I.; Colombo, L.; Gellert, P. R.; Schwab, M. G.; Kim, K.; A roadmap for graphene. *Nature* **2012**, *490*, 192-200.
- (10) Novoselov, K. S.; Geim, A. K.; Morozov, S. V.; Jiang, D.; Zhang, Y.; Dubonos, S. V.; Grigorieva, I. V.; Firsov, A. A.; Electric Field Effect in Atomically Thin Carbon Films. *Science* **2004**, *306*, 666.
- (11) Stöter, M.; Kunz, D. A.; Schmidt, M.; Hirsemann, D.; Kalo, H.; Putz, B.; Senker, J.; Breu, J.; Nanoplatelets of Sodium Hectorite Showing Aspect Ratios of ~20 000 and Superior Purity. *Langmuir* **2013**, *29*, 1280-1285.
- (12) Dozov, I.; Paineau, E.; Davidson, P.; Antonova, K.; Baravian, C.; Biannic, I.; Michot, L. J.; Electric-Field-Induced Perfect

Ergebnisse

- Anti-Nematic Order in Isotropic Aqueous Suspensions of a Natural Beidellite Clay. *J. Phys. Chem. B* **2011**, *115*, 7751-7765.
- (13) Michot, L. J.; Biannic, I.; Maddi, S.; Funari, S. S.; Baravian, C.; Levitz, P.; Davidson, P.; Liquid-crystalline aqueous clay suspensions. *Proc. Nat. Acad. Sci.* **2006**, *103*, 16101-16104.
- (14) Paineau, E.; Antonova, K.; Baravian, C.; Biannic, I.; Davidson, P.; Dozov, I.; Impérator-Clerc, M.; Levitz, P.; Madsen, A.; Meneau, F.; Michot, L. J.; Liquid-Crystalline Nematic Phase in Aqueous Suspensions of a Disk-Shaped Natural Beidellite Clay. *J. Phys. Chem. B* **2009**, *113*, 15858-15869.
- (15) Hemmen, H.; Ringdal, N. I.; De Azevedo, E. N.; Engelsberg, M.; Hansen, E. L.; Méheust, Y.; Fossum, J. O.; Knudsen, K. D. The Isotropic-Nematic Interface in Suspensions of Na-Fluorohectorite Synthetic Clay. *Langmuir* **2009**, *25*, 12507-12515.
- (16) Miyamoto, N.; Iijima, H.; Ohkubo, H.; Yamauchi, Y.; Liquid crystal phases in the aqueous colloids of size-controlled fluorinated layered clay mineral nanosheets. *Chem. Commun.* **2010**, *46*, 4166-4168.
- (17) Nakato, T.; Miyamoto, N.; Liquid Crystalline Behavior and Related Properties of Colloidal Systems of Inorganic Oxide Nanosheets. *Materials* **2009**, *2*, 1734.
- (18) Gholamipour-Shirazi, A.; Carvalho, M. S.; Huila, M. F. G.; Araki, K.; Dommersnes, P.; Fossum, J. O.; Transition from glass- to gel-like states in clay at a liquid interface. *Sci. Rep.* **2016**, *6*, 37239.
- (19) Fossum, J. O.; Flow of clays. *Eur. Phys. J. Spec. Top.* **2012**, *204*, 41-56.
- (20) Hansen, E. L.; Jabbari-Farouji, S.; Mauroy, H.; Plivelic, T. S.; Bonn, D.; Fossum, J. O.; Orientational order in a glass of charged platelets with a concentration gradient. *Soft Matter* **2013**, *9*, 9999-10004.
- (21) Jasmund, K.; Lagaly, G. *Tonminerale und Tone: Struktur, Eigenschaften, Anwendungen und Einsatz in Industrie und Umwelt*; Steinkopff: Darmstadt, **1993**. p. 110.
- (22) Ferrage, E.; Lanson, B.; Sakharov, B. A.; Geoffroy, N.; Jacquot, E.; Drits, V. A.; Investigation of dioctahedral smectite hydration properties by modeling of X-ray diffraction profiles: Influence of layer charge and charge location. *Am. Mineral.* **2007**, *92*, 1731-1743.
- (23) Marry, V.; Turq, P.; Microscopic Simulations of Interlayer Structure and Dynamics in Bihydrated Heteroionic Montmorillonites. *J. Phys. Chem. B* **2003**, *107*, 1832-1839.
- (24) Marry, V.; Turq, P.; Cartailler, T.; Levesque, D. Microscopic simulation of structure and dynamics of water and counterions in a monohydrated montmorillonite. *J. Chem. Phys.* **2002**, *117*, 3454-3463.
- (25) Ferrage, E.; Lanson, B.; Malikova, N.; Plançon, A.; Sakharov, B. A.; Drits, V. A.; New Insights on the Distribution of Interlayer Water in Bi-Hydrated Smectite from X-ray Diffraction Profile Modeling of 00l Reflections. *Chem. Mater.* **2005**, *17*, 3499-3512.
- (26) Martins, M. L.; Gates, W. P.; Michot, L.; Ferrage, E.; Marry, V.; Bordallo, H. N.; Neutron scattering, a powerful tool to study clay minerals. *Appl. Clay Sci.* **2014**, *96*, 22-35.
- (27) Dazas, B.; Ferrage, E.; Delville, A.; Lanson, B.; Interlayer structure model of tri-hydrated low-charge smectite by X-ray diffraction and Monte Carlo modeling in the Grand Canonical ensemble. *Am. Mineral.* **2014**, *99*, 1724-1735.
- (28) Rausell-Colom, J. A.; Saez-Anuon, J.; Pons, C. H.; Vermiculite Gelation: Structural and Textural Evolution. *Clay Miner.* **1988**, *24*, 459-478.
- (29) Rausell-Colom, J. A.; Salvador, P. S.; Complexes Vermiculite-Aminoacides. *Clay Miner.* **1971**, *9*, 139-149.
- (30) Braganza, L. F.; Crawford, R. J.; Smalley, M. V.; Thomas, R. K.; Swelling of n-Butylammonium Vermiculite in Water. *Clays Clay Miner.* **1990**, *38*, 90-96.
- (31) Smalley, M. V.; Electrical Theory of Clay Swelling. *Langmuir* **1994**, *10*, 2884-2891.
- (32) Smalley, M. V.; Thomas, R. K.; Braganza, L. F.; Matsuo, T.; Effect of hydrostatic pressure on the swelling of n-butylammonium vermiculite. *Clays Clay Miner.* **1989**, *37*, 474-478.
- (33) Garret, W. G.; Walker, G. F.; Swelling of some vermiculite-organic complexes in water. *Clays Clay Miner.* **1960**, *9*, 557-567.
- (34) Walker, G. F.; Macroscopic Swelling of Vermiculite Crystals in Water. *Nature* **1960**, *187*, 312-313.
- (35) Daab, M.; Rosenfeldt, S.; Kalo, H.; Stöter, M.; Bojer, B.; Siegel, R.; Förster, S.; Senker, J.; Breu, J.; Two-Step Delamination of Highly Charged, Vermiculite-like Layered Silicates via Ordered Heterostructures. *Langmuir* **2017**, *33*, 4816-4822.
- (36) Lagaly, G.; Water and Solvents on Surfaces Bristling with Alkyl Chains. In *Interactions of Water in Ionic and Nonionic Hydrates*, Kleeberg, H., Ed.; Springer Berlin Heidelberg, **1987**, pp. 229-240.
- (37) Rosenfeldt, S.; Stöter, M.; Schlenk, M.; Martin, T.; Albuquerque, R. Q.; Förster, S.; Breu, J.; In-Depth Insights into the Key Steps of Delamination of Charged 2D Nanomaterials. *Langmuir* **2016**, *32*, 10582-10588.
- (38) Mermut, A. R.; Lagaly, G.; Baseline Studies of the Clay Minerals Society Source Clays: Layer-charge Determination and Characteristics of those Minerals Containing 2:1 Layers. *Clays Clay Miner.* **2001**, *49*, 393-397.
- (39) Lagaly, G.; Layer charge heterogeneity in vermiculites. *Clays Clay Miner.* **1982**, *30*, 215-222.
- (40) Kalo, H.; Milius, W.; Breu, J.; Single crystal structure refinement of one- and two-layer hydrates of sodium fluorohectorite. *RSC Adv.* **2012**, *2*, 8452-8459.
- (41) Schmidt, C. U.; Lagaly, G.; Surface modification of bentonites: I. Betaine montmorillonites and their rheological and colloidal properties. *Clay Miner.* **1999**, *34*, 447-458.
- (42) Swain, M.; chemicalize.org. *J. Chem. Inf. Model.* **2012**, *52*, 613-615.
- (43) Pellenq, R. J. M.; Caillol, J. M.; Delville, A.; Electrostatic Attraction between Two Charged Surfaces: A (N,V,T) Monte Carlo Simulation. *J. Phys. Chem. B* **1997**, *101*, 8584-8594.
- (44) Kim, H.-N.; Keller, S. W.; Mallouk, T. E.; Schmitt, J.; Decher, G.; Characterization of Zirconium Phosphate/Polycation Thin Films Grown by Sequential Adsorption Reactions. *Chem. Mater.* **1997**, *9*, 1414-1421.

SYNOPSIS TOC. A simple explanation for the onset of osmotic swelling in highly charged organo-clays is offered. At a critical d-spacing entropic repulsion sets in. This d-spacing is achieved by the swelling of bulky organic but hydrophilic molecules at a small enough charge equivalent area (high enough charge density) of the clay.



Ergebnisse

6.2.1. Supporting Information

The Onset of Osmotic Swelling in Highly Charged Clay Minerals

Matthias Daab,[†] Natalie J. Eichstaedt,[†] Christoph Habel,[†] Sabine Rosenfeldt,[†] Hussein Kalo,[‡] Hubert Schießling,[‡] Stephan Förster[§] and Josef Breu*[†]

[†]Bavarian Polymerinstitute and Department of Chemistry, University of Bayreuth, D-95440 Bayreuth, Germany

[‡]BYK Chemie GmbH, D-85368 Moosburg, Germany

[§]Forschungszentrum Jülich, Institute of Complex Systems (ICS-1), D-52425 Jülich, Germany

Supporting Information

Content:

1. Supporting Data

- Layer Charge Determination
- Organo-Clays: CHN-Analysis and EDX
- Volume Fraction of a Gel
- Crystalline Swelling of Clays: d-spacings

2. Supporting References

Supporting Data

Layer Charge Determination.

Table S1: Layer charges corresponding to dense packings of mono- or bilayers for n-alkylammonium chains ($C_nH_{2n+1}NH_3^+$) of different length n. The layer charge that results in a dense monolayer or a dense bilayer arrangement is given as follows, assuming a typical a,b area of 47.6 \AA^2 .¹

chain lenght n	monolayer	bilayer
	[p.f.u.]	[p.f.u.]
5	0.56	1.12
6	0.50	0.99
7	0.44	0.89
8	0.40	0.80
9	0.37	0.73
10	0.34	0.67
11	0.31	0.62
12	0.29	0.58

Ergebnisse

Organo-Clays: CHN-analysis and EDX.

The completeness of exchange was determined by CHN- and by EDX-analysis for the remaining sodium-content. The carbon content was converted to interlayer cation content. The amount of organo-cations per gram clay is calculated from the determined wt% of carbon in the organo-clay; the amount of carbon atoms per molecule (x_c) and the molar mass of carbon:

$$CEC_{organo-clay} = \frac{wt\% C}{x_c \cdot 12.011 g/mol}$$

$CEC_{organo-clay}$ was compared to the expected maximum organo-content in mval / 100 g ($CEC_{organo-max.}$) as calculated from the amount of exchangeable Na^+ -ions n per 100 g. The amount n is given in mval as determined by the BaCl_2 -method, $n_{Hec} = 129$ mval (per 100 g) and $n_{Verm} = 185$ mval (per 100 g). Furthermore, the molar masses M of Na and the organic cations are needed.

$$CEC_{organo-max.} = \frac{n}{100 g - M(\text{Na}) \cdot n + M(\text{organocation}) \cdot n}$$

The completeness of organo-exchange is calculated from the ratio $CEC_{organo-clay} / CEC_{organo-max.}$ and is listed in Table S2.

The remaining Na-content was independently estimated by EDX and is calculated from the Na/Si-ratio.

Table S2: Results of the characterization of the obtained organo-clays by CHN-analysis and EDX.

	Hec		Verm	
	Organic content	Na-content	Organic content	Na-content
	(% of $CEC_{organo-max.}$)	(% CEC)	(% of $CEC_{organo-max.}$)	(% CEC)
C4	101	~0	100	~3
TRIS	100	~0	100	~2
DEAE	100	~0	93	~4
TMAEMA	92	~8	91	~12

Volume Fraction of a Gel and Expected d-spacing.

First of all, the weight-fraction of the clay lamellae in the dry clay sample is calculated as follows:

$$wt\%_{lamellae} = 100\% - wt\%_{interlayer\ ions}$$

The weight fraction of the interlayer ions is calculated by the ion content as determined by CHN for all organo-silicates and by the Ba-CEC for Na-Hec and Na-Verm.

The volume fraction ϕ is calculated using the density of the lamellae (2.7 g cm^{-3}) and water (1.0 g cm^{-3}):

$$\phi = \frac{wt\%_{lamellae} \cdot m_{clay} / \rho_{lamellae}}{wt\%_{lamellae} \cdot m_{clay} / \rho_{lamellae} + m_{water} / \rho_{water}}$$

The expected d-spacing is calculated using the thickness ($t = 9.6 \text{ \AA}$) of a clay lamella:

$$d = \frac{t}{\phi}$$

Crystalline Swelling of the Clays: d-spacings.

Table S3: d-spacings^{a)} of the clays (dry and 98 % r.h.) and Δd

	Hec			Verm		
	$d_{dry} [\text{\AA}]$	$d_{98\% \text{ r.h.}} [\text{\AA}]$	$\Delta d [\text{\AA}]$	$d_{dry} [\text{\AA}]$	$d_{98\% \text{ r.h.}} [\text{\AA}]$	$\Delta d [\text{\AA}]$
Na	9.7	15.1	5.4	9.7	15.1	5.4
C4	13.3	14.1	0.8	13.8	19.7	5.9
TRIS	13.7	14.0	0.3	14.0	17.5	3.5
DEAE	13.4	13.5	0.1	13.4	20.3	6.9
TMAEMA	14.0	16.8	2.8	17.4	23.7	6.3

a) Where more than one basal spacing was observed, the larger value is listed.

Supporting References

- (1) Mermut, A. R.; Lagaly, G. Baseline Studies of the Clay Minerals Society Source Clays: Layer-charge Determination and Characteristics of those Minerals Containing 2:1 Layers. *Clays Clay Miner.* 2001, 49, 393-397.

Ergebnisse

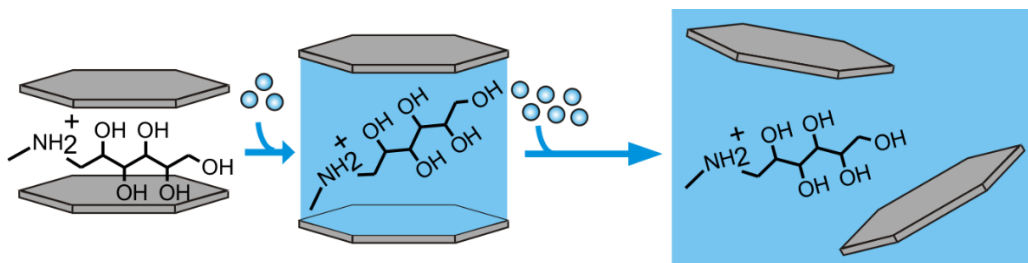
6.3. Ladungsdichte-übergreifende Delaminierung

Matthias Daab,[†] Natalie J. Eichstaedt,[†] Andreas Edenthaler,[†] Sabine Rosenfeldt[†] and Josef Breu^{†*}

Layer Charge Robust Delamination of Organo-Clays

to be submitted

[†]Bavarian Polymerinstitute and Department of Chemistry, University of Bayreuth, D-95440 Bayreuth, Germany



Darstellung des Eigenanteils:

Das Konzept der Ladungsdichte-übergreifenden Delaminierung wurde von mir erarbeitet. Das Manuskript wurde von mir verfasst und wurde mit Prof. Dr. Josef Breu zur Einreichung überarbeitet. Von mir wurden die Auswertungen und Interpretationen durchgeführt und Meglumin über einen weiten Schichtladungsbereich getestet. Die meisten Messungen wurden unter meiner Anleitung von Natalie Eichstaedt im Rahmen ihrer Bachelorarbeit durchgeführt, die Restlichen von mir. Andreas Edenthaler trug zur wissenschaftlichen Diskussion bei. Sabine Rosenfeldt half bei SAXS-Messungen. Textauszüge des Manuskriptes habe ich für eine Patentanmeldung vor dem Einreichen dieser Arbeit zur Verfügung gestellt. Mein Eigenanteil beträgt ca. 80 %.

Veröffentlichung nach Fertigstellung dieser Arbeit:

RSC Adv. 2018, 8, 28797-28803.

Published by The Royal Society of Chemistry.

<http://dx.doi.org/10.1039/C8RA05318A>

Layer Charge Robust Delamination of Organo-Clays

Matthias Daab,[†] Natalie J. Eichstaedt,[†] Andreas Edenharter,[†] Sabine Rosenfeldt[†] and Josef Breu^{†,*}

[†]Bavarian Polymerinstitute and Department of Chemistry, University of Bayreuth, D-95440 Bayreuth, Germany

ABSTRACT: To date delamination of organo-clays is restricted to highly charged, vermiculite-type layered silicates (e.g. n-butylammonium vermiculites). An extended screening, which was guided by previous findings, now identified organo-cations that allowed for extending the process to charge densities in the regime of low-charged smectites. Applying protonated amino-sugars like N-Methyl-D-Glucamine (Meglumine) as an interlayer ion ensures robust delamination of 2:1 layered silicates via repulsive osmotic swelling in water over a wide range of charge densities spanning from smectites (layer charge $x \sim 0.3$ charges per formula unit $\text{Si}_4\text{O}_{10}\text{F}_2$, p.f.u.) to vermiculites ($x \sim 0.7$ p.f.u.). Key is a combination of sufficiently large charge equivalent area along with a significant hydrophilicity of Meglumine that leads to swelling above a threshold d-spacing of $\gtrsim 17.5 \text{ \AA}$ in moist air (98 % r.h.), critically weakening electrostatic attraction. Moreover, Meglumine renders delamination tolerant to charge heterogeneities.

INTRODUCTION

For artificial nacre materials¹⁻³ or high-end gas-barriers,⁴⁻⁶ highly-filled nanocomposites of well oriented nanosheets perform best. Self-assembly into such textured films requires strict control of layer thickness. The same applies to the fabrication of heterostructures.⁷⁻¹⁰ For charged 2-dimensional (2D) materials this kind of control of delamination is feasible via osmotic swelling.¹¹⁻¹³ This type of thermodynamically favoured disintegration of a 1D-crystalline stack of layers leads to nanosheets of structure-inherent thickness. Osmotic swelling is reported for 2D-materials of different electronic¹⁴⁻¹⁶ and magnetic¹⁷⁻²⁰ properties like clay minerals,²¹⁻²⁵ lepidocrocite-type titanates²⁶⁻²⁸ or layered antimony phosphates.²⁹ During osmotic swelling the lateral extension of the nanosheets is inherited from the lateral dimension of the parent material. Thus the aspect ratio α (ratio of lateral dimensions to height) of the resulting nanosheets is maximized, which is particular advantageous for gas barrier applications where permeability is expected to decrease by α^2 .³⁰ Unfortunately, the viability of osmotic swelling is highly sensitive to the charge density of the layered material. For instance, for Na-Hectorite ($\text{Na}_{0.5}^{in-ter.}[\text{Mg}_{2.5}\text{Li}_{0.5}]^{oct.}<\text{Si}_4>^{tetr.}\text{O}_{10}\text{F}_2$, Na-Hec) superb charge homogeneity has to be assured by a melt synthesis being followed by a lengthy high temperature annealing.^{12, 31} Only then a clay is obtained that spontaneously and utterly delaminates upon immersion into water delivering high aspect ratio nanosheets. This filler in turn warrants superior gas barrier properties of nanocomposites.³² Even slight variations of the charge density will lead to domains with a charge above the established upper limit ($x > 0.55$ per formula unit $\text{Si}_4\text{O}_{10}\text{F}_2$, p.f.u.)³³ for osmotic

swelling and these domains might pin the stacks together by the strong Coulomb interactions.¹² Therefore, melt-synthesized Na-Hectorites that have not been homogenized by annealing do not delaminate completely.^{31, 34} More recently and despite the even stronger Coulomb-attraction, we could show that more highly charged vermiculite-type clays (Na-Verm) can be utterly delaminated after ion-exchange with selected bulky and hydrophilic organo-cations.³⁵ Besides the organo-cation being sufficiently hydrophilic, a threshold separation has to be achieved at which repulsive interactions critically dominate over the Coulomb attraction. To accomplish that separation, the ratio of charge equivalent area of the interlayer cation (A_I , area that is occupied by a flat lying cation) and the charge equivalent area of the clay (A_C , area per charge as calculated by the charge density) A_I/A_C should be $\gtrsim 1$, to yield a sufficient steric demand upon hydration. Unfortunately, all organo-cations that were tested so far only delaminate highly charged vermiculites but failed to osmotically delaminate low charged, smectite-type clays like Na-Hec. Organo-cations that do the job for a broad range of charge densities would, however, be highly desirable in the light of charge heterogeneities observed for natural smectites like montmorillonite,^{36,37} for natural vermiculites, or for non-annealed synthetic Na-Hectorite. Therefore, we extended and intensified our screening for a charge robust delamination agent. And in this work we introduce two ammonium-sugars that are capable to trigger osmotic swelling for charge densities ranging from smectite-type clays ($x \sim 0.3$ p.f.u.) all the way to vermiculite-type clays ($x \sim 0.7$ p.f.u.) and that moreover are tolerant to heterogeneities in charge density.

Ergebnisse

EXPERIMENTAL

Synthesis and Characterization of the Clays. A highly charged Na-fluorohectorite $\text{Na}_{0.75}\text{Mg}_{2.25}\text{Li}_{0.75}\text{Si}_4\text{O}_{10}\text{F}_2$ with a nominal charge density in the range of vermiculites (Verm) and a medium charged Na-fluorohectorite $\text{Na}_{0.5}\text{Mg}_{2.5}\text{Li}_{0.5}\text{Si}_4\text{O}_{10}\text{F}_2$ (Hec) with a nominal charge density in the range of smectites were prepared by melt synthesis according to a published procedure followed by annealing (6 weeks, 1045 °C) to improve charge homogeneity and phase purity.³¹ For the as synthesized Hectorite of the nominal composition $\text{Na}_{0.5}\text{Mg}_{2.5}\text{Li}_{0.5}\text{Si}_4\text{O}_{10}\text{F}_2$ the annealing step after melt synthesis was left out and it was washed with Na_4EDTA (0.5 M, 50 mL per 1 g of Hec_{pri}) six times at 60 °C for 48 h per washing cycle and was washed till pH = 6.5 afterwards using Millipore-water, this procedure was repeated one times in order to get rid of soluble sidephases to yield the sample Hec_{pri}. The synthesis is carried out in gas tight molybdenum crucibles. The educts NaF (99.995%, Alfa Aesar), LiF (>99.9%, ChemPur), MgF_2 (>99.9%, ChemPur), MgO (99.95%, Alfa Aesar) and SiO_2 (Merck, fine granular quarz, purum) are mixed according to the nominal composition. The crucible was ramped to 1750 °C (15 °C/min), held at this temperature for 70 min, cooled to 1300 °C (55 °C/min) and then to 1050 °C (10 °C/min). Finally, it was quenched by switching of the power. Synthesis of charge reduced clays: 5 g of Hec were exchanged 7 times with 400 mL of 2 M MgCl_2 -solution. The resulting Mg-exchanged Hectorite was washed with water till chloride-test (with AgNO_3) of the supernatant solution was negative. The suspension was dried at 80°C. The dried powder was heated at 250°C for 24 h for charge reduction (obtained sample: LCR1).³⁸ 50% of the LCR1 sample were again exchanged 7 times with 400 mL of 2 M MgCl_2 -solution. The resulting Mg-exchanged Hectorite was washed with water till chloride-test of the supernatant solution was negative. The suspension was dried at 80°C. The dried powder was heated at 250°C for 24 h for charge reduction (obtained sample: LCR2). The cation exchange capacity was determined according to DIN ISO 11260 using BaCl_2 and the layer charge was determined according to Lagaly.^{39,40}

Powder X-ray Diffraction. Powder X-ray diffraction (PXRD) patterns of as-synthesized clays were recorded on a STOE Stadi P powder diffractometer using $\text{Cu K}\alpha_1$ radiation. The samples were placed in a glass capillary. Prior to measurement samples were equilibrated for one week over saturated K_2CO_3 -solution (43 % relative humidity, r.h.) to obtain the one water layer hydrate. After equilibration, the capillaries were sealed. All other PXRD were measured with textured samples in Bragg-Brentano geometry on a PANalytical X'pert Pro equipped with an X'Celerator Scientific RTMS detector ($\text{Cu K}\alpha$ radiation). PXRD patterns at fixed relative humidities were recorded in a temperature-humidity chamber (Anton Paar temperature humidity chamber driven by a VTI corp. RH-200 humidity generator) mounted on the PANalytical Xpert Pro. Dry samples were obtained by drying at 110°C under vacuum for 24 h and PXRDs of the hot samples were measured within 2 min each after removal from the vacuum furnace.

Microprobe Analysis. The chemical composition of Hec and Verm was determined by wavelength dispersive X-ray spectroscopy on single crystals with flat lying surfaces on a carbon tape using an electron microprobe (Jeol

JXA-8200, Bayerisches Geoinstitut, Bayreuth). The settings were 15 kV acceleration voltage, 15 nA initial beam current, a beam spot diameter of 10 μm, 10 s counting time at the peak position and 5 s counting time at each side of the peak.

Inductive-coupled plasma atomic emission spectroscopy (ICP-OES). The lithium and magnesium content of Hec and Verm was determined by ICP-OES. Samples of about 20 mg of dry clay were weighed into clean Teflon flasks of 15 mL volume. After addition of 1.5 mL 30 wt. % HCl (Merck), 0.5 mL of 85 wt. % H_3PO_4 (Merck), 0.5 mL 65 wt. % HNO_3 (Merck) and 1 mL of 48 wt. % HBF_4 (Merck) the sample was digested in a MLS 1200 Mega microwave digestion apparatus for 6.5 min and heated at 600W (MLS GmbH, Mikrowellen-Labor-Systeme, Leutkirch, Germany). The closed sample container was cooled to room temperature and the clear solution was diluted to 100 mL in a volumetric flask and analyzed on Vista-PRO radial spectrometer.

Cation-exchange with Meglumine. 200 mg of the dry, pristine clays were suspended in 50 mL of a 1 M solution of N-Methyl-D-Glucamine (Meglumine, in its protonated form, pH = 7, > 125-fold excess of the CEC, delamination is prevented by the high ionic strength). The procedure was repeated 5 times. Finally, the obtained organo-clays were washed free of chloride-ions (AgNO_3 -test) with Millipore-water. Gels were concentrated by centrifugation between the washing cycles. The organo-clays were finally washed one times with acetone and dried at 60°C.

CHN-Analysis. A PerkinElmer 2400 CHN equipped with a combustion tube filled with tungsten(VI)-oxide-granules was used at a combustion temperature of 1050 °C. Samples were dried at 110 °C and vacuum for 24 h and stored in a glovebox prior to measurement.

Scanning Electron Microscopy and Energy Dispersive X-ray Spectroscopy (REM-EDX). REM-EDX was measured on a Zeiss 1530 with a EDX INCA 400 unit (Oxford). Samples were prepared on a carbon tape and sputtered with 10 nm carbon.

Small angle X-ray scattering (SAXS). SAXS data were measured using a “Double Ganesha AIR” system (SAXSLAB, Denmark). The X-ray source of this laboratory-based system is a rotating anode (copper, MicroMax 007HF, Rigaku Corporation, Japan) providing a micro-focused beam. The data are recorded by a position sensitive detector (PILATUS 300K, Dectris). Samples were prepared by adding a defined amount of millipore-water to the dry organo-clay. After equilibration for one week SAXS-patterns were recorded in 1 mm glass capillaries.

Atomic force microscopy (AFM). AFM was done in tapping mode using a Dimension 3100 NanoScope IV-unit equipped with OTESPA-R3 (Bruker) silicon tips. Samples were prepared by dropping a very dilute aqueous dispersion (5 mg/L) in millipore water onto silicon wafers.

Ergebnisse

RESULTS AND DISCUSSION

Synthesis and Characterization of the Clays.

Clays with layer charges in the range $0.75 > x > 0.3$ p.f.u. have been synthesized. Highly charged Verm ($\text{Na}_{0.75}^{inter}[\text{Mg}_{2.25}\text{Li}_{0.25}]^{oct}<\text{Si}_4>^{tet}\text{O}_{10}\text{F}_2$ ($x = 0.75$ p.f.u. nominally) and medium charged Hec ($\text{Na}_{0.5}^{inter}[\text{Mg}_{2.5}\text{Li}_{0.5}]^{oct}<\text{Si}_4>^{tet}\text{O}_{10}\text{F}_2$ ($x = 0.5$ p.f.u. nominally)) are directly accessible via melt synthesis. Both were homogenized post-synthesis by long term-annealing in a gas tight crucible to prevent loss of volatile fluorides at elevated temperatures.^{31, 35} Their analysis is recapitulated briefly. As reported before, PXRDs (Fig. S1) indicate a crystalline hydrate for both clays with one layer of water molecules in the interlayer space at 43 % relative humidity (r.h.) ($d_{001} = 12.5 \text{ \AA}$).⁴¹ The patterns can be indexed in C2/m (No. 12) and the diffractograms can be completely indexed, least squares refined lattice parameters for Verm are $a = 5.26(1) \text{ \AA}$, $b = 9.07(2) \text{ \AA}$, $c = 12.48(4) \text{ \AA}$, $\gamma = 95.22(4)^\circ$ and for Hec $a = 5.20(1) \text{ \AA}$, $b = 9.10(1) \text{ \AA}$, $c = 12.48(4) \text{ \AA}$, $\gamma = 95.44(4)^\circ$. The chemical composition was determined by microprobe analysis. Microprobe analysis is insensitive to Li. Therefore, the Mg/Li-ratio was derived from ICP-OES analysis by assuming a complete occupancy of the tetrahedral positions (Si = 4) and by normalizing stoichiometric coefficients of octahedral and interlayer cations to match the 22 negative charges of the anionic sublattice (O_{10}F_2). This way compositions of $\text{Na}_{0.71(4)}\text{Mg}_{2.28(4)}\text{Li}_{0.72(4)}\text{Si}_4\text{O}_{10}\text{F}_2$ and of $\text{Na}_{0.52(2)}\text{Mg}_{2.51(4)}\text{Li}_{0.46(2)}\text{Si}_4\text{O}_{10}\text{F}_2$ were obtained for annealed Verm and annealed Hec, respectively. Lower charged clays that are not directly accessible via melt synthesis,³⁸ were obtained by layer charge reduction (LCR) of annealed Hec by an anti-Hoffmann-Klemm-effect: In doing so, Hec is first ion exchanged with Mg^{2+} followed by annealing at 250°C whereupon octahedral Li^+ and interlayer Mg^{2+} exchange sites. With increasing incorporation of Mg^{2+} into the octahedral layer, concomitantly the permanent negative charge of the silicate layers is reduced.³⁸ These samples were named LCR1 and LCR2 corresponding to one and two cycles of charge reduction. Moreover, a pristine Na-hectorite that has not been homogenized by annealing was included as a reference (Hec_{pri}) (Fig. S2). The composition was determined as $\text{Na}_{0.55(1)}^{inter}[\text{Mg}_{2.48(2)}\text{Li}_{0.49(2)}]^{oct}<\text{Si}_4>^{tet}\text{O}_{10}\text{F}_2$. The cation exchange capacities (CEC) determined by the BaCl₂-method were found to be 185 meq/100 g for Verm, 129 meq/100 g for Hec, 103 meq/100g for LCR1, 75 meq/100 mg for LCR2 and 116 meq/100g for Hec_{pri}. Owing to side phases without cation exchange capability, the experimentally determined CEC of Hec_{pri} (116 meq/100 g) is significantly lower than of the annealed Hec (129 meq/100g). The layer charge density was determined experimentally by the method of Lagaly^{39, 40} where interlayer ions are exchanged with n-alkylammonium ($\text{C}_n\text{H}_{2n+1}\text{NH}_3^+$, Fig. 1). For these organo-cations the equivalent area per charge is known for a dense packing of either mono- ($d = 13.3 \text{ \AA}$, dotted line) or bilayers ($d = 17.6 \text{ \AA}$, dashed line). The onset of the transition of mono- to bilayer- or from bilayer to pseudo-trilayer arrangement with increasing chain length was converted into upper limits of charge densities (Tab. S1). For high charged Verm $n = 9$ represents the longest alkylammonium chain that is still capable to balance the charge density in a bilayer ($d = 17.6 \text{ \AA}$). Slightly increasing the equivalent area to $n = 10$ some pseudo-trilayers

have to be mixed in to warrant charge balance as evidenced by a shift of the d-spacing (Fig. 1 A) which indicates $0.67 \leq x \leq 0.73$ p.f.u.. In a similar way, for the lower charged clays, the charge densities were derived from the transition of mono- to bilayers. with limiting chain length of $n = 5$ (Hec, Fig. 1B), $n = 8$ (LCR1, Fig. 1C) and $n = 11$ (LCR2, Fig. 1D) corresponding to $0.50 \leq x \leq 0.56$ p.f.u., $0.37 \leq x \leq 0.40$ p.f.u. and $0.29 \leq x \leq 0.31$ p.f.u. for Hec, LCR1 and LCR2, respectively (Tab. S1). Interestingly, for LCR2 with $n = 12$ two maxima are observed indicating a certain degree of charge heterogeneity. Apparently, the charge reduction process does not happen in a perfectly homogeneous way. This fact has previously been documented by a broadening of micropore size distributions of microporous organically pillared silicates derived from charge reduced hectorites.⁴² Similarly to LCR2, for Hec_{pri} ($0.50 \leq x \leq 0.56$ p.f.u., Fig. 1E) charge heterogeneity is reflected by a non-uniform increase in d-spacing at longer chain length ($n = 10$) in comparison to Na-Hec (compare Fig. 1E and 1B). In particular, with $n = 10$ for Hec_{pri} d-spacings were observed that are significantly shifted to higher values as compared to Hec. This indicates that Hec_{pri} not only is more heterogeneous but also at least parts of the sample have a higher layer charge as compared to Hec. Please note, that this two phase behaviour of the layer charge density probably is inherent to the melt synthesis conditions and is therefore an intrinsic problem that might be solved by a layer charge robust delamination process: Pseudo-binary alkaline and earth alkaline silicate system show pronounced immiscibility regions⁴³ and the critical temperature might even increase upon addition of fluoride.^{34, 44}

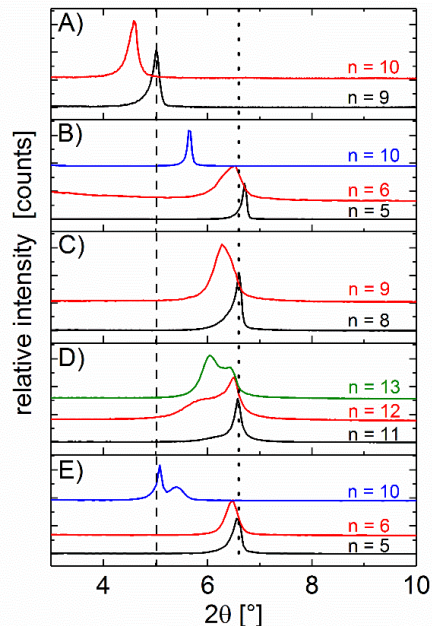


Fig. 1. Layer charge determination according to Lagaly. Interlayer ions are exchanged with n-alkylammonium ions of different chain length ($\text{C}_n\text{H}_{2n+1}\text{NH}_3^+$) for which the equivalent area per charge is known for a dense packing of either mono- ($d = 13.3 \text{ \AA}$, dotted line) or bilayers ($d = 17.6 \text{ \AA}$, dashed line). A) Verm, B) Hec, C) LCR1, D) LCR2, E) Hec_{pri}.

Ergebnisse

Swelling Behavior of Organo-Clays.

All clays were ion-exchanged with a hydrophilic but bulky ammonium-sugar (protonated N-Methyl-D-Glucamine, referred to as Meglumine). The expected Meglumine contents (in mmol/ 100 g) as calculated from the Ba-CEC (Tab. S2) are in fair agreement with Meglumine contents as determined by CHN analysis. Verm, Hec, LCR1, LCR2 and Hec_{pri} contained 138, 104, 90, 69 and 89 mmol Meglumine / 100 g, (expected: 140, 105, 87, 66 and 97 mmol / 100 g, respectively). The Na-content of Na-Verm, Na-Hec and Na-Hec_{pri} was below the detection limit of EDX (Fig. S3). The swelling of Meglumine-clays in humid air (98 % r.h.) is significant (Fig. 2). The d-spacings increase from 16.8 Å to 24.4 Å (Verm), 14.1 to 22.8 Å (Hec), 13.7 to 18.7 Å (LCR1), 13.4 to 18.2 Å (LCR2) and from 14.0 Å to 23.6 Å (Hec_{pri}). Furthermore, the significant increase in d-spacing upon swelling of $\Delta d = 7.6 \text{ Å}$ (Verm), 8.7 Å (Hec), 5.0 Å (LCR1), 4.8 Å (LCR2) and 9.6 Å (Hec_{pri}) may be attributed to the steric pressure of Meglumine upon hydration: With $j\text{mol}^{45} A_1 = 77 \text{ Å}^2$ can be estimated for a flat lying Meglumine cation (van-der-Waals extensions 13.5 Å x 5.7 Å). Consequently, even in case of low charged LCR2 ($x \sim 0.3$ p.f.u., corresponding to $A_C = 79 \text{ Å}^2/\text{charge}$) charge balance requires a densely packed monolayer of meglumine ($A_1/A_C \sim 1$). In the dry state no significant voids are available that could accommodate water molecules. Therefore, upon hydration of the hydrophilic interlayer cation at elevated r.h., expansion of the d-spacing is compulsory. The maximum d-spacings of Meglumine-clays after water uptake from humid air are $> 17.5 \text{ Å}$ for all clays of varying charge density. This d-spacing was suggested to be required for rendering the interaction of adjacent silicate layers repulsive once immersed into liquid water critically weakening electrostatic attraction.³⁵ Meglumine therefore is the first organo-cation that fulfills all necessary requirements postulated for allowing repulsive osmotic delamination of organo-clays. Most importantly, the requirements are met for a broad range of charge densities ranging from low-charge smectites all the way to vermiculite-type charges.³⁵

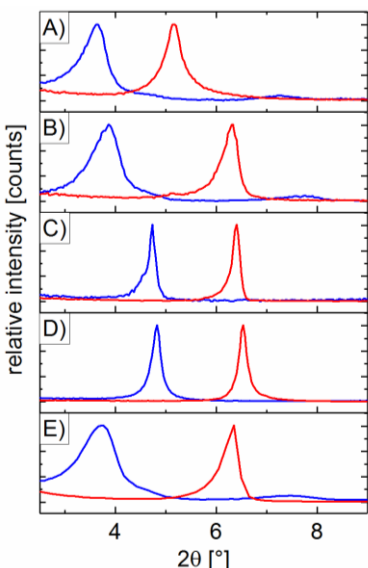


Fig. 2. PXRD of Meglumine-clays (dry, red trace and at 98 % r.h., blue trace). A) Verm, B) Hec, C) LCR1, D) LCR2, E) Hec_{pri}.

And indeed, repulsive osmotic swelling could be confirmed for all clays, also for low charged, smectite-type clays where other organo-cations investigated previously failed. When immersing Meglumine-clays into water homogeneous gels are obtained for all layer charges (Fig. 3, left).

Due to the repulsive nature adjacent silicate layers are separated to the maximum which is defined by the clay in water-volume fraction (ϕ , Fig. 3, right). Even at quite low clay content, the platelets cannot freely rotate because the typical lateral dimension ($> 10 \mu\text{m}$) are orders of magnitude larger than the separation of adjacent clay platelets. This separation can therefore be observed in the SAXS patterns as a series of $00l$ reflections with d-spacings of 140 Å (Verm, Fig. 3A, left), 132 Å (Hec, Fig. 3B, left), 133 Å (LCR1, Fig. 3C, left), 158 Å (LCR2, Fig. 3D, left) and 141 Å (Hec_{pri}, Fig. 3E, left) at concentrations of 5.9 vol% (Verm), 6.7 vol% (Hec), 6.3 vol% (LCR1), 7.1 vol% (LCR2) and 7.6 vol% (Hec_{pri}). (For details of conversion of wt% into vol% see Supporting Information). At clay contents > 3 vol%, the d-spacing is indirect proportional to ϕ .^{11,12} Taking into account the thickness of the silicate layer ($t = 9.6 \text{ Å}$) the separation of adjacent layers is given by $d = t / \phi$. For the given vol%, d-values of 163 Å (Verm), 143 Å (Hec), 152 Å (LCR1), 135 Å (LCR2) and 127 Å (Hec_{pri}) are expected, respectively. These values are in fair agreement with observed d-spacings for all clays. This is a first indication that the gels consist of domains of lamellar liquid crystals with a homogeneous separation of adjacent silicate layers.

This is furthermore corroborated by studying the increase of d-spacings of adjacent silicate layers upon increasing the water content (Fig. 3, right). A linear slope was found as expected according to $d = t / \phi$. The experimentally determined slopes are 8.4 Å (Verm, Fig. 3A, right), 8.8 Å (Hec, Fig. 3B, right), 8.9 Å (LCR1, Fig. 3C, right), 10.5 Å (LCR2, Fig. 3D, right) and 10.7 Å (Hec_{pri}, Fig. 3E, right) which is in good agreement with the expected value of 9.6 Å. Utter osmotic swelling to mono-phase gels is therefore concluded for all Meglumine-clays. Meglumine is not unique. Other bulky and hydrophilic ammonium-sugars like Glucosamine ($\sim 72 \text{ Å}^2$, $A_1/A_C = 0.9$ for LCR2) also have the potential of delaminating clays with broadly varying layer charge densities (Fig. S4).

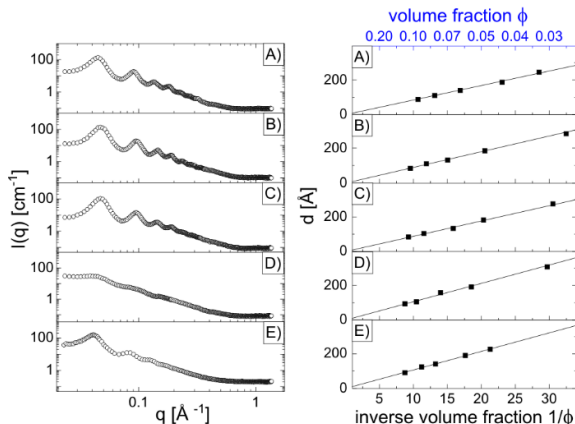


Fig. 3. Left: SAXS-pattern of Verm (A, 5.9 vol%), Hec (B, 6.7 vol%), LCR1 (C, 6.3 vol%), LCR2 (D, 7.1 vol%) and Hec_{pri} (E, 7.6 vol%). Right: The slope of d vs. $1/\phi$ is 8.4 Å (Verm, A), 8.8 Å (Hec, B), 8.9 Å (LCR1, C), 10.5 Å (LCR2, D) and 10.7 Å (Hec_{pri}, E).

Ergebnisse

Delamination of clays by Meglumine not only is robust in respect to a broad range of charge densities. Moreover, it proves tolerance to charge heterogeneities. This is important from a practical point of view since natural clays like montmorillonite suffer from pronounced charge density heterogeneity.

The results furthermore suggest, that repulsive osmotic delamination may be applied generally to charged two dimensional materials irrespective of their charge density.

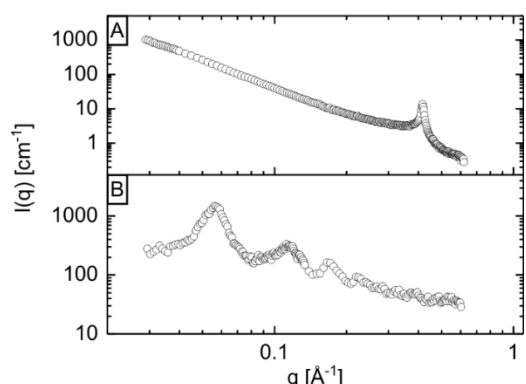


Fig. 4. SAXS-patterns. A) For Na-Hec_{pri} only a crystalline hydrate (two water layer hydrate, 15 Å) is found, while B) Na-Hec swells osmotically in water ($d = 112 \text{ \AA}$, 8.4 vol%, expected d -spacing: 114 Å).

Hec_{pri} represents a perfect test case for demonstrating the robustness and tolerance towards charge density variations for repulsive osmotic delamination with Meglumine. Contrary to Na-Hec ($d = 112 \text{ \AA}$, 8.4 vol%, expected d -spacing: 114 Å), Na-Hec_{pri} does not delaminate completely when immersed into liquid water despite a comparable layer charge density (Fig. 4). Moreover, swelling of Na-Hec_{pri} is limited to a crystalline hydrate (two water layer hydrate, 15 Å,⁴⁶⁻⁴⁹ Fig. 4A), although a minor fraction (< 5 wt% of total solid content) probably delaminates upon immersion in water, as indicated by the formation of a birefringent suspension between crossed polarizers (Fig. S5). Anyhow, while most of Hec_{pri} forms a non-birefringent sediment upon immersion in water its heterogeneity is emphasized by that partial delamination.

Cation exchange with Meglumine, however, allows quantitative delamination for both these hectorites (Fig. 3). Quite pleasing, this spares us the lengthy annealing procedure which so far was required to "activate" Na-Hec_{pri} for osmotic swelling.³¹ All diluted aqueous suspensions of Meglumine-clays show birefringence as expected for a lyotropic texture between crossed-polarizers at ~ 0.25 vol% due to the formation of a nematic sol (Fig. 5). Upon further dilution (~ 10⁻⁴ vol%) delamination into single platelets is evidenced by casting the then isotropic dispersions on a silicon wafer. With AFM only platelets with a height of ~ 1 nm were found in good agreement with the thickness of one silicate layer (9.6 Å).

CONCLUSION AND OUTLOOK

We have previously proposed that osmotic swelling requires, first, bulky interlayer cations ($A_I/A_C \gtrsim 1$) with, second, appreciable hygroscopy as expressed by significant swelling when going from 0 % to 98 % r.h. ($\Delta d \gtrsim 3.5 \text{ \AA}$). If then at 98 % r.h., third, a threshold separation ($d \gtrsim 17.5 \text{ \AA}$) is accomplished, repulsive delamination upon immersion in water sets in as electrostatic attraction is critically weakened.

Based on the above empirical recipe, we extended our screening to ammonium-sugars. These are considerably bulkier than for instance TRIS (Tris(hydroxymethyl)ammoniummethan, $A_I = 37 \text{ \AA}^2$) used before for vermiculites. At the same time their hydrophilicity is high due to a large number of OH-groups. This way, we were able to extend osmotic swelling of organo-clays into the regime of low-charged smectites.

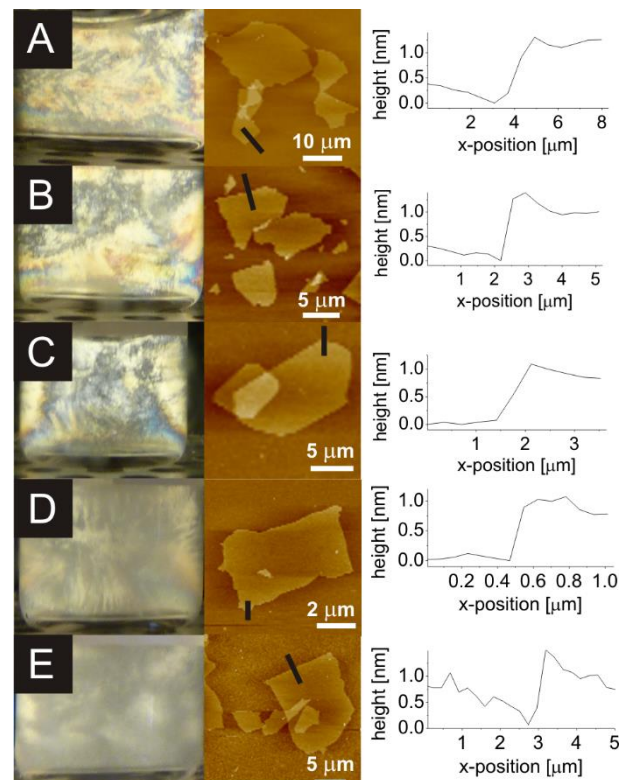


Fig 5. Upon dilution to ~ 0.25 vol% the aqueous Meglumine-clay suspensions show birefringence between crossed polarizers due to the formation of a nematic sol (left), in case isotropic dispersions of 10⁻⁴ vol% are dropped on a Si-wafer and dried, platelets are found by AFM (middle) with the height of a single-clay layer (right). A) Verm, B) Hec, C) LCR1, D) LCR2, E) Hec_{pri}.

ASSOCIATED CONTENT

Supporting Information. PXRD of Clay Minerals, Layer Charge Determination: Charge Density vs. Chain Length, Meglumine-clays: CHN and EDX, Volume Fraction of Gels (Calculation), Glucosamine-clays and Birefringence of Hec_{pri}-suspensions.

AUTHOR INFORMATION

Corresponding Author

*Phone +49 921 55 2531; Fax +49 921 55 2788; e-mail Josef.Breu@uni-bayreuth.de

Notes

The authors declare no competing financial interest.

Ergebnisse

Funding Sources

This work was supported by the Deutsche Forschungsgemeinschaft (SFB 840) and by BYK Chemie GmbH. M.D. thanks Fonds der chemischen Industrie for a fellowship.

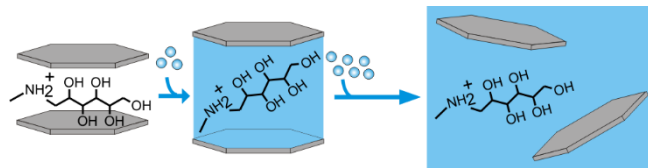
ACKNOWLEDGEMENTS

Bayerisches Geoinstitut is acknowledged for microprobe analysis and BAYCEER for ICP-OES measurements.

REFERENCES

- 1 Z. Tang, N. A. Kotov, S. Magonov, and B. Ozturk, *Nat. Mater.*, 2003, **2**, 413-418.
- 2 J. Wang, Q. Cheng, L. Lin and L. Jiang, *ACS Nano*, 2014, **8**, 2739-2745.
- 3 H.-B. Yao, Z.-H. Tan, H.-Y. Fang and S.-H. Yu, *Angew. Chem. Int. Ed.* **2010**, *49*, 10127-10131.
- 4 W. S. Jang, I. Rawson and J. C. Grunlan, *Thin Solid Films*, 2008, **516**, 4819-4825.
- 5 M. A. Priolo, D. Gamboa and J. C. Grunlan, *ACS Appl. Mater. Interfaces*, 2009, **2**, 312-320.
- 6 E. S. Tsurko, P. Feicht, F. Nehm, K. Ament, S. Rosenfeldt, I. Pietsch, K. Roschmann, H. Kalo and J. Breu, *Macromolecules*, 2017, **50**, 4344-4350.
- 7 K. S. Novoselov, D. Jiang, F. Schedin, T. J. Booth, V. V. Khotkevich, S. V. Morozov and A. K. Geim, *Proc. Nat. Acad. Sci.*, 2005, **102**, 10451-10453.
- 8 A. K. Geim and I. V. Grigorieva, *Nature*, 2013, **499**, 419-425.
- 9 D. Jariwala, T. J. Marks and M. C. Hersam, *Nat. Mater.*, 2017, **16**, 170-181.
- 10 B. V. Lotsch, *Ann. Rev. Mater. Res.*, 2015, **45**, 85-109.
- 11 L. J. Michot, I. Bihannic, S. Maddi, S. S. Funari, C. Baravian, P. Levitz and P. Davidson, *Proc. Nat. Acad. Sci.*, 2006, **103**, 16101-16104.
- 12 S. Rosenfeldt, M. Stöter, M. Schlenk, T. Martin, R. Q. Albuquerque, S. Förster and J. Breu, 2016, **32**, 10582-10588.
- 13 R. J. M. Pellenq, J. M. Caillol and A. Delville, *J. Phys. Chem. B*, 1997, **101**, 8584-8594.
- 14 N. Sakai, Y. Ebina, K. Takada and T. Sasaki, *J. Am. Chem. Soc.*, 2004, **126**, 5851-5858.
- 15 T. Sasaki and M. Watanabe, *J. Phys. Chem. B*, 1997, **101**, 10159-10161.
- 16 S. S. Kim, T. V. Khai, V. Kulish, Y.-H. Kim, H. G. Na, A. Katoch, M. Osada, P. Wu and H. W. Kim, *Chem. Mater.*, 2015, **27**, 4222-4228.
- 17 H. Hemmen, N. I. Ringdal, E. N. De Azevedo, M. Engelsberg, E. L. Hansen, Y. Méheust, J. O. Fossum and K. D. Knudsen, *Langmuir*, 2009, **25**, 12507-12515.
- 18 E. Paineau, I. Dozov, I. Bihannic, C. Baravian, M.-E. M. Krapf, A.-M. Philippe, S. Rouzière, L. J. Michot and P. Davidson, *ACS Appl. Mater. Interfaces*, 2012, **4**, 4296-4301.
- 19 X. Dong, M. Osada, H. Ueda, Y. Ebina, Y. Kotani, K. Ono, S. Ueda, K. Kobayashi, K. Takada and T. Sasaki, *Chem. Mater.*, 2009, **21**, 4366-4373.
- 20 M. Osada, Y. Ebina, K. Fukuda, K. Ono, K. Takada, K. Yamaura, E. Takayama-Muromachi and T. Sasaki, *Phys. Rev. B*, 2006, **73**, 153301.
- 21 L. Pauling, *Proc. Nat. Acad. Sci.*, 1930, **16**, 123-129.
- 22 E. Paineau, I. Bihannic, C. Baravian, A. M. Philippe, P. Davidson, P. Levitz, S. S. Funari, C. Rochas and L. J. Michot, *Langmuir*, 2011, **27**, 5562-5573.
- 23 G. Lagaly and S. Ziesmer, *Adv. Colloid Interface Sci.*, 2003, **100-102**, 105-128.
- 24 N. Miyamoto, H. Iijima, H. Ohkubo and Y. Yamauchi, *Chem. Commun.*, 2010, **46**, 4166-4168.
- 25 T. Nakato and N. Miyamoto, *Materials*, 2009, **2**, 1734.
- 26 F. Geng, R. Ma, Y. Ebina, Y. Yamauchi, N. Miyamoto and T. Sasaki, *J. Am. Chem. Soc.*, 2014, **136**, 5491-5500.
- 27 T. Maluangnont, K. Matsuba, F. Geng, R. Ma, Y. Yamauchi and T. Sasaki, *Chem. Mater.*, 2013, **25**, 3137-3146.
- 28 T. Sasaki and M. Watanabe, *J. Am. Chem. Soc.*, 1998, **120**, 4682-4689.
- 29 J. C. Gabriel, F. Camerel, B. J. Lemaire, H. Desvaux, P. Davidson and P. Batail, *Nature*, 2001, **413**, 504-508.
- 30 E. L. Cussler, S. E. Hughes, W. J. Ward III and R. Aris, *J. Membrane Sci.*, 1988, **38**, 161-174.
- 31 M. Stöter, D. A. Kunz, M. Schmidt, D. Hirsemann, H. Kalo, B. Putz, J. Senker and J. Breu, *Langmuir*, 2013, **29**, 1280-1285.
- 32 D. A. Kunz, J. Schmid, P. Feicht, J. Erath, A. Fery and J. Breu, *ACS Nano*, 2013, **7**, 4275-4280.
- 33 K. Jasmund and G. Lagaly, *G., Tonminerale und Tone: Struktur, Eigenschaften, Anwendungen und Einsatz in Industrie und Umwelt*, Steinkopff: Darmstadt, **1993**, p. 110.
- 34 J. Breu, W. Seidl, A. J. Stoll, K. G. Lange and T. U. Probst, *Chem. Mater.*, 2001, **13**, 4213-4220.
- 35 M. Daab, N. J. Eichstaedt, C. Habel, S. Rosenfeldt, H. Kalo, H. Schießling, S. Förster and J. Breu, *submitted*
- 36 G. E. Christidis, A. E. Blum and D. D. Eberl, *Appl. Clay Sci.*, 2006, **34**, 125-138.
- 37 G. E. Christidis and D. D. Eberl, *Clays Clay Miner.*, 2003, **51**, 644-655.
- 38 M. M. Herling, H. Kalo, S. Seibt, R. Schobert and J. Breu, *Langmuir*, 2012, **28**, 14713-14719.
- 39 A. R. Mermut and G. Lagaly, *Clays Clay Miner.*, 2001, **49**, 393-397.
- 40 G. Lagaly, *Clays Clay Miner.*, 1982, **30**, 215-222.
- 41 H. Kalo, W. Milius and J. Breu, *RSC Adv.*, 2012, **2**, 8452-8459.
- 42 C. D. Keenan, M. M. Herling, R. Siegel, N. Petzold, C. R. Bowers, E. A. Rössler, J. Breu and J. Senker, *Langmuir*, 2013, **29**, 643-652.
- 43 V. McGahay and M. Tomozawa, *J. Non-Cryst. Solids*, 1989, **109**, 27-34.
- 44 J. H. Markis, K. Clemens and M. Tomozawa, *J. Am. Chem. Soc.*, 1981, **64**, C-20.
- 45 Jmol: an open-source Java viewer for chemical structures in 3D. <http://www.jmol.org>
- 46 V. Marry and P. Turq, *J. Phys. Chem. B*, 2003, **107**, 1832-1839.
- 47 E. Ferrage, B. Lanson, B. A. Sakharov, N. Geoffroy, E. Jacquot and V. A. Drits, *Am. Mineral.*, 2007, **92**, 1731-1743.
- 48 M. L. Martins, W. P. Gates, L. Michot, E. Ferrage, V. Marry and H. N. Bordallo, *Appl. Clay Sci.*, 2014, **96**, 22-35.
- 49 E. Ferrage, B. Lanson, N. Malikova, A. Plançon, B. A. Sakharov and V. A. Drits, *Chem. Mater.*, 2005, **17**, 3499-3512.

SYNOPSIS TOC. To date delamination of organo-clays is restricted to highly charged, vermiculite-type layered silicates. In this work ammonium-sugars were proven to be suitable for the delamination of low and high layer charges and to be robust against heterogeneities in layer charge. The results furthermore suggest, that repulsive osmotic delamination may be applied generally to charged two dimensional materials irrespective of their charge density.



Ergebnisse

6.3.1. Supporting Information

Layer Charge Robust Delamination of Organo-Clays

Matthias Daab,^a Natalie J. Eichstaedt,^a Andreas Edenharder,^a Sabine Rosenfeldt^a and Josef Breu^{a*}

^aBavarian Polymerinstitute and Department of Chemistry, University of Bayreuth, D-95440 Bayreuth, Germany

Supporting Information

Content:

1. Supporting Data
 - PXRD of Clay Minerals
 - Layer Charge Determination: Charge Density vs. Chain Length
 - Meglumine-clays: CHN and EDX
 - Volume Fraction of Gels (Calculation).
 - Glucosamine-clays
 - Hec_{pri}: birefringence
2. Supporting References

1. Supporting Data

PXRD of Clay Minerals.

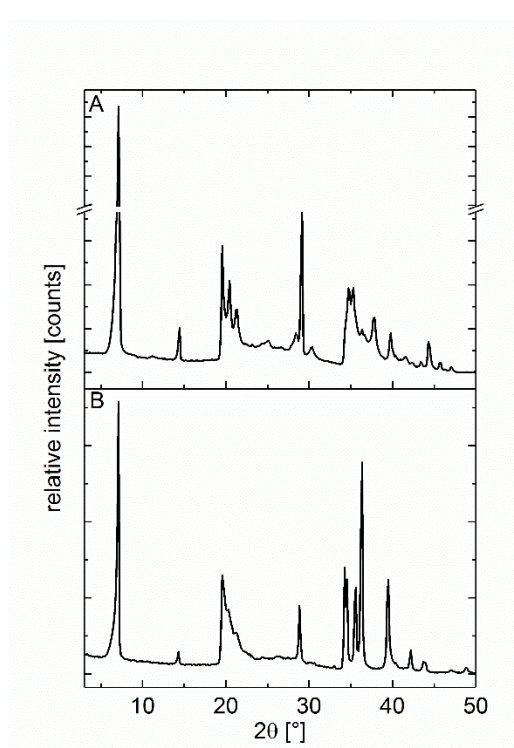


Fig. S1: PXRDs of Hec (A) and Verm (B) indicate a crystalline swollen phase with one layer of water molecules in the interlayer space ($d_{001} = 12.5 \text{ \AA}$). The patterns can be indexed in C2/m (No. 12) and least square refined lattice parameters for Hec ($a = 5.20(1) \text{ \AA}$, $b = 9.10(1) \text{ \AA}$, $c = 12.48(4) \text{ \AA}$, $\gamma = 95.44(4)^\circ$) and Verm ($a = 5.26(1) \text{ \AA}$, $b = 9.07(2) \text{ \AA}$, $c = 12.48(4) \text{ \AA}$, $\gamma = 95.22(4)^\circ$) can be derived without unindexed lines.

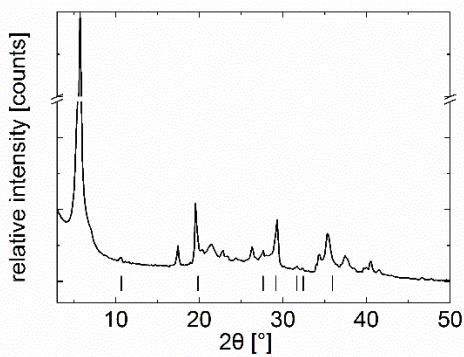


Fig. S2: PXRD of as synthesized Hec_{pri}, Proto-amphibol (PDF2-database number 00-013-0409, the most intense reflexions are marked by ticks) is found as a sidephase.

Ergebnisse

Layer Charge Determination.

Tab. S1: Layer charges corresponding to dense packings of mono- or bilayers for n-alkylammonium chains ($C_nH_{2n+1}NH_3^+$) of different length n. The layer charge that results in a dense monolayer or a dense bilayer arrangement is given as follows, assuming a typical a,b area of 47.6 \AA^2 .¹

chain lenght n	monolayer	bilayer
	[p.f.u.]	[p.f.u.]
5	0.56	1.12
6	0.50	0.99
7	0.44	0.89
8	0.40	0.80
9	0.37	0.73
10	0.34	0.67
11	0.31	0.62
12	0.29	0.58
13	0.27	0.54
14	0.25	0.51
15	0.24	0.48

Meglumine-clays: CHN-analysis and EDX.

The completeness of exchange was determined by CHN- and by EDX-analysis for the remaining sodium-content. Interlayer cation content was calculated by carbon content. The amount of organo-cations per gram clay is calculated from the determined wt% of carbon in the organo-clay; the amount of carbon atoms per Meglumine-cation (7) and the molar mass of carbon:

$$CEC_{Meglumine-clay} = \frac{wt\% C}{7 \cdot 12.011 g/mol}$$

$CEC_{Meglumine-clay}$ was compared to the expected maximum Meglumine-content in mmol / 100 g ($CEC_{Meglumine-max.}$) as calculated from the amount of exchangeable Na^+ -ions n per 100 g. The amount n is given in mval as determined by the BaCl_2 -method, $n_{verm} = 185$ mval (per 100 g), $n_{Hec} = 129$ mval (per 100 g), $n_{LCR1} = 103$ mval (per 100 g), $n_{LCR2} = 75$ mval (per 100 g) and $n_{Hec-Pri} = 116$ mval (per 100 g). Furthermore, the molar masses M of the former interlayer ions of the clays and Meglumine-cations are needed:

$$CEC_{\text{Meglu}-\text{max}} = \frac{n}{100 \text{ g} - M(\text{former interlayer ions}) \cdot n + M(\text{Meglumine}) \cdot n}$$

The completeness of organo-exchange is calculated from the ratio $\text{CEC}_{\text{Meglu-clay}} / \text{CEC}_{\text{Meglu-max}}$ and is listed in Table S2.

Tab. S2: CHN-analysis of Meglumine-clays.

	Verm	Hec	LCR1	LCR2	Hec _{pri}
wt% C	8.769	11.580	7.598	5.809	7.470
CEC _{Meglu-clay} [mmol/100g]	138	104	90	69	89
CEC _{Meglu-max} [mmol/100g]	140	105	87	66	97
deviation	-2%	-1%	+4%	+5%	-8%

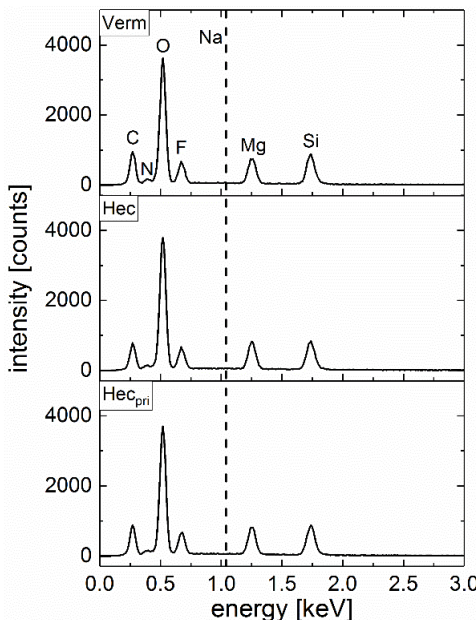


Fig. S3. The EDX-measurements of the Na-clays (Verm, Hec and Hec_{pri}) do not show remaining Na (position of Na-K α shown by dashed line) in dried Meglumine-clay (separation of Na-containing side phases like Protoamphibole was carried out by sedimentation for the case of delaminated Hec_{pri} prior to sample preparation).

Volume Fraction of Gels.

First of all, the weight-fraction of the clay lamellae in the dry Meglumine-clay sample is calculated as follows:

$$\text{wt\%}_{\text{lamellae}} = 1 - \text{wt\%}_{\text{Meglumine}}$$

The weight fraction of Meglumine is determined by CHN-analysis.

Ergebnisse

The volume fraction ϕ is calculated using the density of the lamellae (2.7 gcm^{-3}) and water (1.0 gcm^{-3}):

$$\phi = \frac{\text{wt\%}_{\text{lamellae}} \cdot m_{\text{clay}} / \rho_{\text{lamellae}}}{\text{wt\%}_{\text{lamellae}} \cdot m_{\text{clay}} / \rho_{\text{lamellae}} + m_{\text{water}} / \rho_{\text{water}}}$$

The expected d-spacing is calculated using the thickness ($t = 9.6 \text{ \AA}$) of a clay lamella:

$$d = t / \phi$$

Glucosamine-clays.

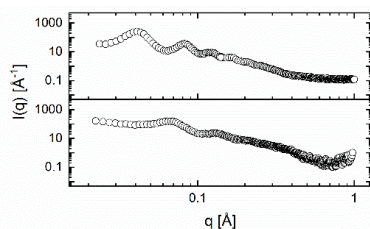


Fig. S4. SAXS-patterns of Glucosamine-clays: Verm (154 \AA , 6.1 vol%, expected: 157 \AA) and LCR2 (97 \AA , 9.3 vol%, expected: 103 \AA).

Hec_{pri}: Birefringence.

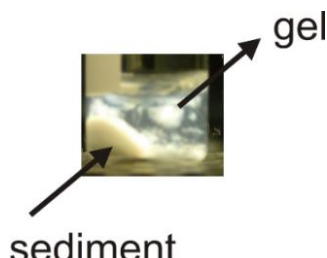


Fig. S5. Suspension of Hec_{Pri} between crossed polarizers. The supernatant gel (containing < 5 wt% of the total solid content) forms a birefringent, lyotropic suspension between crossed polarizers.

2. Supporting References

- (1) Mermut, A. R.; Lagaly, G. Baseline Studies of the Clay Minerals Society Source Clays: Layer-charge Determination and Characteristics of those Minerals Containing 2:1 Layers. *Clays Clay Miner.* 2001, **49**, 393-397.

6.4. Isomorphe Substitution und elektrische Leitfähigkeit

Matthias Daab,^[a] Patrick Loch,^[a] Wolfgang Milius,^[a] Daniela Schönauer-Kamin,^[b] Michaela Schubert,^[b] Anja Wunder,^[c] Ralf Moos,^[b] Friedrich E. Wagner^[d] and Josef Breu*^[a]

Single-Crystal Structure and Electronic Conductivity of Melt Synthesized Fe-rich, near End-Member Ferro-Kinoshitalite

Veröffentlicht: *Z. Allg. Anorg. Chem.* **2017**, 643, 1661-1667.

Reprinted with permission, Copyright (2017) Wiley-VCH.

Impact Factor (2016) *Z. Allg. Anorg. Chem.*: 1.144

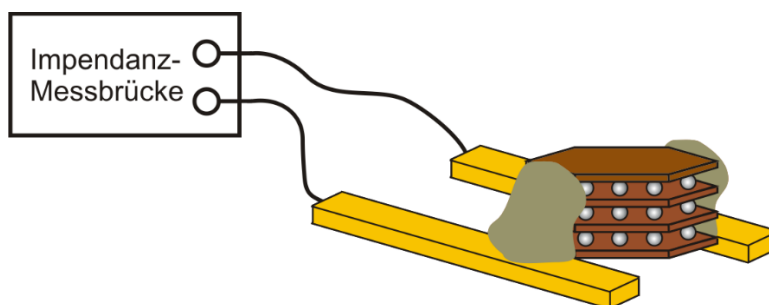
<http://dx.doi.org/10.1002/zaac.201700265>

[a] Bayerisches Polymer Institut und Lehrstuhl für Anorganische Chemie 1, Universität Bayreuth Universitätsstraße 30, 95447 Bayreuth, Germany

[b] Lehrstuhl für Funktionsmaterialien, Universität Bayreuth, Universitätsstraße 30, 95447 Bayreuth, Germany

[c] Lehrstuhl für Organische Chemie 1, Universität Bayreuth, Universitätsstraße 30, 95447 Bayreuth, Germany

[d] Physik-Department E15, Technische Universität München, James-Franck-Straße, 85748 Garching, Germany



Darstellung des Eigenanteils:

Die Synthese des Ferro-Kinoshitalites wurde von Patrick Loch selbstständig im Rahmen eines Masterpraktikums durchgeführt. Das Konzept der Publikation wurde von mir und Prof. Dr. Josef Breu erarbeitet. Das Manuskript wurde von mir verfasst und wurde mit Prof. Dr. Josef Breu zur Einreichung überarbeitet. Prof. Dr. Ralf Moos und Patrick Loch steuerten Verbesserungen bei. Von mir stammen die Auswahl, Messung und Strukturlösung des Einkristalls (mit Hilfe von Dr. Wolfgang Milius) und alle Auswertungen und Berechnungen sowie die wissenschaftliche Diskussion aller Ergebnisse im Kontext von Literatur und Vorarbeiten.

Die Kontaktierung der Einkristalle und die Impedanzspektroskopie wurde von Patrick Loch unter Anleitung von Dr. Daniela Schönauer-Kamin im Rahmen eines Masterpraktikums durchgeführt. Das Skript zur Auswertung der Impedanzmessungen stand am Lehrstuhl von Prof. Dr. Ralf Moos zur Verfügung. Michaela Schubert bestimmte die Ausdehnungen der Kristalle mit dem Lasermikroskop. Prof. Dr. Friedrich E. Wagner führte die Mössbauermessungen durch und wertete diese aus. Anja Wunder führte IR-Messungen durch. Mein Eigenanteil beträgt ca. 60 %.

Single-Crystal Structure and Electronic Conductivity of Melt Synthesized Fe-rich, near End-Member Ferro-Kinoshitalite

Matthias Daab,^[a] Patrick Loch,^[a] Wolfgang Milius,^[a] Daniela Schönauer-Kamin,^[b] Michaela Schubert,^[b] Anja Wunder,^[c] Ralf Moos,^[b] Friedrich E. Wagner,^[d] and Josef Breu^{*[a]}

Dedicated to Professor Wolfgang Schnick on the Occasion of his 60th Birthday

Abstract. In an attempt to improve the electronic conductivity an Fe^{II}-rich brittle mica, a near end-member Ferro-Kinoshitalite ($\text{BaFe}_3\text{Si}_2\text{Al}_2\text{O}_{10}\text{F}_2$) was synthesized via a melt approach. The structure is of 1M polytype [$a = 5.4013(11)$ Å, $b = 9.3659(19)$ Å, $c = 9.987(2)$ Å, $\beta = 100.52(3)^\circ$, $C2/m$] and the iron content clearly exceeds natural abundance levels. The crystal structure is discussed with respect to established limits of isomorphous substitution based on geometrical considerations and is compared to other iron-rich micas. It is

evidenced that the limitation of octahedral Fe^{II} substitution in micas is not merely governed by the misfit of tetrahedral and octahedral sheets as indicated in the literature. The electronic conductivity of contacted single crystals ($\mu\text{S}\cdot\text{cm}^{-1}$) is comparable to the conductivity of Ferrous-Tainiolite and is unfortunately not enhanced by the increased iron content. It is determined by the valence state of Fe rather than by the total Fe content.

Introduction

The chemical diversity of layered materials like graphene,^[1] metal dichalcogenides,^[2] or black phosphorus^[3] allows for fabrication of heterostructures, in which the combinations of different nanosheets result in a variety of novel and interesting optical and electronical properties.^[4] The formation of heterostructures from nanosheets requires strict control over their thickness,^[5] which is a limitation for the large-scale fabrication of such heterostructures. Delamination by shearing is never complete and requires separation of produced nanosheets. Charged layered materials, like micaceous clay minerals, provide interlayer ions that might trigger osmotic swelling. Osmotic swelling of micaceous clays represents a thermodynamically favored repulsive delamination and a gentle top down procedure for the fabrication of single nanosheets of uniform thickness from the bulk material, which is also possible for

layered double hydroxides.^[6] Micaceous clay minerals cannot only be delaminated into single nanosheets but also the controlled delamination into double stacks consisting of two nanosheets is feasible.^[7] The electronic conductivity through-plane of true micas (majority of interlayer ions being monovalent) can be tuned to some degree by the exfoliation of the bulk material as the bandgap is dependent on the number of layers stacked above each other but highly charged true micas cannot be delaminated in a controlled way.^[8] Therefore, improving the in-plane conductivity of micaceous materials, while maintaining the ability of osmotic swelling would add a highly interesting feature to the 2D family. The electronic conductivity of micas can be improved generally by increasing the transition metal content and is based on polaron hopping.^[9] Moreover, low-valent structural transition metal ions like Fe²⁺ may be oxidized post synthesis. This way the layer charge is reduced and the micaceous material becomes swellable.^[10]

For the incorporation of transition metals into the mica structure, especially for transition metal ions like Fe^{II} and Mn^{II} that are among the largest octahedral ions incorporated into the octahedral sheet (O-sheet) of micas, structure immanent limits for the degree of isomorphous substitution exist: The lateral dimensions of the two tetrahedral sheets (T-sheet) and the central O-sheet must match since they share a common $\text{O}^{2-}/(\text{OH}^-/\text{F}^-)$ anion plane; the apical oxygen ions of the tetrahedrons are also part of the octahedrons (Figure 1). The substitution limits have been related to the misfit of the O- and the T-sheet of the mica structure.^[10,11]

The limits may be stretched to a certain extent by distortions in both the O- and the T-sheet to adjust their lateral dimensions. The most prominent adjustment mechanism of the T-sheet is tetrahedral rotation (angle α).^[12] Two adjacent tetrahedrons can rotate with respect to each other along the c^* axis

* Prof. Dr. Josef Breu

E-Mail: Josef.Breu@uni-bayreuth.de

[a] Bayerisches Polymer Institut und Lehrstuhl für Anorganische Chemie 1,
Universität Bayreuth
Universitätsstraße 30
95447 Bayreuth, Germany

[b] Lehrstuhl für Funktionsmaterialien
Universität Bayreuth
Universitätsstraße 30
95447 Bayreuth, Germany

[c] Lehrstuhl für Organische Chemie 1
Universität Bayreuth
Universitätsstraße 30
95447 Bayreuth, Germany

[d] Physik-Department E15
Technische Universität München
James-Franck-Straße
85748 Garching, Germany

Supporting information for this article is available on the WWW under <http://dx.doi.org/10.1002/zaac.201700265> or from the author.

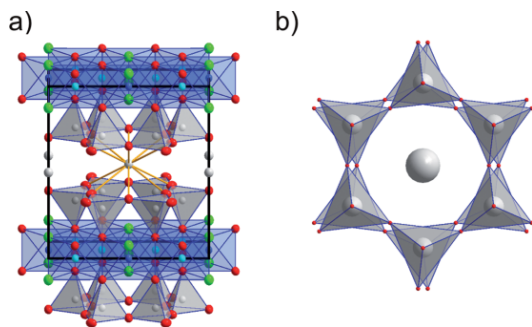


Figure 1. (a) Crystal structure (1M polytype, space group $C2/m$) of this work's Ferro-Kinoshitalite (Fe-KS) with a different color code for *cis*- (light blue) and *trans*- (blue) ions in octahedral environment, view towards (100) plane. (b) Adjacent hexagonal tetrahedral nets sandwiching the interlayer ion, view towards (001) plane.

in a counter-rotary fashion. The maximum extension for T-sheets is obtained for a tetrahedral rotation angle (α) of 0° .

For further details concerning (other) structural adjustment mechanisms the reader is referred to the elaborate work of Bailey,^[13] Guggenheim,^[14] and Brigatti,^[15] where also other crystal chemical implications affecting these parameters are discussed.

Rotation angles near 0° for the T-sheet have been determined for Annite-type micas (idealized end-member: $K_{\text{inter}}[\text{Fe}^{\text{II}}_3]^{\text{oct}.} < \text{Si}_3\text{Al}_1 >^{\text{tetr}.} \text{O}_{10}\text{F}_2$) and it was concluded that the size of the O-sheet has to be reduced by a mixed valence occupancy.^[11b,16]

In this work we focus on the synthesis of an Fe^{II} -rich brittle mica ($A_{\text{inter}}[\text{Fe}^{\text{II}}_3]^{\text{oct}.} < \text{Si}_2\text{Al}_2 >^{\text{tetr}.} \text{O}_{10}\text{F}_2$) in which the T-sheet is larger than in Annite due to 50% aluminum content. Furthermore, its electronic conductivity was determined.

Results and Discussion

A member of the brittle mica family, Ferro-Kinoshitalite (Fe-KS) of the nominal composition $\text{BaFe}_3\text{Si}_2\text{Al}_2\text{O}_{10}\text{F}_2$, was synthesized in a gas-tight molybdenum crucible from the melt (1900 °C) in a high-frequency furnace. Molybdenum is a suitable crucible material, being redox inert against the ferrous iron starting material $\text{Fe}^{\text{II}}_2\text{SiO}_4$. The crucible material at the same time acts as an O_2 buffer that fixes the oxygen fugacity in the stability field of FeO (Figure S1, Supporting Information). The powder X-ray diffraction (PXRD) shows pattern typical for micas (Figure 2a). Only minor amounts of side phases were identified: BaF_2 (B, PDF-2 database number: 00-004-0452) and a Ferro-alumosilicate (F, PDF-2 database number: 00-009-0427). Three weak reflections (*) cannot be assigned. The PXRD pattern can be indexed in $C2/m$, refined cell parameters [$a = 5.43(1)$ Å, $b = 9.33(2)$ Å, $c = 9.98(1)$ Å, $\alpha = \beta = 90^\circ$, $\gamma = 100.80(3)^\circ$] agree well with single crystal data.

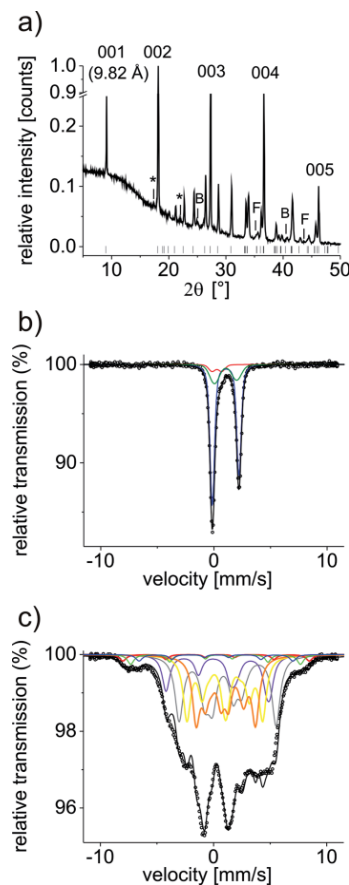


Figure 2. (a) PXRD pattern of Fe-KS. Reflections marked B belong to BaF_2 (PDF-2 database number: 00-004-0452), F belongs to a Ferro-alumosilicate (PDF-2 database number: 00-009-0427) whereas the reflections marked (*) cannot be assigned. (b) Mössbauer spectrum measured at 145 K and (c) at 4.2 K.

The Mössbauer spectrum at 145 K (fit parameters: Table S1, Supporting Information) shows a broadened Fe^{II} quadrupole doublet that was fitted by a sharp and a broad Fe^{II} component and a very weak shoulder at about $1 \text{ mm}\cdot\text{s}^{-1}$ assigned to an Fe^{III} doublet (Figure 2b). No clear indication of the presence of tetrahedral Fe^{III} was found and the overall amount of Fe^{III} is determined to be about 6 %. At high velocities no magnetic splitting at 145 K for Fe^{III} is observed. Therefore, Fe^{III} is most likely related to Fe-KS.

While for ferro-silicates typically no magnetic splitting is found at 4.2 K (fit parameters: Table S2, Supporting Information), such a magnetic splitting was observed for Annite-type micas.^[17] For the Fe-KS sample, a magnetic hyperfine splitting is observed at 4.2 K (Figure 2c). The broad pattern indicates a distribution of magnetic hyperfine fields that was approximated by three sextets with fields between 42 and 51 T for the Fe^{III} and four octet patterns with fields between 12 and 24 T for the Fe^{II} . The fact that no Fe^{II} quadrupole doublet is observed any more at 4.2 K is a strong indication that all Fe^{II} is incorporated into the Fe-KS.

Wavelength dispersive electron microprobe analysis yields a composition of $\text{Ba}_{0.98(1)}^{\text{inter}}[\text{Fe}^{\text{II}}_{2.38(7)}\text{Fe}^{\text{III}}_{0.15(1)}-\text{Al}_{0.28(1)}]^{\text{oct}.} < \text{Si}_{2.01(49)}\text{Al}_{1.99(10)} >^{\text{tetr}.} \text{O}_{10}\text{F}_2$. This formula was

derived from the atomic ratios by assuming full occupancy of tetrahedral sites and by normalizing to a total cationic charge of 22 matching the negative charge of the anionic sublattice ($O_{10}F_2$ per formula unit, p.f.u.). Additionally, the IR spectrum of Fe-KS shows the tetrahedral- and octahedral-vibration bands (Figure S2, Supporting Information).

During single crystal structure refinement, interlayer Ba^{2+} and the octahedral $Fe^{II/III}$ positions were freely refined, while all other occupation factors were fixed according to this formula determined by microprobe analysis. This way a composition of $Ba_{0.963(7)}^{inter}[Fe_{2.681(15)}Al_{0.28}]^{oct}<Si_{2.01}Al_{1.99}>^{tet}O_{10}F_2$ resulted from the refinement that, within experimental errors, agrees with the formula based on the microprobe analysis. As observed recently for natural samples of Kinoshitalite^[25] and a Mg-rich Ferro-Kinoshitalite^[20] it was not possible to determine the in-plane ordering of Al–Si tetrahedrons that would be expected according to Loewenstein's rule.^[26] Most likely, the ordering indeed exists within a single T-sheet but is not conserved in the random stacking resulting in the (artificially) higher symmetric space group $C2/m$ that does not allow for tetrahedral ordering [$a = 5.4013(11)$ Å, $b = 9.3659(19)$ Å, $c = 9.987(2)$ Å, $\alpha = \gamma = 90^\circ$, $\beta = 100.52(3)^\circ$]. Details of the structure refinement are given in Table 1; atomic coordinates in Table 2; and anisotropic displacement parameters in Table S3 (Supporting Information).

The crystal structure of Fe-KS is discussed via selected bond lengths (Table 3) and by a comparison of the structural parameters (Table 4) to those of other (iron-rich) micas. These micas are synthetic Ferro-Tainiolite^[10] ($Cs^{inter}[Fe_2Li]^{oct}<Si_4>^{tet}O_{10}F_2$, Fe-Tain), a natural Ferro-Kinoshitalite^[20] ($Ba_{0.47}K_{0.33}Na_{0.04}^{inter}[Fe^{2+}_{1.72}Mg_{0.74}Mn_{0.08}Fe^{3+}_{0.15}Ti_{17}]^{oct}<Si_{2.44}Al_{1.56}>^{tet}O_{10}F_2$, KS-nat) and a synthetic sodium-brittle mica^[21] ($Na_{3.4}^{inter}[Mg_3]^{oct}<Si_{2.3}Al_{1.7}>^{tet}O_{10}F_2$, Na-BM).

To quantitatively evaluate the misfit of both sheets and to obtain a demonstrative parameter for that purpose, the ratio of lateral (a,b) dimensions of the undistorted T-sheet and the undistorted O-sheet is calculated, $(a,b)_t / (a,b)_o$. The (a,b) dimensions are calculated from the mean bond length of a polyhedron. The tetrahedral bond length $<T-O>_{shannon}$ and the octahedral bond length $<M-O/F>_{shannon}$ that are expected for a refined composition are calculated via Shannon^[22] radii (high-spin state). The small amount of octahedral vacancies was not taken into account.^[14] Subsequently, the (a,b) dimensions are

Table 1. Crystallographic data and details of the structure determination of Fe-KS.

	Fe-Kinoshitalite
Empirical formula	$Ba_{0.963(7)}[Fe_{2.681(15)}Al_{0.28}]<Si_{2.01}Al_{1.99}>O_{10}F_2$
MW /g·mol ⁻¹	598.1
a /Å	5.4013(11)
b /Å	9.3659(19)
c /Å	9.987(2)
$\alpha = \gamma$ /°	90
β /°	100.52(3)
Z	2
Density / g·cm ⁻³	4.1
Dimensions /mm ³	$0.25 \times 0.23 \times 0.02$
Abs. coefficient μ /mm ⁻¹	8.28
Crystal system	monoclinic
Space group	$C2/m$ (no. 12)
Diffractometer	STOE IPDS I
Radiation	$Mo-K_\alpha$ (0.71073 Å)
Monochromator	Graphite
T /K	293
Data collection mode	omega scans
$\theta_{min} - \theta_{max}$ /°	2.074–25.785
Index range (hkl)	6, -6; 11, -11; 11, -12
Reflections collected	1784
Reflections unique	508
Reflections $I > 2\sigma(I)$	495
R_{int}	0.0704
Absorption correction	Numerical
Solution and refinement	SHELXT ^[18] and SHELXL ^[19]
Refinement on	F^2
R_1 [$I > 2\sigma(I)$]	0.0334
wR_2 [$I > 2\sigma(I)$]	0.0938
R_1 (all data)	0.0339
wR_2 (all data)	0.0946
Goodness of fit	0.863
$\Delta\rho_{max}$ and $\Delta\rho_{min}$ ($e\cdot\text{\AA}^{-3}$)	1.237 and -0.856
Refined parameters	56

calculated as follows:^[23] $b_o = 3\sqrt{2}<M-O/F>_{shannon}$ and $b_t = 4\sqrt{2}<M-O/F>_{shannon}$ and $a = b/\sqrt{3}$ (for the derivation of the equations see Figure S3, Supporting Information).

The ratio $(a,b)_t / (a,b)_o$ is increasing in the row Fe-Tain, KS-nat, Fe-KS, and Na-BM (1.03, 1.12, 1.13, and 1.15). As expected, the tetrahedral rotation angle α increases with $(a,b)_t / (a,b)_o$ in order to decrease the T-sheet's lateral extension (0.14, 3.95, 6.83, and 11.86°, for Fe-Tain, KS-nat, Fe-KS, and Na-BM, respectively). This is the main adjustment

Table 2. Atomic coordinates of Fe-KS. *Cis* (c) and *trans* (t) octahedral sites as well as apical (a) and basal (b) oxygen atoms are distinguished by subscripts.

Atom	Site	s.o.f.	x/a	x/b	x/c
Ba	2c	0.963(7)	1/2	1/2	1/2
Fe _c	4g	0.892(8)	1/2	0.33249(9)	0
Al _c	4g	0.0933	1/2	0.33249(9)	0
Fe _t	2b	0.897(10)	1	1/2	0
Al _t	2b	0.0933	1	1/2	0
Si	8j	0.5025	0.9255(2)	0.33370(11)	0.28108(13)
Al	8j	0.4975	0.9255(2)	0.33370(11)	0.28108(13)
O1 _a	8j	1	0.8682(6)	0.3352(3)	0.1100(4)
O2 _b	4i	1	0.9814(10)	1/2	0.3437(5)
O3 _b	8j	1	0.6792(6)	0.2672(4)	0.3437(3)
F	4i	1	0.3756(7)	1/2	0.1118(5)

Table 3. Selected bond lengths /Å of Fe-KS. *Cis* (c) and *trans* (t) octahedral sites as well as apical (a) and basal (b) oxygen atoms are distinguished by subscripts.

Bond	Bond length
Octahedral site	
$M_c\text{--O}$	2.113(4)
$M_c\text{--O}$	2.089(3)
$M_c\text{--F}$	2.106(3)
$M_t\text{--O}$	2.093(3)
$M_t\text{--F}$	2.130(4)
Tetrahedral site	
$T\text{--O}_1\text{a}$	1.680(4)
$T\text{--O}_2\text{b}$	1.685(2)
$T\text{--O}_3\text{b}$	1.689(4)
$T\text{--O}_3\text{b}$	1.688(3)
Interlayer space	
$\text{Ba}\text{--O}_{\max}$	3.273(4)
$\text{Ba}\text{--O}_{\min}$	2.946(4)

mechanism of the T-sheet, while the tetrahedral flattening angle τ is a parameter difficult to study in mica crystal chemistry:

τ has to be “isolated” from the influence of the divalent interlayer cation in brittle micas for comparison with true micas and the influence of the misfit of the sheets is therefore strongly superimposed by electrostatics.^[15] Moreover, the thickness of the T-sheet t_d not only increases (2.227, 2.270, 2.295, and 2.307 Å for Fe-Tain, KS-nat, Fe-KS, and Na-BM, respectively) to further reduce its lateral extension with increasing $(a,b)_t / (a,b)_o$. Interestingly, the thickness of the T-sheet t_d increases from Fe-KS to Na-BM although the mean tetrahedral bond length decreases due to the decreasing Al:Si ratio.

One adjustment mechanism of the O-sheet is the deviation from the mean bond length $\langle M\text{--O/F} \rangle_{\text{mean}}$ of the bond length that is calculated via Shannon radii^[22] $\langle M\text{--O/F} \rangle_{\text{shannon}}$. While for the smallest tetrahedral sheet (Fe-Tain) $\langle M\text{--O/F} \rangle_{\text{mean}}$ is smaller than calculated, it is larger than calculated for KS-nat, but only slightly larger in case of Fe-KS, where there is no significant difference in *trans*- and *cis*-octahedron size. For Fe-KS the adjustment is mainly achieved via a that is significantly larger in comparison to KS-nat, although $(a,b)_t / (a,b)_o$ is similar for both micas.

Table 4. Structural parameters obtained from single-crystal refinement for synthetic Ferro-Kinoshitalite (Fe-KS, this work), for Ferrous-Tainiolite^[10] ($\text{Cs}[\text{Fe}_2\text{Li}]<\text{Si}_4>\text{O}_{10}\text{F}_2$, Fe-Tain), natural Fe-bearing Kinoshitalite^[20] ($\text{Ba}_{0.47}\text{K}_{0.33}\text{Na}_{0.04}[\text{Fe}^{2+}_{1.72}\text{Mg}_{0.74}\text{Mn}_{0.08}\text{Fe}^{3+}_{0.15}\text{Ti}_{1.17}]<\text{Si}_{2.44}\text{Al}_{1.56}>\text{O}_{10}\text{F}_2$, KS-nat) and sodium brittle mica^[21] ($\text{Na}_{3.4}[\text{Mg}_3]<\text{Si}_{2.3}\text{Al}_{1.7}>\text{O}_{10}\text{F}_2$, Na-BM).

Parameters ^{a)}	Fe-Tain ($C2/m$)	KS-nat ($C2/m$)	Fe-KS ($C2/m$)	Na-BM ($C2$)
$(a,b)_t / (a,b)_o$ ^{b)}	1.03	1.12	1.13	1.15
Tetrahedral sheet				
$\langle T\text{--O}_b \rangle / \text{\AA}^c$	1.649	1.674	1.687	1.679 <Si> and 1.718 <Al,Si>
$\langle T\text{--O}_a \rangle / \text{\AA}^c$	1.597	1.665	1.680	1.715 <Si> and 1.679 <Al,Si>
$\langle T\text{--O} \rangle / \text{\AA}^d$	1.618	1.665	1.678	1.670
τ ^{e)}	112.4	111.3	111.7	111.2
a ^{f)}	0.14	3.95	6.83	11.86
$t_d / \text{\AA}^g$	2.227	2.270	2.295	2.307
Octahedral sheet				
$\langle M\text{--O/F} \rangle_{\text{cis}} / \text{\AA}^h$	2.098	2.106	2.103	2.074 and 2.102
$\langle M\text{--O/F} \rangle_{\text{trans}} / \text{\AA}^h$	2.098	2.120	2.105	2.043
$\langle M\text{--O/F} \rangle_{\text{mean}} / \text{\AA}^h$	2.098	2.111	2.104	2.073
$\langle M\text{--O/F} \rangle_{\text{shannon}} / \text{\AA}^i$	2.127	2.102	2.103	2.073
$o_d / \text{\AA}^j$	2.282	2.216	2.172	2.104
e_u/e_s ^{k)}	1.058	1.091	1.106	1.120
Ψ ^{l)}	57.05	58.34	58.92	59.50
Interlayer space				
$h / \text{\AA}^m$	3.900	3.129	3.069	5.247
$\langle A\text{--O} \rangle_{\max} / \text{\AA}^n$	3.285	3.210	3.273	3.201
$\langle A\text{--O} \rangle_{\min} / \text{\AA}^n$	3.271	3.018	2.946	2.438

a) Definition and calculation of parameters listed, see below. Parameters were recalculated as proposed by Brigatti and Guggenheim^[15] from the original publications as there are older definitions^[12] of some of the parameters. **b)** $(a,b)_t / (a,b)_o$ = ratio of the a,b area for ideal, undistorted tetrahedral and octahedral sheets. The (a,b) dimensions are calculated from the mean bond length of a polyhedron. The tetrahedral bond length $\langle T\text{--O} \rangle_{\text{shannon}}$ and the octahedral bond length $\langle M\text{--O/F} \rangle_{\text{shannon}}$ that are expected for a refined composition are calculated via Shannon radii,^[22] high-spin state. Using the bond lengths, the (a,b) dimensions are calculated as follows^[23] $b_0 = 3\sqrt{2} \langle M\text{--O/F} \rangle_{\text{shannon}}$ and $b_t = 4\sqrt{2} \langle M\text{--O/F} \rangle_{\text{shannon}}$ and $a = b_t/\sqrt{3}$ (derivation of the equations: Figure S3, Supporting Information). No influence of octahedral vacancies (KS-nat and Fe-KS) on the calculated $\langle M\text{--O/F} \rangle_{\text{shannon}}$ has been assumed.^[14] Shannon radii (coordination numbers in subscripts) are: 1.35 Å basal-O_{ii}, 1.38 Å apical-O_{iv}, 1.30 Å F_{iii}, 0.26 Å Si_{iv}, 0.39 Å Al_{iv}, 0.78 Å Fe^{II}_{vi}, 0.76 Å Li_{vi}, 0.535 Å Al_{vi}, 0.72 Å Mg_{vi}, 0.83 Å Mn_{vi}, 0.645 Å Fe^{III}_{vi}, 0.605 Å Ti^{IV}_{vi}. **c)** $\langle T\text{--O}_b \rangle$ and $\langle T\text{--O}_a \rangle$ = mean basal and apical cation–oxygen bond length of tetrahedrons, for Na-BM (space group $C2$) separate values for the <Si> and the <Al,Si> tetrahedrons are given. **d)** $\langle T\text{--O} \rangle_{\text{Shannon}}$ = mean tetrahedral bond length as calculated by Shannon radii,^[22] high-spin state, according to the refined tetrahedral composition. **e)** τ = mean O_{apical}–T–O_{basal} angle.^[15] **f)** a = tetrahedral rotation 1/6 $\sum 1120^\circ - \Phi/2$ with Φ being the angle between bridging basal oxygen atoms.^[15] **g)** t_d = thickness of the tetrahedral sheet.^[15] **h)** $\langle M\text{--O/F} \rangle_{\text{trans}}$, $\langle M\text{--O/F} \rangle_{\text{cis}}$ and $\langle M\text{--O/F} \rangle_{\text{mean}}$ = mean cation–anion bond length in *trans* and *cis* octahedrons and octahedral mean bond length (ratio 2:1 of *cis* and *trans* octahedrons). **i)** $\langle M\text{--O/F} \rangle_{\text{shannon}}$ = mean octahedral bond length as calculated by Shannon radii,^[22] high-spin state, according to the refined octahedral composition. No influence of octahedral vacancies (KS-nat and Fe-KS) on the calculated $\langle M\text{--O/F} \rangle_{\text{shannon}}$ was assumed (justified in the caption of Figure S3). **j)** o_d = thickness of the octahedral sheet.^[15] **k)** e_u/e_s = ratio of the mean length of unshared to shared octahedral edges.^[24] **l)** Ψ = octahedral flattening angle, arccos $(o_d / (2 \langle M\text{--O/F} \rangle_{\text{mean}}))^{1/2}$. **m)** h = interlayer separation of the basal planes.^[15] **n)** $\langle A\text{--O} \rangle_{\max}$ and $\langle A\text{--O} \rangle_{\min}$ = maximum and minimum bond length of the interlayer ion A with the basal oxygen atoms.

As expected, the octahedral flattening angle Ψ , that increases the lateral extension of the O-sheet, becomes larger with increasing $(a,b)_t / (a,b)_o$ values (57.05, 58.34, 58.92, and 59.50° for Fe-Tain, KS-nat, Fe-KS, and Na-BM, respectively). Related to Ψ increase, the ratio of the length of unshared to shared octahedral edges (e_u/e_s), (1.058, 1.091, 1.106, and 1.120 for Fe-Tain, KS-nat, Fe-KS, and Na-BM, respectively) increases, which also reduces the thickness of the octahedral layer o_d (2.282, 2.216, 2.172, and 2.104 Å for Fe-Tain, KS-nat, Fe-KS, and Na-BM, respectively) and this way maximizes the lateral size of the O-sheet. For Fe-KS no pronounced *cis/trans* preference is obvious from the site occupation factors (Table 2) and the bond lengths (Table 3).

The interlayer separation h is governed by the ionic radius of the interlayer ion and – in case of Na-BM – of its hydration state. The hydration of Na-BM leads to a complex interlayer space that is discussed elsewhere^[21] and cannot be compared with non-hydrated Fe-Tain, KS-nat, and Fe-KS. In case of Fe-Tain, h (3.900 Å) is significantly larger than in KS-nat (3.129 Å) and Fe-KS (3.069 Å) due to the larger ionic radius of Cs^+ . However, with both, decreasing interlayer separation h and increasing distortion of the hexagonal cavity (tetrahedral rotation angle α , 0.14°, 3.95°, and 6.83° for Fe-Tain, KS-nat, and Fe-KS, respectively) the difference in maximum ($\langle A-O \rangle_{\max}$) and minimum ($\langle A-O \rangle_{\min}$) interlayer ion to basal oxygen separation is increasing (0.014 Å, 0.192 Å and 0.327 Å for Fe-Tain, KS-nat, and Fe-KS, respectively).

With an interlayer separation of 3.069 Å the basal oxygen atoms of Fe-KS are in direct contact (van der Waals radius of O^{2-} according to *Batsanov*: 1.55 Å).^[27] The repulsion of basal oxygen atoms is avoided by the distortion of the T-sheet (Figure 1b) that results in a slightly staggered arrangement of adjacent basal oxygen atoms.

To sum up, the increasing misfit $(a,b)_t / (a,b)_o$ in the row Fe-Tain, KS-nat, Fe-KS, and Na-BM (1.03, 1.12, 1.13, and 1.15, respectively) is compensated for by several adjustment mechanisms. Nevertheless, the end-member Ferro-Kinoshitalite ($\text{Ba}^{\text{inter}}[\text{Fe}^{\text{II}}_3]^{\text{oct}}<\text{Si}_2\text{Al}_2>^{\text{tetra}}\text{O}_{10}\text{F}_2$) could not be synthesized. Since Fe-KS does not show the largest misfit, it would, however, be expected to be accessible. It therefore appears that the substitution limit for octahedral Fe^{II} incorporation ($r = 0.78$ Å) cannot be rationalized by purely geometrical factors as suggested in the literature for Annite.^[11b,16] Electronic considerations (e.g. an upper limit of the valence electron concentration in octahedral positions) have not yet been considered. An elaborate study of >6000 mica structures and their solid solutions was carried out by *Tischendorf*.^[28] But as natural micas have a complex chemical composition and are in most cases mixed valence compounds, predictions on the miscibility

of the cations in true end-members are nevertheless impossible. The only way out is the synthetic exploration of accessible (near) end-members in future studies.

The conductivity of Fe-KS was measured by impedance spectroscopy and is compared to the conductivity of previously reported Fe-Tain^[10] that is about 30 % lower in iron content. To rule out the influence of side phases and grain boundaries, single crystals were picked (Fe-KS1, Fe-KS2, and Fe-Tain1) and contacted with a Pt-paste on gold electrodes (Figure 3) to measure the in-plane conductivity. The electronic conductivity (σ , Table 5) was calculated from the size of the crystals and the DC-resistance obtained by extrapolation of the Nyquist-plot against zero frequency (Figure S4, Supporting Information).

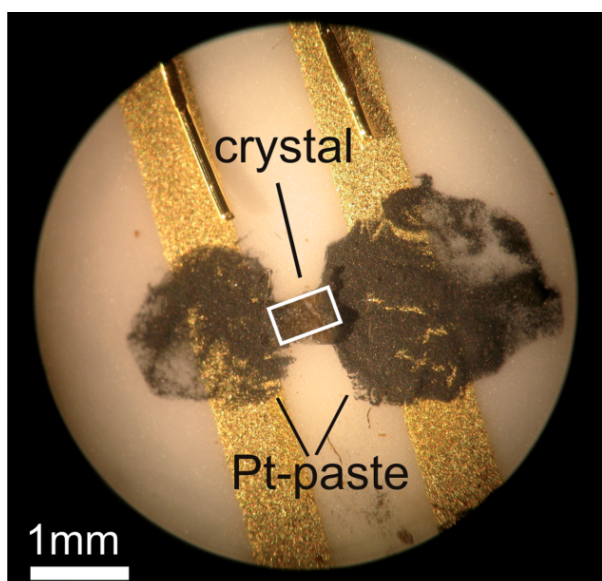


Figure 3. Optical microscopy of a typical crystal contacted with Pt-Paste on gold electrodes.

The charge transport mechanism in micas is polaron hopping.^[10] For the conductivity of iron-bearing micas a linear dependency with the Fe^{II} content was reported (along with a decrease in conductivity with increasing Fe^{III} and fluoride content)^[29] but also a (linear^[19]) increase with the total iron content was found.^[30] A plateau in conductivity was proposed by *Toland* with > 1.5 Fe p.f.u.^[31] The large differences in chemical composition of natural micas, however, hampered clear conclusions as to the main factors governing the conductivity of micas.^[19]

The conductivity of both, as-prepared Fe-KS and as-prepared Fe-Tain is in the order of magnitude of $\mu\text{S}\cdot\text{cm}^{-1}$ at

Table 5. Conductivity of different single-crystals of Fe-Tain and Fe-KS at 200 °C. The dimensions and the electronic conductivity (σ) in nitrogen and air atmosphere of the crystals are shown.

	Fe-KS1	Fe-KS2	Fe-Tain1
Size /mm	$0.65 \times 0.38 \times 0.004$	$0.92 \times 0.32 \times 0.007$	$1.02 \times 0.47 \times 0.005$
$\sigma(\text{N}_2) / \mu\text{S}\cdot\text{cm}^{-1}$	1.5(1)	4.1(2)	3.5(2)
$\sigma(\text{air}) / \mu\text{S}\cdot\text{cm}^{-1}$	3.3(2)	22.2(9)	8.0(4)

200 °C in a nitrogen atmosphere (Table 5). The conductivities of the same crystals are enhanced by a factor > 2 upon a change in redox potential of the atmosphere (in air). The obtained conductivities are about three orders of magnitude smaller than for a bulk sample of Fe-Tain at the same temperature,^[10] which is related to the absence of both, grain boundaries and a random orientation of different platelets due to the use of single crystals in this work. A pronounced effect of the transition metal content (≥ 2 Fe p.f.u.) on the specific conductivity is not observed within experimental errors. This is in line with *Tollands* observation that most of the increase in conductivity happens around 1.5 Fe p.f.u.^[31] The sensitivity of Fe-KS to the redox potential of the gas atmosphere might be explained by Fe^{III} atoms acting as hopping centers.^[30] According to the Mössbauer spectrum, upon oxidation in air the Fe^{III} content increases from 6% to 13% (Figure S5, Table S4, Supporting Information).

Conclusions

In this work the crystal structure of a melt synthesized, near end-member Ferro-Kinoshitalite, $\text{Ba}_{0.963(7)}[\text{Fe}_{2.681(15)}\text{Al}_{0.28}]<\text{Si}_{2.01}\text{Al}_{1.99}>\text{O}_{10}\text{F}_2$, was determined by single-crystal structure solution. The discussion of its crystal chemistry revealed, that the limitation of isomorphous substitution for large transition metals in micas cannot solely be attributed to geometric constraints. Rules established in literature should not refrain from attempting to synthesize compositions that are expected to have interesting physical properties or applications. The electric conductivity of iron-rich micas (≥ 2 Fe p.f.u.) is determined by the valence state of Fe rather than by the total Fe content.

Experimental Section

Melt Synthesis: Fe-KS was prepared by melt synthesis in a gas tight molybdenum-crucible. The handling of the crucible is described in detail elsewhere.^[32] The starting materials (4 g in total) BaF₂ (99.99%, Sigma Aldrich), α -Al₂O₃ (>99.95%, Alfa Aesar), SiO₂ (Merck, fine granular quarz, purum) and Fe₂SiO₄ (Fayalite, synthesized as described previously^[11c]) were mixed according to the nominal composition BaFe₃Si₂Al₂O₁₀F₂. The crucible was sealed gas tight and was ramped to 1900 °C in a high-frequency furnace under vacuum (<10⁻⁵ mbar). After 30 min dwell time it was quenched by switching off the power. The crucible was turned upside down, heated and quenched for one more time. The cool crucible was broken to obtain the product. Fe-Tain was prepared as described in earlier work.^[10] The PXRD of Fe-Tain is shown in Figure S6 (Supporting Information).

Single Crystal: For X-ray data collection, a single crystal (0.25 mm × 0.23 mm × 0.02 mm) was selected. The intensity data were collected at 293 K with a STOE IPDS I diffractometer using graphite-monochromated Mo- K_{α} radiation. A numerical absorption correction was applied using the program X-RED34 based on a crystal shape description optimized using equivalent reflections with X-SHAPE34. The solution and the refinement were carried out using SHELXT^[18] and SHELXL,^[19] implemented in Olex2^[33] (OlexSys). The occupancy of Ba and Fe (4h and 2d positions) were freely refined. All other occupancies were fixed according to microprobe analysis; all positions could be refined anisotropically.

Further details of the crystal structure investigations may be obtained from the Fachinformationszentrum Karlsruhe, 76344 Eggenstein-Leopoldshafen, Germany (Fax: +49-7247-808-666; E-Mail: crysdata@fiz-karlsruhe.de, <http://www.fiz-karlsruhe.de/request.html> for deposited data) on quoting the depository number CSD-433396.

Powder X-ray Diffraction: The powdered sample, mounted on a zero background spinner, was measured in Bragg-Brentano geometry with a PANalytical X'pert Pro equipped with an X'Celerator Scientific RTMS detector (Cu- K_{α} radiation) and a secondary beam monochromator to suppress fluorescence.

Microprobe Analysis: The chemical composition of Fe-KS was determined by wavelength dispersive X-ray spectroscopy on single crystals with flat lying surfaces on a carbon grid using an electron microprobe (Jeol JXA-8200, Bayerisches Geoinstitut, Bayreuth). The settings were 15 kV acceleration voltage, 15 nA initial beam current, a beam spot diameter of 10 μm , 20 s counting time at the peak position and 10 s counting time at each side of the peak. Calibration was done using commercial mineral standards: BaSO₄ (Ba), Fe (Fe), MgAl₂O₄ (Al), MgSiO₃ (Si), SiO₂ (O) and CaF₂ (F).

FT-IR Spectroscopy: The measurement was recorded with a PerkinElmer ONE FT-IR spectrometer equipped with an ATR module.

Mössbauer Spectroscopy: ⁵⁷Fe Mössbauer spectra of powdered samples were measured at ambient temperature, 145 K and 4.2 K with a source of ⁵⁷Co in a rhodium matrix that was kept at the same temperature as the absorber. For velocity calibration α -Fe was used. The spectra were least-squares fitted with line shapes corresponding to a Gaussian broadening of Lorentzian lines (Voigt profiles) grouped into quadrupole doublets and, for the 4.2 K spectrum, with appropriate superpositions of magnetically split sextets (for Fe^{III}) and octets (for Fe^{II}).

Impedance Spectroscopy: The crystals were contacted with Pt-paste on gold electrodes (Figure 3). The impedances were measured at 200 °C in a corundum furnace at frequencies between 10⁻¹ and 10⁷ Hz (Novocontrol Alpha Analyzer, 200 mV).

Supporting Information (see footnote on the first page of this article): Phase barogram of the iron-molybdenum system, calculations of $(a,b)_t$ / $(a,b)_o$, anisotropic displacement parameters, Nyquist-plots, Mössbauer spectra of oxidized Fe-KS and PXRD of Fe-Tain.

Acknowledgements

This work was supported by the Deutsche Forschungsgemeinschaft (SFB 840). M.D. thanks the Fonds der Chemischen Industrie for a fellowship. P.L. thanks Elite Network Bavaria in the framework of the Elite Study Program "Macromolecular Science". Prof. Rainer Schobert is acknowledged for making IR equipment available. The authors thank Bayerisches Geoinstitut for electron microprobe analysis.

Keywords: Crystal chemistry; Conductivity; Fe-rich mica; Single crystal; Brittle mica

References

- [1] K. S. Novoselov, V. I. Falko, L. Colombo, P. R. Gellert, M. G. Schwab, K. Kim, *Nature* **2012**, *490*, 192–200.

- [2] M. Chhowalla, H. S. Shin, G. Eda, L. J. Li, K. P. Loh, H. Zhang, *Nat. Chem.* **2013**, *5*, 263–275.
- [3] P. W. Bridgman, *J. Am. Chem. Soc.* **1914**, *36*, 1344–1363.
- [4] a) H. Lim, S. I. Yoon, G. Kim, A. R. Jang, H. S. Shin, *Chem. Mater.* **2014**, *26*, 4891–4903; b) A. K. Geim, I. V. Grigorieva, *Nature* **2013**, *499*, 419–425; c) D. Jariwala, T. J. Marks, M. C. Hersam, *Nat. Mater.* **2017**, *16*, 170–181.
- [5] B. V. Lotsch, *Ann. Rev. Mater. Res.* **2015**, *45*, 85–109.
- [6] a) M. Daab, S. Rosenfeldt, H. Kalo, M. Stöter, B. Bojer, R. Siegel, S. Förster, J. Senker, J. Breu, *Langmuir* **2017**, *33*, 4816–4822; b) S. Rosenfeldt, M. Stöter, M. Schlenk, T. Martin, R. Q. Albuquerque, S. Förster, J. Breu, *Langmuir* **2016**, *32*, 10582–10588; c) L. J. Michot, I. Bihannic, S. Maddi, S. S. Funari, C. Baravian, P. Levitz, P. Davidson, *Proc. Natl. Acad. Sci. USA* **2006**, *103*, 16101–16104; d) K. Norrish, *Disc. Faraday Soc.* **1954**, *18*, 120–134; e) W. G. Garret, G. F. Walker, *Clays Clay Miner.* **1960**, *9*, 557–567; f) J. A. Rausell-Colom, J. Saez-Anuon, C. H. Pons, *Clay Miner.* **1988**, *24*, 459–478; g) G. Abellan, C. Martí-Gastaldo, A. Ribera, E. Coronado, *Acc. Chem. Res.* **2015**, *48*, 1601–1611; h) Q. Wang, D. O'Hare, *Chem. Rev.* **2012**, *112*, 4124–4155.
- [7] a) M. Stöter, B. Biersack, S. Rosenfeldt, M. J. Leitl, H. Kalo, R. Schobert, H. Yersin, G. A. Ozin, S. Förster, J. Breu, *Angew. Chem. Int. Ed.* **2015**, *54*, 4963–4967; b) M. Stöter, S. Gödrich, P. Feicht, S. Rosenfeldt, H. Thurn, J. W. Neubauer, M. Seuss, P. Lindner, H. Kalo, M. Möller, A. Fery, S. Förster, G. Papastavrou, J. Breu, *Angew. Chem. Int. Ed.* **2016**, *55*, 7398–7402.
- [8] S. S. Kim, T. V. Khai, V. Kulish, Y. H. Kim, H. G. Na, A. Katoch, M. Osada, P. Wu, H. W. Kim, *Chem. Mater.* **2015**, *27*, 4222–4228.
- [9] M. Meunier, J. F. Currie, M. R. Wertheimer, A. Yelon, *J. Appl. Phys.* **1983**, *54*, 898–905.
- [10] R. Mariyachuk, A. Baumgartner, F. E. Wagner, A. Lerf, A. Dubbe, R. Moos, J. Breu, *Chem. Mater.* **2007**, *19*, 5377–5387.
- [11] a) R. M. Hazen, D. R. Wones, *Am. Mineral.* **1978**, *63*, 885–892; b) G. J. Redhammer, A. Beran, E. Dachs, G. Amthauer, *Phys. Chem. Miner.* **1993**, *20*, 382–394; c) A. Baumgartner, C. Buterhof, S. Koch, R. Mariyachuk, J. Breu, *Clays Clay Miner.* **2009**, *57*, 271–277.
- [12] G. Donnay, N. Morimoto, H. Takeda, *Acta Crystallogr.* **1964**, *17*, 1374–1381.
- [13] S. W. Bailey, *Am. Mineral.* **1982**, *67*, 394–398.
- [14] S. Guggenheim, R. A. Eggleton, *Am. Mineral.* **1987**, *72*, 724–738.
- [15] M. F. Brigatti, S. Guggenheim, *Rev. Mineral. Geochem.* **2002**, *46*, 1–97.
- [16] R. M. Hazen, D. R. Wones, *Am. Mineral.* **1972**, *57*, 103–119.
- [17] I. A. D. Christie, D. G. Rancourt, G. Lamarche, M. Royer, H. Kodama, J. L. Robert, *Hyperfine Interact.* **1992**, *68*, 315–318.
- [18] G. Sheldrick, *Acta Crystallogr., Sect. A* **2015**, *71*, 3–8.
- [19] G. Sheldrick, *Acta Crystallogr., Sect. C* **2015**, *71*, 3–8.
- [20] S. Guggenheim, H. E. Frimmel, *Can. Mineral.* **1999**, *37*, 1445.
- [21] H. Kalo, W. Milius, M. Bräu, J. Breu, *J. Solid State Chem.* **2013**, *198*, 57–64.
- [22] R. Shannon, *Acta Crystallogr., Sect. A* **1976**, *32*, 751–767.
- [23] J. W. McCauley, R. E. Newnham, *Am. Mineral.* **1971**, *56*, 1626–1638.
- [24] H. Toraya, *Z. Kristallogr. Cryst. Mater.* **1981**, *157*, 173.
- [25] E. Gnos, T. Armbruster, *Am. Mineral.* **2000**, *85*, 242–250.
- [26] W. Loewenstein, *Am. Mineral.* **1954**, *39*, 92–96.
- [27] S. S. Batsanov, *Inorg. Mater.* **2001**, *37*, 871–885.
- [28] G. Tischendorf, H. J. Förster, B. Gottesmann, M. Rieder, *Mineral. Mag.* **2007**, *71*, 285–320.
- [29] A. A. Guseinov, I. O. Gargatsev, R. U. Gabitova, *Izv. Phys. Solid Earth* **2005**, *41*, 670–679.
- [30] J. P. Crine, A. Friedmann, M. R. Wertheimer, A. Yelon, *Can. J. Phys.* **1977**, *55*, 270–275.
- [31] H. G. Tolland, R. G. J. Strens, *Phys. Earth Planet. Inter.* **1972**, *5*, 380–386.
- [32] J. Breu, W. Seidl, A. J. Stoll, K. G. Lange, T. U. Probst, *Chem. Mater.* **2001**, *13*, 4213–4220.
- [33] O. V. Dolomanov, L. J. Bourhis, R. J. Gildea, J. A. K. Howard, H. Puschmann, *J. Appl. Crystallogr.* **2009**, *42*, 339–341.

Received: July 31, 2017

Published Online: October 28, 2017

6.4.1. Supporting Information

Single-Crystal Structure and Electronic Conductivity of Melt Synthesized Fe-rich, near End-Member Ferro-Kinoshitalite

Matthias Daab,^[a] Patrick Loch,^[a] Wolfgang Milius,^[a] Daniela Schönauer-Kamin,^[b] Michaela Schubert,^[b] Anja Wunder,^[c] Ralf Moos,^[b] Friedrich E. Wagner^[d] and Josef Breu*^[a]

Dedicated to Professor Wolfgang Schnick on the Occasion of His 60th Birthday.

Supporting Information

Content:

- Figure S1: Phase barogram of the iron-molybdenum system
- Figure S2: IR-spectrum
- Figure S3: Octahedral and tetrahedral sheet: Calculation of $(a,b)_t/(a,b)_o$
- Table S1: Mössbauer fit results, Fe-KS, 145 K
- Table S2: Mössbauer fit results, Fe-KS, 4.2 K
- Table S3: Anisotropic displacement parameters
- Figure S4: Nyquist-plots
- Figure S5: Mössbauer spectrum of oxidized Fe-KS
- Table S4: Mössbauer fit results, oxidized Fe-KS, room temperature
- Figure S6: PXRD of Fe-Tain
- Supporting references

* Prof. Dr. Josef Breu
E-mail: Josef.Breu@uni-bayreuth.de

[a] Bayerisches Polymer Institut und Anorganische Chemie 1, Universität Bayreuth, Universitätsstraße 30, 95447 Bayreuth, Germany.

[b] Lehrstuhl für Funktionsmaterialien
Universität Bayreuth
Universitätsstraße 30, 95447 Bayreuth, Germany

[c] Lehrstuhl für Organische Chemie 1
Universität Bayreuth
Universitätsstraße 30, 95447 Bayreuth, Germany

[d] Physik-Department E15
Technische Universität München
James-Franck-Straße, 85748 Garching, Germany

Ergebnisse

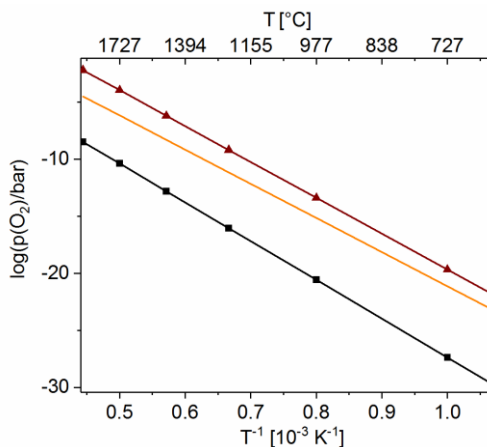


Figure S1: Phase barogram showing the temperature dependent oxygen fugacities of the systems Fe-FeO (black line, squares), FeO-Fe₃O₄ (red line, triangles) and Mo-MoO₂ (orange, straight line). The Mo-crucible acts as an O₂-buffer at elevated temperatures during synthesis and provides an oxygen fugacity in the stability range of FeO.

The oxygen fugacities ($\log\left(\frac{p\text{O}_2}{\text{bar}}\right) = A - \frac{B}{T}$ with $A = \frac{\Delta S_R(T)}{2.303 \cdot R}$ and $B = \frac{\Delta H_R(T)}{2.303 \cdot R} \cdot [K]$) were calculated using thermodynamic data of NIST-JANAF tables.^[1] The thermodynamic data at 1300 K for the reaction $x M^{ox} \rightleftharpoons y M^{red} + 1 O_2$ are the following: for oxygen $H^0-H^0(298.15\text{K}) = 33 \text{ kJ/mol}$ and $S^0 = 253 \text{ J/molK}$ and for the crystalline phases:

	x	y	$\Delta_f H_{\text{ox}}^0$ (*)	S_{ox}^0	$\Delta_f H_{\text{red}}^0$ (*)	S_{red}^0	ΔH_R	ΔS_R	A	B
			/kJ/mol	/J/molK	/kJ/mol	/J/molK	/kJ/mol	/J/molK		
FeO/Fe	2	2	-270	142	39	79	651	127	6.6	34000
Fe ₃ O ₄ /FeO	2	6	-1095	441	-270	142	602	225	11.8	31500
MoO ₂ /Mo	1	1	-573	153	27	68	633	168	8.8	33100

(*) for the elements Fe and Mo $H^0-H^0(298.15\text{K})$ is given instead of $\Delta_f H^0$.

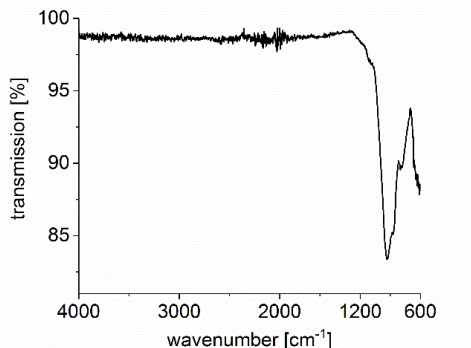


Figure S2: FT-IR-spectrum of Fe-KS. Si-O stretching frequencies are found in the range of 1000 cm^{-1} , while bending frequencies are found at about 500 cm^{-1} .^[2] The substitution with Al results in additional bands in the range of 900 to 500 cm^{-1} for annite-type micas.^[2-3] By this means it is not possible to distinguish the spectral features from all sidephases (see main text, Figure 1) from those of the Ferro-Kinoshitalite. In comparison to natural micas the OH-bands are absent because a Fluoro-mica has been synthesized without octahedral OH^- .

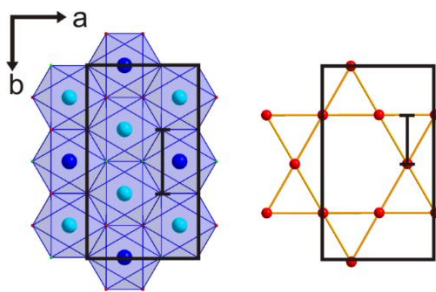


Figure S3: Octahedral sheet (left) and basal plane of the tetrahedral sheet (right) of the mica structure. For undistorted sheets the b -dimension contains 3 times the edge length of an ideal octahedron and 4 times the altitude of an equilateral triangle of basal oxygens. The mean bond length ($\langle \text{M-O/F} \rangle_{\text{shannon}}$ and $\langle \text{T-O} \rangle_{\text{shannon}}$) represents the radius of the circumspheres of the polyhedrons which is used to derive the edge length and the altitude:

$$\text{Edge length (e) of the circumsphere of an octahedron: } e = \frac{r \cdot 2}{\sqrt{2}} = \frac{\langle \text{M-O/F} \rangle_{\text{shannon}} \cdot 2}{\sqrt{2}}$$

$$b\text{-dimension of an ideal octahedral sheet: } b_o = 3 \cdot e = 3\sqrt{2} \cdot \langle \text{M-O/F} \rangle_{\text{shannon}}$$

$$\text{Edge length (e) of the circumsphere of a tetrahedron: } e = \frac{r \cdot 4}{\sqrt{6}} = \frac{\langle \text{T-O} \rangle_{\text{shannon}} \cdot 4}{\sqrt{6}}$$

$$\text{Altitude (h) of an equilateral triangle of basal oxygens: } h = \frac{\sqrt{3}}{2} e = \sqrt{2} \cdot \langle \text{T-O} \rangle_{\text{shannon}}$$

$$b\text{-dimension of an ideal tetrahedral sheet: } b_t = 4 \cdot h = 4\sqrt{2} \cdot \langle \text{T-O} \rangle_{\text{shannon}}$$

$\langle \text{M-O/F} \rangle_{\text{shannon}}$ and $\langle \text{T-O} \rangle_{\text{shannon}}$ were calculated using Shannon^[4] radii (listed in the caption of Table 4) according to the refined compositions. Octahedral vacancies were not considered.^[5]

Ergebnisse

Table S1: Mössbauer spectrum: Fit results for Fe-KS at 145 K. QS are the splittings of the electric quadrupole doublets, and IS the isomer shifts with respect to metallic iron at room temperature.

Component	QS (mm/s)	IS (mm/s)	Rel. Area (%)
Fe(II) a	2.36	1.27	75
Fe(II) b	1.96	1.27	20
Fe(III)	0.85	0.50	5

Table S2: Mössbauer spectrum: Fit results for Fe-KS at 4.2 K. Fe-QS is the electric quadrupole interaction $eqV_{zz}/2$ for the Fe(II) magnetic hyperfine patterns, or the corresponding quadrupole shift in the Fe(III) magnetic hyperfine patterns. IS is the isomer shift with respect to metallic iron at room temperatures. B is the magetic hyperfine field.

Component	QS (mm/s)	IS (mm/s)	B (Tesla)	Rel. Area (%)
Fe(II) a	-1.93	1.27	23.8	14
Fe(II) b	-2.56	1.27	21.7	28
Fe(II) c	-2.43	1.27	16.7	25
Fe(II) d	-2.43	1.27	11.6	26
Fe(III) a	-0.34	0.63	51.1	2
Fe(III) b	-0.29	0.56	46.5	3
Fe(III) c	-0.04	0.47	42.2	2

Table S3: Anisotropic displacement parameters, in \AA^2 .

	U ₁₁	U ₂₂	U ₃₃	U ₁₂	U ₁₃	U ₂₃
Ba	0.0304(4)	0.298(4)	0.0341(4)	0.00000	0.0064(3)	0.00000
Fe _{cis}	0.0184(6)	0.0203(7)	0.0244(7)	0.00000	0.0030(4)	0.00000
Al _{cis}	0.018(4)	0.0203(6)	0.0244(7)	0.00000	0.0030(7)	0.00000
Fe _{trans}	0.0239(8)	0.0176(8)	0.0259(9)	0.00000	0.0084(5)	0.00000
Al _{trans}	0.024(2)	0.0176(8)	0.0259(8)	0.00000	0.0084(9)	0.00000
Si	0.0189(7)	0.0192(8)	0.0208(8)	-0.0004(4)	0.0036(5)	-0.0008(4)
Al	0.0189(7)	0.0192(8)	0.0208(8)	-0.0004(4)	0.0036(5)	-0.0008(4)
O1 _{apical}	0.0256(16)	0.0249(18)	0.0281(17)	-0.0008(10)	0.0049(13)	-0.0020(12)
O2 _{basal}	0.0282(16)	0.042(2)	0.0297(17)	-0.0085(14)	0.0060(13)	0.0013(15)
O3 _{basal}	0.045(3)	0.026(3)	0.030(2)	0.00000	0.003(2)	0.00000
F	0.032(2)	0.033(2)	0.043(2)	0.00000	0.0072(17)	0.00000

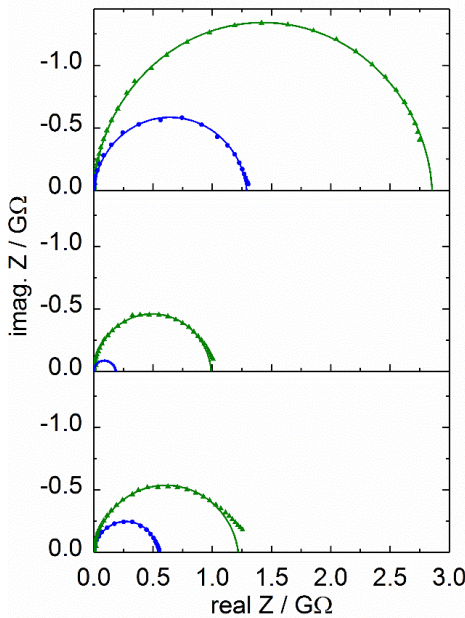


Figure S4: Nyquist-plot for contacted crystals: Fe-KS1 (top), Fe-KS2 (middle) and Fe-Tain (bottom). Measurements under nitrogen (triangles, green) and air (circles, blue) are shown. The extrapolated DC-resistances (fits shown as solid semi circles) are: Fe-KS1 ($2.89\text{ G}\Omega$ nitrogen, $1.29\text{ G}\Omega$ air), Fe-KS2 ($0.992\text{ G}\Omega$ nitrogen, $0.185\text{ G}\Omega$ air) and Fe-Tain ($1.22\text{ G}\Omega$ nitrogen, $0.545\text{ G}\Omega$ air).

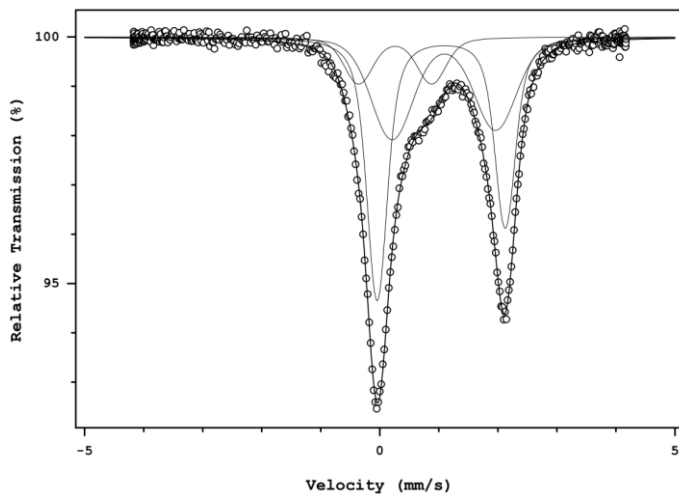


Figure S5: Mössbauer spectrum measured at room temperature of Fe-KS oxidized at 200°C for 24 h in air (same conditions as for the impedance spectroscopy measured under air).

Ergebnisse

Table S4: Mössbauer spectrum: Fit results for Fe-KS oxidized at 200°C for 24 h in air. QS are the splittings of the electric quadrupole doublets, and IS the isomer shifts with respect to metallic iron at room temperature.

Component	QS (mm/s)	IS (mm/s)	Rel. Area (%)
Fe(II) a	2.17	1.16	49
Fe(II) b	1.75	1.20	37
Fe(III)	0.85	0.38	13

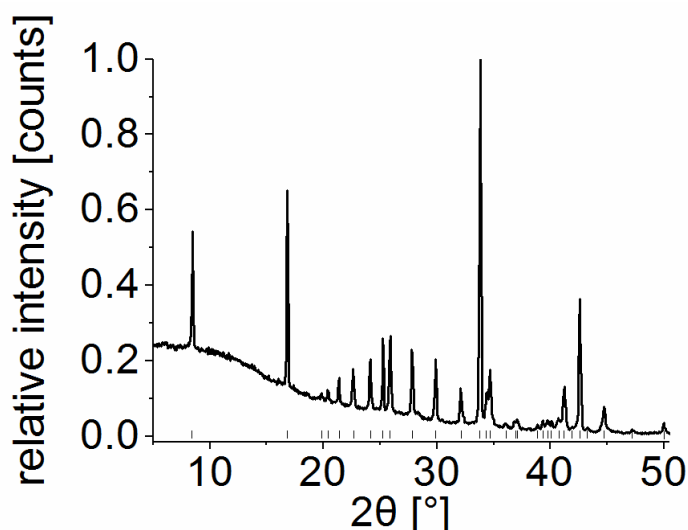


Figure S6: PXRD of Fe-Tain. The same reflections as observed in previous work, marked by ticks, were obtained.^[6]

Supporting References

- [1] M. W. Chase, *J. Phys. Chem. Ref. Data* **1998**, Monograph 9.
- [2] A. Beran, *Rev. Mineral. Geochem.* **2002**, *46*, 351-369.
- [3] G. J. Redhammer, A. Beran, J. Schneider, G. Amthauer, W. Lottermoser, *Am. Mineral.* **2000**, *85*, 449-465.
- [4] R. Shannon, *Acta Cryst. A* **1976**, *32*, 751-767.
- [5] S. Guggenheim, R. A. Eggleton, *Am. Mineral.* **1987**, *72*, 724-738.
- [6] R. Mariychuk, A. Baumgartner, F. E. Wagner, A. Lerf, A. Dubbe, R. Moos, J. Breu, *Chem. Mater.* **2007**, *19*, 5377-5387.

7. Publikationsliste

- “Two-Step Delamination of Highly Charged, Vermiculite-like Layered Silicates via Ordered Heterostructures”
Matthias Daab, Sabine Rosenfeldt, Hussein Kalo, Matthias Stöter, Beate Bojer, Renée Siegel, Stephan Förster, Jürgen Senker, Josef Breu
Langmuir, **2017**, 33, 4816-4822.
- “Single-Crystal Structure and Electronic Conductivity of Melt Synthesized Fe-rich, near End-Member Ferro-Kinoshitalite”
Matthias Daab, Patrick Loch, Wolfgang Milius, Daniela Schönauer-Kamin, Michaela Schubert, Anja Wunder, Ralf Moos, Friedrich E. Wagner, Josef Breu
Z. Allg. Anorg. Chem. **2017**, 643, 1661-1667.
- “Onset of Osmotic Swelling in Highly Charged Clay Minerals”
Matthias Daab, Natalie J. Eichstaedt, Christoph Habel, Sabine Rosenfeldt, Hussein Kalo, Hubert Schießling, Stephan Förster, Josef Breu
Langmuir **2018**, 34, 8215–8222.
- “Layer Charge Robust Delamination of Organo-Clays”
Matthias Daab, Natalie J. Eichstaedt, Andreas Edenhalter, Sabine Rosenfeldt, Josef Breu
RSC Adv. **2018**, 8, 28797-28803.
- “Can high oxygen and water vapor barrier nanocomposite coatings be obtained with a waterborne formulation?”
Evgeny S. Tsurko, Patrick Feicht, Christoph Habel, Theresa Schilling, **Matthias Daab**, Sabine Rosenfeldt, Josef Breu
J. Membrane Sci. **2017**, 540, 212-218.
- “Structural Insights into Water-Based Spider Silk Protein–Nanoclay Composites with Excellent Gas and Water Vapor Barrier Properties”
Elena Doblhofer, Jasmin Schmid, Martin Rieß, **Matthias Daab**, Magdalena Suntinger, Christoph Habel, Hendrik Bargel, Christoph Hugenschmidt, Sabine Rosenfeldt, Josef Breu, Thomas Scheibel
ACS Appl. Mater. Interfaces **2016**, 8, 25535-25543.

Danksagung

8. Danksagung

Mein besonderer Dank gilt meinem geschätzten Hochschullehrer Prof. Dr. Josef Breu. Die ausgezeichnete Betreuung schloss sehr gute und lehrreiche Diskussionen mit ein, seinen Weitblick, die hervorragende und dennoch stetig wachsende Ausstattung am Lehrstuhl und die gewährten Freiheiten „an der langen Leine“.

Dem Fonds der chemischen Industrie danke ich für die großzügige Gewährung eines Promotionsstipendiums.

Dr. Hubert Schießling und Dr. Hussein Kalo von der BYK Chemie GmbH gilt mein besonderer Dank für die Diskussionen in unseren Projektbesprechungen, viele Einblicke und das Vertrauen in unsere Schichtsilikate.

Dr. Sabine Rosenfeldt danke ich für Messungen, Einweisung und Messzeit an der SAXS-Anlage. Beate Bojer, Dr. René Siegel und Prof. Dr. Jürgen Senker danke ich für all die NMR-Messungen. Prof. Dr. Friedrich Wagner danke ich für Mößbauer-Messungen inklusive der Auswertung mit Erklärungen und Literaturstellen dazu. Lena Geiling, Marco Schwarzmann und Sonja Lutschinger gilt mein bester Dank für viele Messungen und Florian Puchtler für die Unterstützung bei Synthesen fernab der vorliegenden Arbeit, was mir für diese den Rücken freihielte. Dr. Wolfgang Milius danke ich herzlich für die intensive Betreuung unserer Diffraktometer, das Aufrechterhalten des Meßbetriebes und seine ständige Hilfsbereitschaft. Petra Seidler, Iris Raithel und Sieglinde Hörath danke ich für ihre organisatorischen Leistungen, die den Arbeitsalltag rund ablaufen ließen.

Meinen Hiwis und ehemaligen Bachelorstudenten Patrick Loch und Natalie Eichstaedt danke ich für ihr präparatives Geschick und ihren unermüdlichen Arbeitseinsatz. Kevin Ament danke ich herzlich für hilfreiche Anmerkungen nach der Lektüre der Rohfassung dieser Arbeit. Den gesamten Lehrstühlen AC1 und AC3 danke ich für die gute Arbeitsatmosphäre und die stete Hilfsbereitschaft untereinander.

Meiner Familie danke ich herzlichst für ihre Unterstützung - nicht nur während dieser Arbeit.

9. Erklärung des Verfassers

(Eidesstattliche) Versicherungen und Erklärungen

(§ 8 Satz 2 Nr. 3 PromO Fakultät)

Hiermit versichere ich eidesstattlich, dass ich die Arbeit selbstständig verfasst und keine anderen als die von mir angegebenen Quellen und Hilfsmittel benutzt habe (vgl. Art. 64 Abs. 1 Satz 6 BayHSchG).

(§ 8 Satz 2 Nr. 3 PromO Fakultät)

Hiermit erkläre ich, dass ich die Dissertation nicht bereits zur Erlangung eines akademischen Grades eingereicht habe und dass ich nicht bereits diese oder eine gleichartige Doktorprüfung endgültig nicht bestanden habe.

(§ 8 Satz 2 Nr. 4 PromO Fakultät)

Hiermit erkläre ich, dass ich Hilfe von gewerblichen Promotionsberatern bzw. –vermittlern oder ähnlichen Dienstleistern weder bisher in Anspruch genommen habe noch künftig in Anspruch nehmen werde.

(§ 8 Satz 2 Nr. 7 PromO Fakultät)

Hiermit erkläre ich mein Einverständnis, dass die elektronische Fassung der Dissertation unter Wahrung meiner Urheberrechte und des Datenschutzes einer gesonderten Überprüfung unterzogen werden kann.

(§ 8 Satz 2 Nr. 8 PromO Fakultät)

Hiermit erkläre ich mein Einverständnis, dass bei Verdacht wissenschaftlichen Fehlverhaltens Ermittlungen durch universitätsinterne Organe der wissenschaftlichen Selbstkontrolle stattfinden können.

Bayreuth, 22.11.2018

.....
Ort, Datum, Unterschrift